A Precision Measurement of the W Boson Mass

A Dissertation Presented

by

Jun Guo

to

The Graduate School

in Partial Fulfillment of the Requirements

for the Degree of

Doctor of Philosophy

in

Physics

Stony Brook University

August 2009

Stony Brook University

The Graduate School

Jun Guo

We, the dissertation committee for the above candidate for the Doctor of Philosophy degree, hereby recommend acceptance of this dissertation.

Robert L. McCarthy – Dissertation Advisor
Professor, Department of Physics and Astronomy

Roderich Engelmann – Chairperson of Defense
Professor, Department of Physics and Astronomy

Thomas T.S. Kuo
Professor, Department of Physics and Astronomy

Heidi Schellman
Professor of Physics
Northwestern University

This dissertation is accepted by the Graduate School.

Lawrence Martin
Dean of the Graduate School

Abstract of the Dissertation

A Precision Measurement of the W Boson Mass

by

Jun Guo

Doctor of Philosophy

in

Physics

Stony Brook University

2009

In this dissertation, a precision measurement of the W boson mass in $W \to e\nu$ decays with 1 fb^{-1} of collider data collected between 2002 and 2006 at DØ is presented. In the standard model, the mass of W boson(M_W) can be used to make constraints on the Higgs boson mass in conjunction with the top quark mass. The electron energy has been measured with a precision of 0.05%. The measured W boson mass is 80.401 ± 0.043 GeV.

Contents

List of Figures

List of Tables

Acknowledgements

During the DØ W boson mass measurement, a lot of people have kindly provided me help in different ways. First I would like to thank my advisor Professor Robert L. McCarthy, for whom I have great respect. He has been very patient since I started working at DØ and taking baby steps to fit in. Professor McCarthy has also given me a lot of freedom to work my way while maintaining timely guidance when necessary.

In the challenging journey of measuring the W boson mass, nothing would have been achieved without the collaborative work from the postdocs and fellow students in the DØ W mass group - Tim Andeen, Mikolaj Cwiok, Feng Guo, Alex Melnitchouk, Jyotsna Osta, Matt Wetstein, Sahal Yacoob and Junjie Zhu. Ever since I joined the DØ W mass group, Junjie has taught me from the very beginning how to write codes and helped me get familiar with analysis. Special thanks go to the W mass group conveners Jan Stark and Pierre Petroff for their wonderful leadership. Dr. Jan Stark has scrutinized the work from everyone in the group including myself. His high standard kept us going as far as we can. It has been a great experience working with professor Sarah Eno, Martin Grunewald, Mike Hildreth, John Hobbs, Michael Rijssenbeek, and Heidi Schellman, from whom we received many insightful comments and suggestions.

I have gotten valuable advice and help from the Stony Brook group - Subhendu Chakrabarti, Huishi Dong, Satish Desai, Paul Grannis, Feng Guo, Yuan Hu, Dean Schamberger, Emanuel Strauss, Dmitri Tsybychev, Adam Yurkewicz, and Junjie Zhu. I had a wonderful experience working in the calorimeter operations group. It was pleasant to work with those wonderful people on the calorimeter maintenance. During the first year after I joined the Stony Brook high energy group, I was working with professor Roderich Engelmann and Michael Rijssenbeek, who helped me overcome the difficulty in the initial phase.

A lot of thanks go to the Editorial Board for this analysis, which consists of Paul Grannis (chair), Ela Barberis, Jerry Blazey, Marcel Demarteau, Hugh Montgomery, Dean Schamberger. I am thankful that they have spent

considerable time out of their busy schedules to review the analysis.

I definitely want to thank my thesis committee members, Roderich Engelmann, Thomas T.S. Kuo, Robert L. McCarthy and Heidi Schellman for squeezing time out of their busy schedules to serve on my committee.

I am also grateful to my professors during my undergraduate study at the University of Science and Technology of China(USTC). Among them, I want to specially thank my bachelor's thesis advisor Zengbing Chen.

"Thanks" can never fully describe my gratitude to my family, especially my parents. It is their unconditional love and support that have enabled me to come all the way to where I am, even though they do not really understand what I am doing and why I am doing it.

It has been fortunate for me to have worked with so many fantastic people and also to get to know them, many of whom I can not mention here. I have felt honored to work with you and benefit from your wisdom. So great thanks to all of you!!

Chapter 1

Introduction

Ever since physics developed into an independent science four centuries ago, physicists have been trying to understand the motion of objects and the interactions(forces) between them. With better understanding achieved over time, people have expanded their sights from macroscopic lengths to microscopic scales, allowing objects to be studied at more fundamental levels. With the brilliant discovery of the law of gravitation by Isaac Newton, following the careful observations of Johannes Kepler, and the three laws of motion by Isaac Newton, people were able to understand quantitatively the motions of daily objects and celestial bodies for the first time. James Maxwell's development of the classical electromagnetic theory unified electricity, magnetism and even light into one framework by a set of so called "Maxwell's equations".

At the beginning of 20th century, the building of theory of relativity and quantum mechanics by Albert Einstein and other physicists brought human knowledge of nature onto a brand new level. The relation between matter and energy was understood and a dual wave-like and particle-like behavior of matter and radiation was revealed. Aside from the gravitational and electromagnetic interactions, two new interactions - strong and weak forces were found in experiments. It has always been physicists' belief and ambition to unify all known interactions into one theory, although theories of general relativity and quantum mechanics have not been unified.

1.1 Overview of Particle Physics

Among the branches of physics, particle physics is devoted to study the elementary constituents of matter and radiation, and the interactions between them on the smallest scale of matter. Since particles with extremely high energies are used in studying the fundamental structure of matter and their interactions, particle physics is also called high energy physics.

Currently, the well established theoretical framework in particle physics is the Standard Model. It describes three of the four known fundamental interactions and the elementary particles which take part in these interactions by a gauge theory of the strong and electroweak interactions with the gauge group SU(3)×SU(2)×SU(1), among which SU(3) accounts for the strong interaction and SU(2)×SU(1) describes the electroweak interaction[1]. It is a simple and comprehensive theory which explains hundreds of particles and complex interactions with only:

- 6 quarks(u, d, s, c, b, t)
- 6 leptons($e, \mu, \tau, \nu_e, \nu_\mu, \nu_\tau$)
- Force carrier particles(gluon, photon, $W^\pm$, Z^0)

Figure 1.1 shows all 17 particles together with their masses in the Standard Model which are the constituents of matter and force carriers. Table 1.1 [2]lists the fundamental forces and mediators, among which the gravitational force is not included in the Standard Model.

Interaction	Mediator	Charge	Spin	Mass (GeV/c^2)
Strong	gluon(g)	0	1	0
Electromagnetic	photon(γ)	0	1	0
Weak	$W^\pm$	± 1	1	80.399 ± 0.025
	Z^0	0	1	91.188 ± 0.002
Gravitational	Graviton(G)	0	2	0

Table 1.1: Fundamental interactions and mediators.

In the Standard Model, all elementary particles are either fermions or bosons. Fermions(bosons) are defined as elementary particles having $J = n\frac{\hbar}{2}$, where n is an odd(even) integer. Fermions obey Fermi-Dirac statistics and the Pauli exclusion principle, while bosons respect Bose-Einstein statistics. There are 12 known fermions, each with a corresponding antiparticle. They are classified according to how they interact (or equivalently, by what charges they carry). There are six quarks (up, down, charm, strange, top, bottom), and six leptons (electron, muon, tauon, and their corresponding neutrinos). Pairs from each classification are grouped together to form a generation, with corresponding particles exhibiting similar physical behavior.

Among the fermions, quarks are the fundamental constituents of matter. The defining property of the quarks is that they carry color charge, and hence, interact via the strong force. Quarks are combined to form composite particles, hadrons, the best-known of which are protons and neutrons, as shown in figure 1.2. So far quarks have never been observed in isolation and have only been found within hadrons, which is explained by a phenomenon known as color confinement. It is the physics phenomenon that color charged particles (such as quarks) cannot be isolated, and therefore cannot be directly observed. Quarks, by default, clump together to form groups, or hadrons. There are two types of hadrons: mesons and the baryons, composed of two and three quarks respectively. The constituent quarks in a group cannot be separated from their parent hadron, and this is why quarks can never be studied or observed in any more direct way than at a hadron level. Quarks also carry electric charge and weak isospin. Hence they interact with other fermions both electromagnetically and via the weak nuclear interaction. They, along with gluons, are the only particles in the Standard Model to experience the strong interaction in addition to the other three fundamental interactions.

The other six fermions do not carry color charge and are called leptons. The three neutrinos do not carry electric charge either, so their motion is directly influenced only by the weak nuclear force, which makes them extremely difficult to detect. However, by virtue of carrying an electric charge, the electron, muon and the tauon interact electromagnetically.

In the Standard Model, the forces are explained as a result of the exchanging force mediating particles between matter particles. When a force mediating particle is exchanged, at a macro level the effect is equivalent to a force influencing both of them, and the mediating particle is therefore said to have mediated that force. Force mediating particles are believed to be the reason why the forces and interactions between matter particles observed in the laboratory and in the universe exist.

The known force mediating particles described by the Standard Model have spin-1, meaning that all force mediating particles are bosons. In consequence, they do not follow the Pauli Exclusion Principle. The different types of force mediating particles are described as follows.

- The eight massless gluons mediate the strong interactions between color charged quarks. The eightfold multiplicity of gluons is labeled by a combination of color and an anticolor charge (e.g., red-antigreen). Since the gluon carries an effective color charge, they can interact among themselves. The gluons and their interactions are described by the theory of quantum chromodynamics.

- Photons mediate the electromagnetic force between electrically charged particles. The photon is massless and is well-described by the theory of quantum electrodynamics.

- The massive $W^{\pm}$ and Z gauge bosons mediate the weak interactions between particles of different flavors (all quarks and leptons). The weak interactions involving the $W^{\pm}$ act on exclusively left-handed particles and right-handed antiparticles. Furthermore, the $W^{\pm}$ carry an electric charge of +1 and -1 and couple to the electromagnetic interactions. The electrically neutral Z boson interacts with both left-handed particles and antiparticles. These three gauge bosons along with the photons are grouped together which collectively mediate the electroweak interactions.

1.2 Electroweak Theory

It is our belief that the nature can be explained by one simply beautiful, self-contained theory. Physicists continuously seek for any possibility of unifying the known forces into one theoretical framework. In the 1960's, Abdus Salam, Sheldon Glashow and Steven Weinberg independently unified the weak and electromagnetic interaction under a gauge group SU(2)×SU(1) [1].

With understandings of nature at more and more fundamental levels, in addition to the knowledge about matter and forces, physicists came to achieve perspectives of some basic rules that nature might follow, among which symmetry is deemed to be a powerful constraint when considering any possibly correct theory that could describe the laws of nature. In the history of modern physics, symmetry has been used extensively by theoretical physicists. Einstein is insightful in discovering the intrinsic symmetry in nature, which led to the development of general theory of relativity.

In the middle of the last century, gauge theory was brought up into prominence. It is a field theory in which the Lagrangian is invariant under a certain continuous group of transformations. Instead of the global gauge invariance, local gauge invariance brought new insights into physics when constructing Lagrangians. Local gauge invariance introduces a new field which requires its own free Lagrangian. In order for the new field not to spoil the local gauge invariance, the new field needs to be massless. Inspired by the same idea that a global invariance should also hold locally, C. N. Yang and Robert Mills developed a non Abelian gauge theory, widely known as Yang-Mills theory. In this theory, Yang and Mills amazingly managed to promote the global gauge invariance of a non Abelian group to the status of a local gauge invariance. The implementation is subtle and it is very remarkable that is works at all. Although Yang-Mills theory in its initial form was of little use until 1960, Yang-Mills theory turned out to be successful in the formulation of both electroweak unification and quantum chromodynamics (QCD) when combined with the concept of the breaking of symmetry in massless theories which was put forward initially by Jeffrey Goldstone, Yoichiro Nambu and Giovanni Jona-Lasinio[4][5][6].

Spontaneous symmetry breaking takes place when a system that is symmetric with respect to some symmetry group has a vacuum state that is not symmetric. When that happens, the system no longer appears to behave in a symmetric manner. One of the consequences of the spontaneous symmetry breaking of a continuous global symmetry is the appearance of one or more massless scalar. The Higgs mechanism utilizes the spontaneous symmetry breaking and the local gauge invariance which impressively introduces a free gauge field that has a “mass”. In the Standard Model, the Higgs mechanism is responsible for the masses of the weak interaction gauge bosons($W^{\pm}$ and Z^0). Spontaneous breaking of gauge symmetries plays a key role in the model of unified weak and electromagnetic interactions independently built by Weinberg and Salam. A scalar massive Higgs field is naturally incorporated into the Lagrangian, which thus becomes local gauge invariant. The discussion below is following the book by Francis Halzen and Alan D. Martin[3]. More details can also be found in [7] and [8]

In the quantum electrodynamics(QED), by demanding invariance of the Lagrangian for a free fermion,

$$L = \overline{\psi}(i\gamma^{\mu}\partial_{\mu} - m)\psi, \tag{1.1}$$

under local gauge transformations

$$\psi \rightarrow \psi' = e^{i\alpha(x)Q}\psi \tag{1.2}$$

where Q is the charge operator(with eigenvalue -1 for an electron).

By requiring local gauge invariance, the Lagrangian of QED is naturally deducted:

$$L = \overline{\psi}(i\gamma^{\mu}\partial_{\mu} - m)\psi - e\overline{\psi}\gamma^{\mu}Q\partial_{\mu}\psi A_{\mu} - \frac{1}{4}F_{\mu\nu}F^{\mu\nu} \tag{1.3}$$

To incorporate the weak interaction, we replace equation (1.1) first by an isotriplet of weak current $\mathbf{J}_{\mu}$ coupled to three vector bosons $\mathbf{W}^{\mu}$,

$$-ig\mathbf{J}_{\mu} \cdot \mathbf{W}^{\mu} = -ig\overline{\chi}_L\gamma^{\mu}\mathbf{T} \cdot \mathbf{W}^{\mu}\chi_L \tag{1.4}$$

and second by a weak hypercharge current coupled to a fourth vector boson

B^μ,

$$-i\frac{g'}{2}{j_\mu}^Y \cdot B^\mu = -ig'\overline{\psi}\gamma^\mu\frac{Y}{2}\psi B^\mu \tag{1.5}$$

Here, $\mathbf{T}$ and Y are the generators of the $SU(2)_L$ and $U(1)_Y$ groups of gauge transformations. g, g' are the couplings of fermions to $\mathbf{W}^\mu$ and B^μ.

The generators of the three groups satisfy

$$Q = T^3 + \frac{Y}{2}, \tag{1.6}$$

so that

$${j_\mu}^{em} = {J_\mu}^3 + \frac{1}{2}{j_\mu}^Y, \tag{1.7}$$

${j_\mu}^{em}$ is the electromagnetic current. ${J_\mu}^3$ and $\frac{1}{2}{j_\mu}^Y$ are two neutral currents belonging to symmetry groups $SU(2)_L$ and $U(1)_Y$ respectively. Therefore, the two physical neutral gauge fields A_μ and Z_μ are orthogonal combinations of the gauge fields ${W_\mu}^3$ and B_μ, with mixing angle θ_W. The interaction in the neutral current sector can be written as

$$-igJ_\mu{}^3W^{3\mu} - -i\frac{g'}{2}{j_\mu}^Y \cdot B^\mu = -ie{j_\mu}^{em}A^\mu - \frac{ie}{\sin\theta_W\cos\theta_W}[{J_\mu}^3 - \sin^2\theta_W j_\mu^{em}]Z^\mu \tag{1.8}$$

Since the electromagnetic interaction must appear on the right-hand side, we obatain

$$e = g\sin\theta_W = g'\cos\theta_W \tag{1.9}$$

To formulate the Higgs mechanism so that the $W^\pm$ and Z^0 become massive and the photon remains massless, we introduce an $SU(2)$ and $U(1)$ gauge invariant Lagrangian for four scalar fields ϕ_i

$$L' = |(i\partial_\mu - g\mathbf{T}\cdot\mathbf{W}_\mu - g'\frac{Y}{2}B_\mu)\phi|^2 - V(\phi) \tag{1.10}$$

To maintain the gauge invariance of L', the ϕ_i must belong to $SU(2)$ and $U(1)$ multiplets. The gauge boson masses are identified by substituting the vacuum expectation value $\phi_0 = \begin{pmatrix} 0 \\ v \end{pmatrix}$(Here, v is the location where $V(\phi)$ reaches its minimum.) for $\phi(x)$ in the Lagrangian L', in which the relevant term is $|(-ig\frac{\tau}{2}\cdot\mathbf{W}_\mu - i\frac{g'}{2}B_\mu)\phi|^2$

$$= (\frac{1}{2}\nu g)^2{W_\mu}^+W^{-\mu} + \frac{1}{8}\nu^2({W_\mu}^3, B_\mu)\begin{pmatrix} g^2 & -gg' \\ -gg' & g'^2 \end{pmatrix}\begin{pmatrix} W^{3\mu} \\ B^\mu \end{pmatrix} \tag{1.11}$$

where $W^{\pm} = \frac{1}{\sqrt{2}}(W^1 \mp iW^2)$. By identifying the first term as the mass term $M_W^2 W^+ W^-$, we have

$$M_W = \frac{1}{2}\nu g \tag{1.12}$$

With the digitalization by the physical fields Z_μ and A_μ, the second term is identified as

$$\frac{1}{2}M_Z^2 Z_\mu^2 + \frac{1}{2}M_A^2 A_\mu^2 \tag{1.13}$$

By normalizing these fields and using

$$\frac{g'}{g} = \tan\theta_W \tag{1.14}$$

which is easied derived from equation (9), we can obtain

$$A_\mu = \cos\theta_W B_\mu + \sin\theta_W W_\mu^3 \tag{1.15}$$

$$Z_\mu = -\sin\theta_W B_\mu + \cos\theta_W W_\mu^3 \tag{1.16}$$

Therefore, we achieve

$$\frac{M_W}{M_Z} = \cos\theta_W \tag{1.17}$$

1.3 Motivation of the W Mass Measurement

The Standard Model predicts the existence of the W and Z bosons, but it does not quantify their masses. However, the W boson mass is related to other fundamental parameters by[9]

$$M_W = \sqrt{\frac{\pi\alpha}{G_F\sqrt{2}}}\frac{1}{\sin\theta_W\sqrt{1-\Delta r}} \tag{1.18}$$

where α is the electromagnetic constant, G_F is the Fermi constant. θ_W is the weak mixing angle defined by equation (1.17).

Δr represents all radiative corrections.

$$M_Z = 91.1876 \pm 0.0021 GeV \tag{1.19}$$

$$G_F = (1.16639 \pm 0.00002) \times 10^{-5} GeV^{-2} \tag{1.20}$$

$$\alpha = 1/(137.0359895 \pm 0.0000061) \tag{1.21}$$

Within the framework of the Standard Model, Δr is dominated by loops involving the top quark and the Higgs boson, as shown in figure 1.3. The contribution from the $t\bar{b}$ loop is substantial due to the large mass difference between the two quarks. It depends on the top quark mass as $\propto M_t^2$. The correction from the Higgs loop is proportional to $\ln M_H$. So by measuring the top quark mass and W boson mass, the Higgs boson mass can be constrained within the Standard Model. Beyond the Standard Model, there are also some other corrections. For example, in the minimal supersymmetric extension of the Standard Model (MSSM), corrections from the squark loops (figure 1.4) can increase the predicted W mass by up to 250 MeV[10][11].

For equal contributions to the Higgs mass, it is required that the accuracies of the measurements of the W boson and top quark masses be related by

$$\Delta M_W \approx 0.006 \cdot \Delta M_t. \tag{1.22}$$

Currently, the top quark has been measured with an uncertainty of about 1.3 GeV[12]. That means the W mass needs to be measured with an uncertainty of 8 MeV to provide an equivalent constraint. However, the world average of the W mass uncertainty is so far 25 MeV. The W boson mass is the limiting factor in constraining the Higgs boson mass. Figure 1.5[13] shows the Higgs mass as a function of the W mass and top quark mass.

1.4 Previous Measurements of M_W

Continuous efforts have been made to measure the W boson mass by different experiments[15][16] as listed in figure 1.6[13] ever since the W and Z bosons[17] were discovered at CERN by UA1 and UA2 in 1983 with a W mass of 81 ± 5 GeV . From 1996 to 2000, the four experiments of LEP at CERN - ALEPH, DELPHI, l3 and OPAL measured the boson mass with e^+e^- collisions at center-of-mass energies above the W pair production threshold, $\sqrt{s} > 2M_W$. The combined result of the W boson mass from LEP is 80.376 ± 0.033 GeV [13]. The measurements were performed using W pair hadronic decays into four quark jets, leptonic decays into four leptons(two charged leptons + two neutrinos) or hadronic + leptonic decays. The advantage of the LEP experiments is mainly their insensitivity to the theoretical description of the proton or anti-proton content. The bottom part in figure 1.6 from NuTeV, LEP1/SLD, and LEP1/SLD/$\mathrm{m_t}$ show the indirect constraints[13][14] which are not included in the world average.

The Collider Detector at Fermilab(CDF) and DØ experiments at the Fermilab Tevatron collider(proton and anti-proton at $\sqrt{s} = 1.8$ TeV) measured the W mass using data collected from 1992 to 1995 with an uncertainty below 100 MeV. Since 2001, the upgraded CDF and DØ experiment have been taking data at the upgraded Tevatron at center-of-mass energy $\sqrt{s} = 1.96$ TeV. In 2007, CDF published their result using 200 pb^{-1} data with the measured W mass value 80.413 ± 0.0048 GeV.

In this thesis, a precision measurement of the W boson mass using DØ data collected from 2002 to 2006 will be presented.

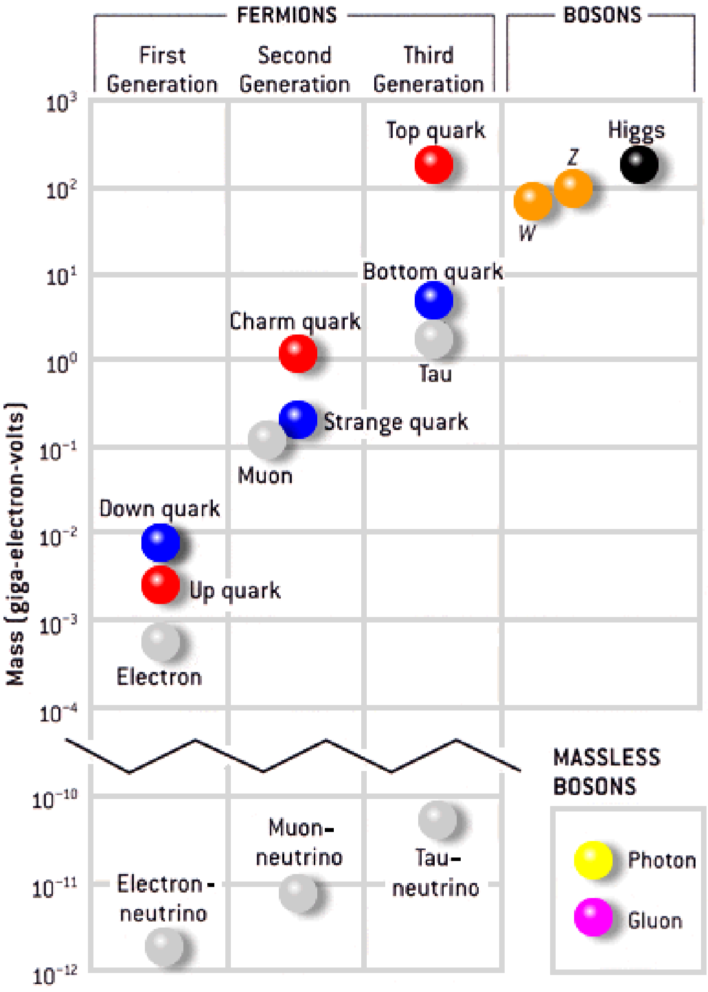

Figure 1.1: The fundamental particles in the Standard Model

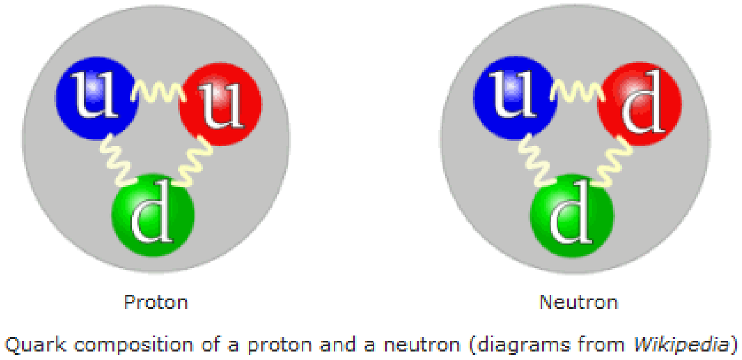

Figure 1.2: Proton and Neutron

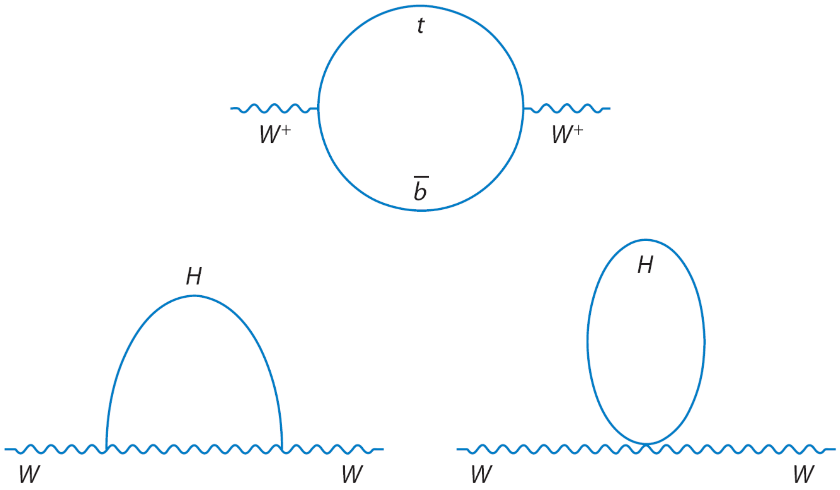

Figure 1.3: One-loop top quark and Higgs corrections to the W boson mass.

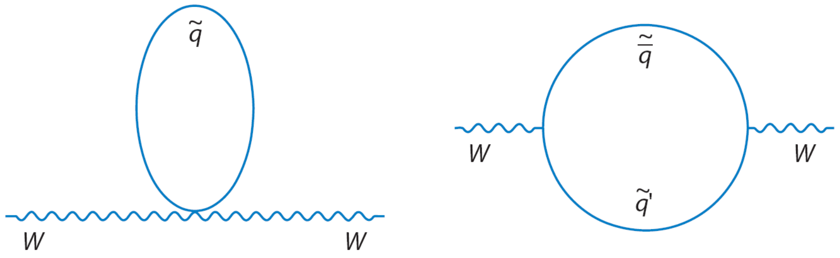

Figure 1.4: One-loop squark corrections to the W boson mass.

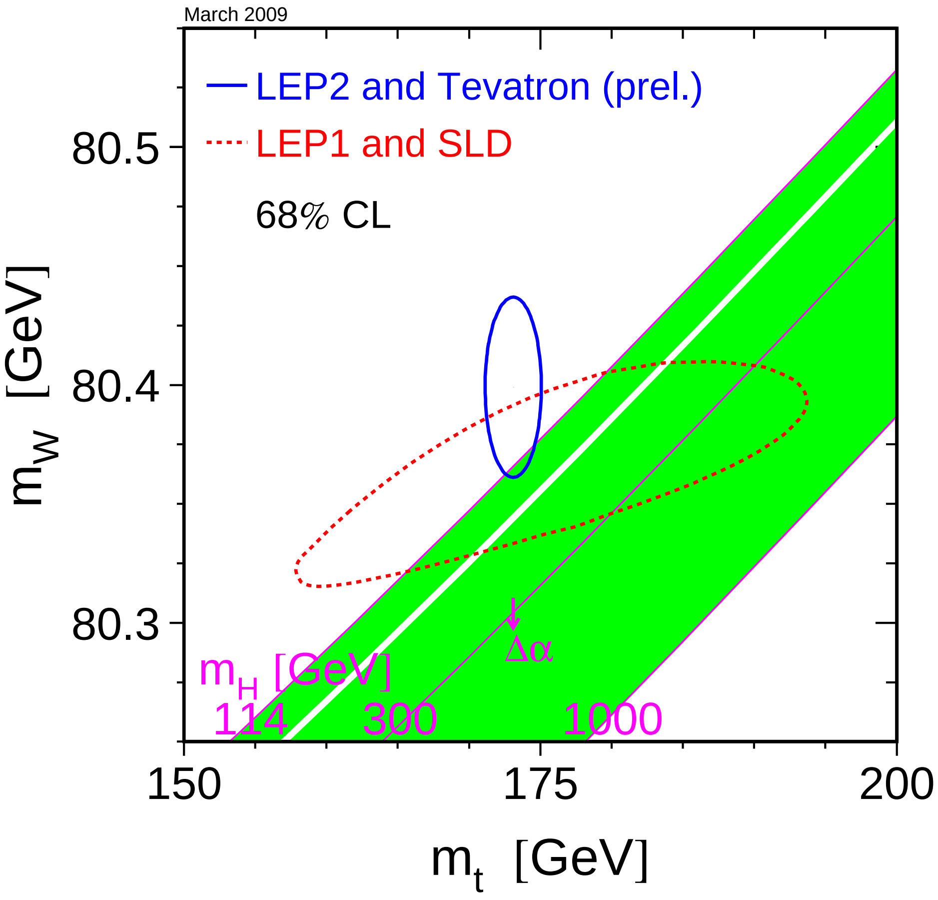

Figure 1.5: Higgs mass constraints as function of M_W and M_{top}. The green band is prediction of the Higgs mass, with 160 GeV to 170 GeV recently ruled out by Tevatron(the white stipe) with 95% C.L. The blue contour corresponds to the 68% C.L.

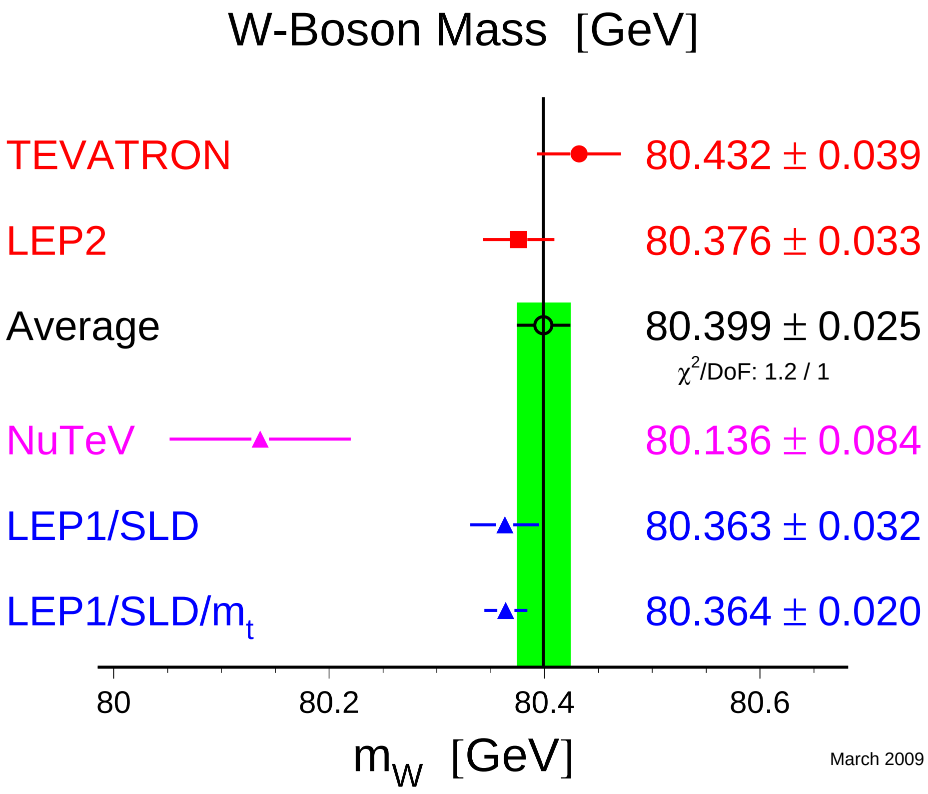

Figure 1.6: Previous measurements of M_W

Chapter 2

Experimental Apparatus

2.1 The Fermilab Accelerator System

The proton-antiproton collision beams are provided by the Tevatron, which is a circular particle accelerator at the Fermi National Accelerator Laboratory(FNAL) in Batavia, Illinois, USA. It is still the highest energy particle collider operating in the world. Protons and antiprotons are accelerated to energies of 0.98 TeV every 396 ns at Tevatron. Details about the accelerator are documented in reference [15][18][19].

The accelerator is composed of a number of different accelerator systems: the Pre-accelerator, Linac, and Booster (collectively known as the Proton Source), Main Injector, Tevatron, Debuncher and Accumulator (These last two machines are referred to as the Antiproton Source). Figure 2.1 is the overview of the accelerator at Fermilab.

2.1.1 Preac, Linac and Booster

The Pre-accelerator(Preacc), is a Cockcroft-Walton accelerator. It provides the source of the negatively charged H^- ions accelerated by the linear accelerator. The H^- gas is accelerated through a column from the charged dome(-750 kV) to the grounded wall to acquire an energy of 750 keV.

The Linear Accelerator(Linac) accelerates the H^- ions with an energy of 750 KeV to an energy of 400 MeV. It has two main sections, the low energy drift tube Linac(DTL) and the high energy side coupled cavity Linac(SCL). DTL focuses the beam by means of quadrupole magnets located inside the drift tubes.The beam traveling through the SCL is focused by quadrupoles placed between the accelerating modules.

The Booster is the first circular accelerator, or synchrotron, in the chain

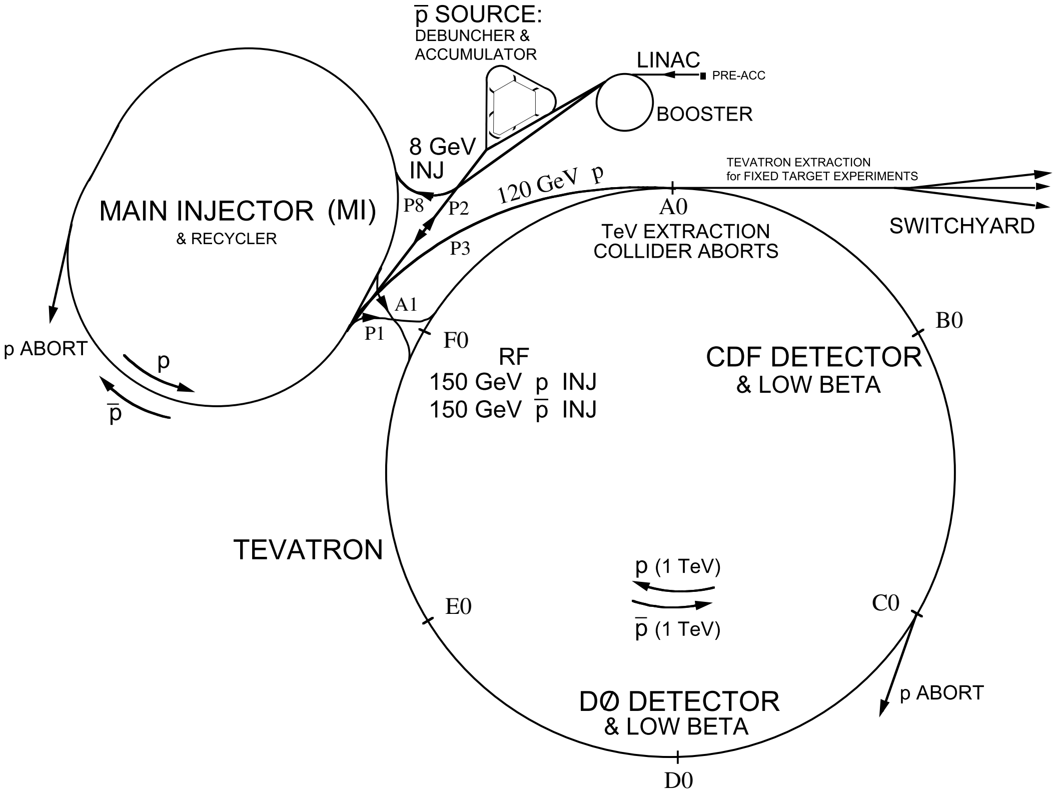

Figure 2.1: Accelerator Overview

of accelerators. It takes the 400 MeV negative hydrogen ions from the Linac and strips the electrons off, which leaves only the proton, and accelerates the protons to 8 GeV. The Booster can accelerate beam once every 66 milliseconds (15 Hz).

2.1.2 Main Injector

The Main Injector (MI) is a circular synchrotron seven times the circumference of the Booster and slightly more than half the circumference of the Tevatron. It consists of 6 sections, labeled MI-10 through MI-60. The MI can accelerate 8 GeV protons from the Booster to either 120 GeV or 150 GeV, depending on their destination. The Main Injector can provide beam to a number of different places at a number of different energies. It can operate in different modes:

- Pbar Production: It produces Pbars, to put in a stack in the accumulator.

- Shot Setup: This mode relates to the act of extracting a bunch of antiprotons from the Antiproton Source and inserting them into the Tevatron.
- The NuMI experiment: The MI sends protons to the NuMI target to produce neutrinos.
- Other modes

2.1.3 Tevatron

The Tevatron is the largest of the Fermilab accelerators, with a circumference of approximately 4 miles. The Tevatron can accept both protons and antiprotons from Main Injector and accelerate them from 150 GeV to 980 GeV. In Collider mode, the Tevatron can store beam for hours at a time. Because the Tevatron is a primarily storage ring, the length of time between acceleration cycles is widely variable. The magnets used in the Tevatron use wire made from superconducting niobium/titanium alloy that needs to be kept extremely cold ($\sim$4 K) by liquid helim to remain a superconductor.

2.1.4 Antiproton Source

The Antiproton Source is composed of the following parts.

- Target: During stacking, 120 GeV protons coming from the MI are directed to strike a nickel target. 8 GeV antiprotons are collected by using magnets out of all sorts of secondary particles produced by the collision. These antiprotons are directed down into the Debuncher.
- Debuncher: It can accept 8 GeV protons from Main Injector for beam studies, and 8 GeV antiprotons from the target station. Its primary purpose is to efficiently capture the high momentum spread antiprotons coming off of the target.
- Accumulator: It is the second synchrotron of the antiproton source and used to store the antiprotons.

2.2 Run IIa DØ Detector

The DØ detector for Run IIa was constructed to study proton-antiproton collisions at a center of mass energy $\sqrt{s} = 1.96$ TeV. It is a multipurpose collider detector, optimized to follow three general goals[20]:

- Excellent identification and measurement of electrons and muons.
- Good measurement of high p_T quark jets through finely segmented calorimetry with good energy resolution.
- A well-controlled measurement of missing transverse energy to characterize the presence of neutrinos and other non-interacting particles.

Figure 2.2 is the overview of the DØ detector. A Cartesian coordinate system is used with the z axis defined by the direction of the proton beam, the x axis pointing radially out of the Tevatron ring, and the y axis pointing up[25][26]. In proton-antiproton collisions the center of mass frame of the colliding partons is approximately at rest in the plane transverse to the beam direction, but the motion along the beam direction of some secondaries can not be determined because of the beam pipe. Therefore the plane transverse to the beam direction is of special importance, and sometimes we work with two-dimensional vectors defined in the x-y plane. We use rapidity $y = +\frac{1}{2}ln(\frac{E+p_z}{E-p_z})$ to define the direction of a particle relative to the beam direction. The rapidity is additive under Lorentz boosts in the beam direction. For a particle with energy much greater than its mass, the pseudorapidity $\eta = -ln\tan(\theta/2)$ is used as a good approximation of rapidity. The DØ detector covers a range of $|\eta| < 4.2$. Its most important components are the central tracking system, uranium/liquid-argon calorimeter and muon system. In the next sections for the subdetectors, we will follow the discussions in reference [26][28].

2.2.1 Central Tracking System

The central tracking system is composed of the silicon microstrip tracker(SMT) and the central fiber tracker (CFT) surrounded by a solenoidal magnet as shown in figure 2.3. They were designed for the excellent tracking measurement in the central region for studies of top quark, electroweak, and b physics and to search for new phenomena, including the Higgs boson.

Silicon Microstrip Tracker(SMT)

The SMT[21] is built to perform the tracking and vertexing over nearly the full coverage of the calorimeter and muon systems. A overview of the SMT is shown in figure 2.4. It has six barrels in the central region, in each of which there are four silicon readout layers. Each barrel is capped at high |z| with an F-disk, which consists of twelve double-sided wedge detectors. The barrel detectors primarily measure the position in the r-ϕ plane and the disk detectors measure the position in both r-z and r-ϕ planes. There are another three F-disks on each side of the forward region. H-disks are sitting in the

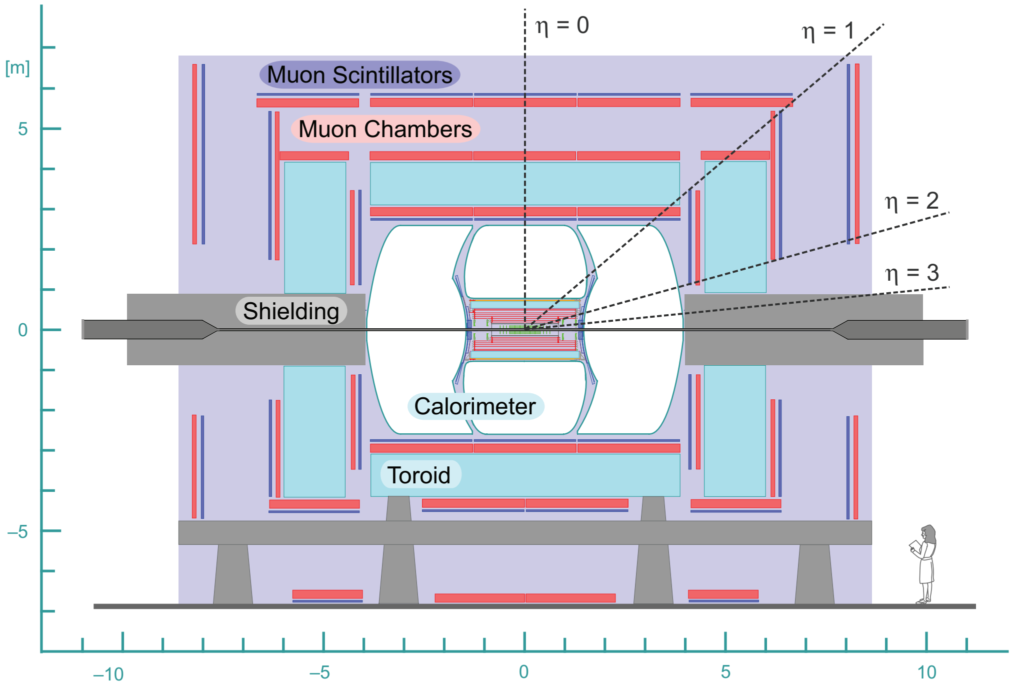

Figure 2.2: DØ Detector

far forward regions to measure tracks at high $|\eta|$. The SMT has 912 readout modules, with 792,576 channels.

Central Fiber Tracker(CFT)

Outside the SMT is the Central fiber tracker(CFT)[22] as shown in figure 2.5. The CFT is made up of scintillating fibers mounted on eight concentric support cylinders, at radii from 20 to 52 cm. It covers a range of $\eta \leq 1.7$. Photons produced by an ionizing particle are detected by a Visible Light Photon Counter (VLPC) that converts the photons into an electrical pulse. The CFT has 76,800 scintillating fibers grouped into doublet layers and can measure the position with a resolution on the order of 100 μm, corresponding to a ϕ resolution of 2×10^{-4} radians.

2.2.2 Solenoid and Preshower

The 2T magnetic field in the central tracking system is provided by the superconducting solenoidal magnet. The magnet was designed to optimize the momentum resolution and tracking pattern recognition within the constraints

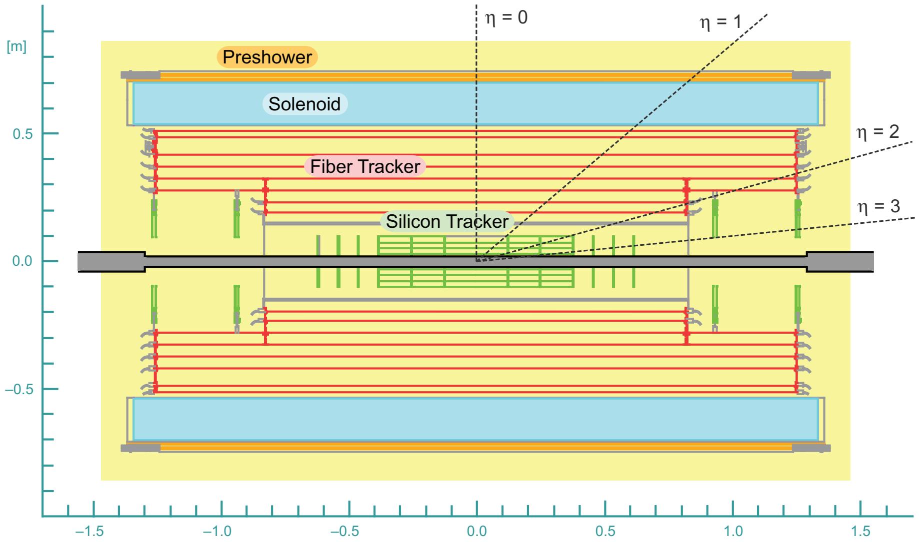

Figure 2.3: DØ Tracking System

imposed by the DØ calorimeter.

The preshower[23][24] detectors are added to help identify electrons and reject background during both triggering and offline reconstruction by enhancing the spatial matching between tracks and calorimeter showers. The central preshower detector covers the region $|\eta| < 1.3$ and the two forward preshower detectors cover $1.5 < |\eta| < 2.5$. The preshower detectors are not used in the W mass measurement due to the electronics saturation from the high luminosity during the RunII data taking.

2.2.3 Calorimeter

To the W mass measurement at DØ the most important subdetector is the uranium/liquid-argon sampling calorimeter(figure 2.6). It is well suited to identify electrons, photons and jets and also measure their energies. A significant improvement to the detectors performance resulted from the removal of the old Main Ring beam pipe from the calorimeters(compared to Run I). Removal of the Main Ring increased the livetime of the detector by approximately 10%, depending on the trigger[26][27].

The calorimeter has one central calorimeter covering $|\eta| < 1.1$. The two forward calorimeter cover $1.5 < |\eta| < 4.2$, as shown in figure 2.7. Each of them is contained in its own cryostat and can be further categorized into an electro-

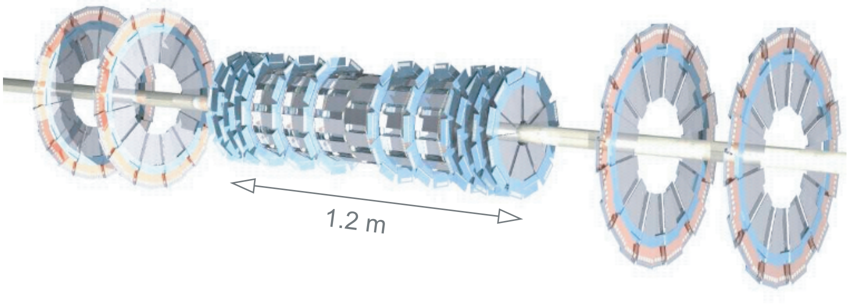

Figure 2.4: DØ Silicon Detector

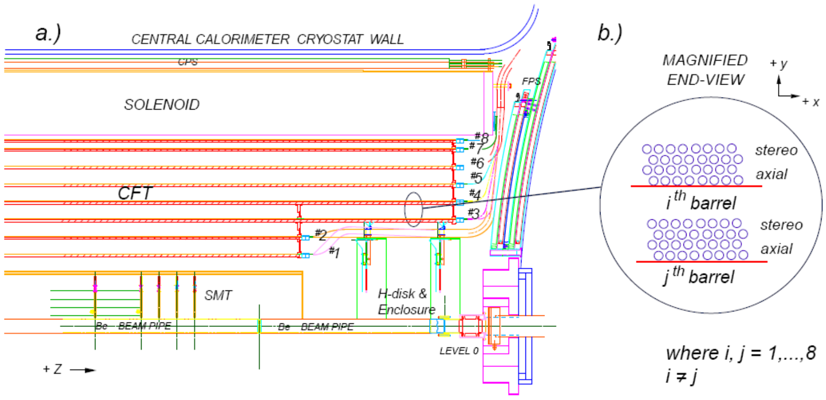

Figure 2.5: DØ Central Fiber Tracker

magnetic section closest to the interaction region and hadronic sections. The hadronic section is composed of fine and coarse calorimeters. Liquid argon is chosen as the active medium because it does not trap charges and allows the ionization produced in electromagnetic or hadronic showers to be collected by the signal boards without amplification. Liquid argon is chosen also because of the relative simplicity of calibration, the flexibility provided in segmenting the calorimeter into transverse and longitudinal cells, the good radiation hardness, and the relatively low cost per channel for readout electronics[20].The three calorimeters (CC, ECN, and ECS) are located within their own cryostats with a temperature maintained at approximately 90 K. In the electromagnetic sections (EM), the absorber plates are made of nearly pure depleted uranium. 6-mm-thick uranium-niobium (2%) alloy is used for the fine hadronic calorimeter and relatively thick (46.5 mm) plates of copper (in the CC) or stainless steel (EC) are used for the coarse hadronic modules .

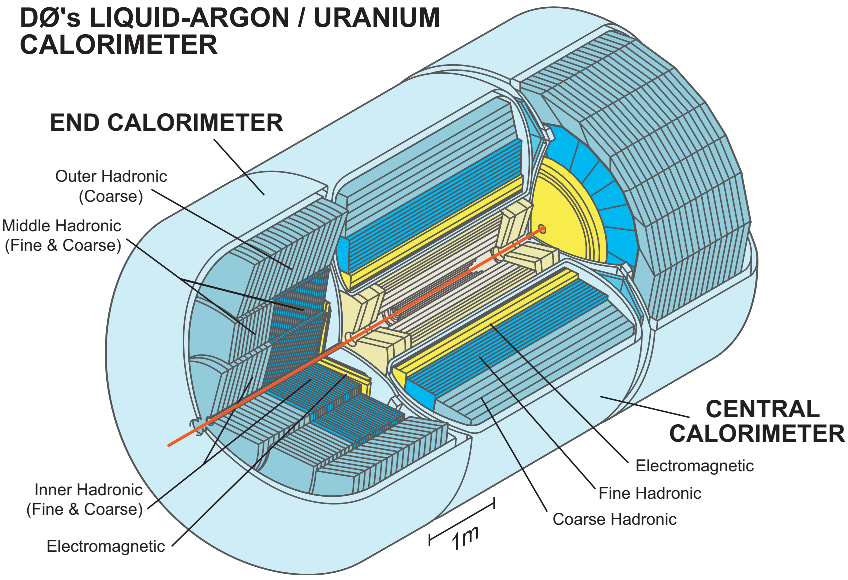

Figure 2.6: DØ Uranium/Liquid-argon Calorimeter

The CC-EM section is composed of 32 azimuthal modules. The entire calorimeter is divided into about 5000 pseudoprojective towers, each covering 0.1×0.1 in $\eta\times\phi$. The EM section is segmented into four layers, 2, 2, 7, and 10 radiation lengths thick respectively. The third layer, in which electromagnetic showers typically reach their maximum, is transversely segmented into cells covering 0.05×0.05 in $\eta\times\phi$ (figure 2.8). The hadronic section is segmented into four layers (CC) or five layers (EC). The entire calorimeter is 7 to 9 nuclear interaction lengths thick. The signals from arrays of 2×2 calorimeter towers, covering 0.2×0.2 in $\eta\times\phi$, are added together electronically for the EM section only and for all sections, and shaped with a fast rise time for use in the level 1 trigger. We refer to these arrays of 2×2 calorimeter towers as trigger towers[25].

Figure 2.9 is the schematic view of a typical calorimeter cell. The metal absorber plates are grounded and the signal boards(G10 boards) with resistive surfaces are placed at a high voltage of 2.0 kV. The electron drift time across the 2.3 mm liquid argon gap is approximately 450 ns. The gap thickness was chosen to be large enough to observe minimum ionizing particle signals and to avoid fabrication difficulties. Particles traversing the gap generate an ionized trail of electrons and ions. The current, produced by the electrons drift in the electric field, induces an image charge on a copper pad etched on the G10

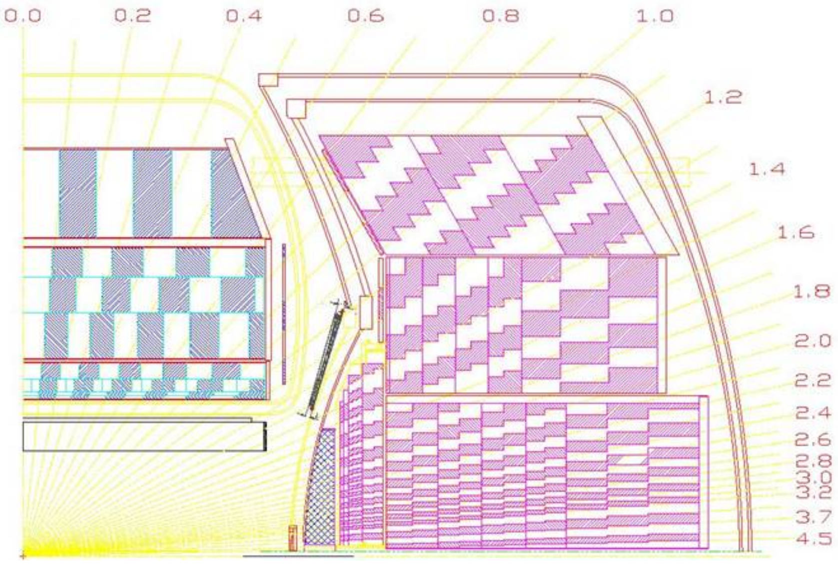

Figure 2.7: DØ Uranium/Liquid-argon Calorimeter showing segmentation in η and depth

board under the resistive coat. The charge is then transferred to calorimeter readout system.

Figure 2.10 shows a schematic of this data path. The signal from each readout cell is brought to a feed-through port on a 30 Ω coaxial cable. The signals are carried from the feed-through ports to the preamplifier inputs on 115 Ω twist & flat cables. The image charge induced on the readout pads by the charge collected on the resistive coat is integrated by the charge-sensitive preamplifiers. The voltage pulses are transferred to the shaper and baseline subtracter (BLS), where the preamplifier outputs are shaped, sampled before and after the bunch crossing, and the difference is stored on a sample & hold circuit. The sample & hold outputs are then read out and digitized by the analog to digital converters(ADCs) when a trigger is received.

It is very important to understand the calorimeter performance. The energy resolution of the calorimeter can be written as equation 2.1.

$$\frac{\sigma_E}{E} = \sqrt{\left(\frac{N}{E}\right)^2 + \left(\frac{S}{\sqrt{E}}\right)^2 + C^2} \tag{2.1}$$

where N, S and C are used in the noise, sampling, and constant terms, respectively. The noise term is from electronic noise summed over readout channels. The sampling term reflects statistical fluctuations such as intrinsic

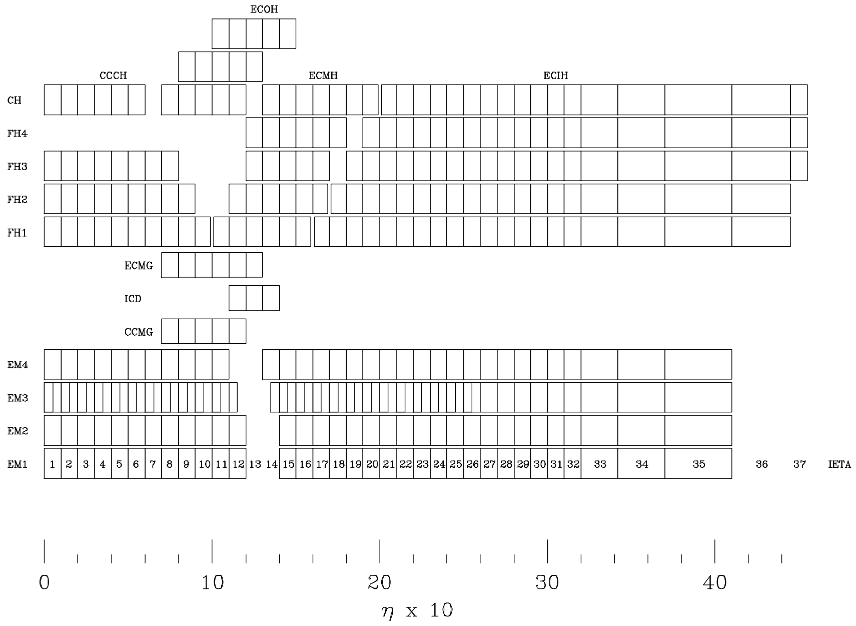

Figure 2.8: Calorimeter channel layout in directions of depth and η

shower fluctuations, including dead material in front of the calorimeter and sampling fluctuations. The constant term accounts for contributions from detector non-uniformity and calibration uncertainty.

2.2.4 Muon System

The upgraded detector uses the original central muon system proportional drift tubes (PDTs) and toroidal magnets, central scintillation counters (some new and some installed during Run I), and a completely new forward muon system. The new forward muon system extends muon detection from $|\eta| \leq 1.0$ to $|\eta| \approx 2.0$, using mini drift tubes (MDTs) instead of PDTs and including trigger scintillation counters and beam pipe shielding. A 1.8 T magnetic field is generated by a toroidal iron magnet in a second tracking system outside the calorimeter to detect muons. Positions are measured by drift chambers. In the DØ W mass measurement, only the tracking system and calorimeter are used.

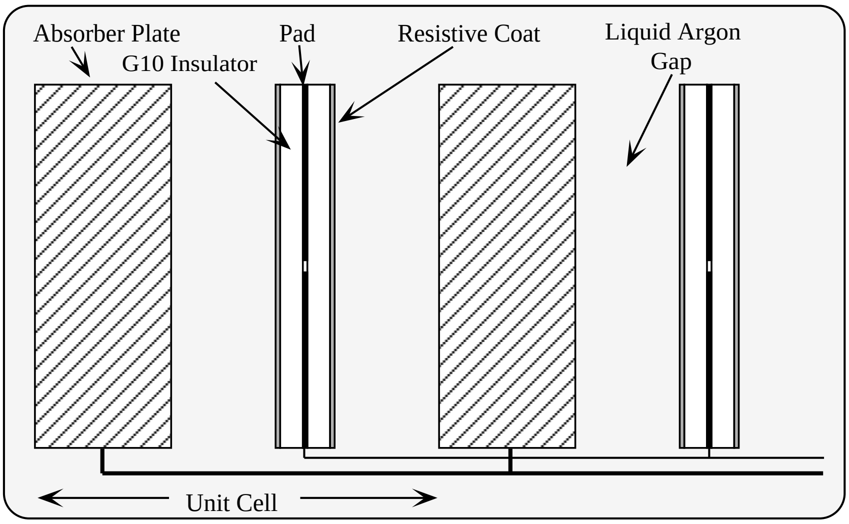

Figure 2.9: Liquid argon gap and signal board unit cell for the calorimeter

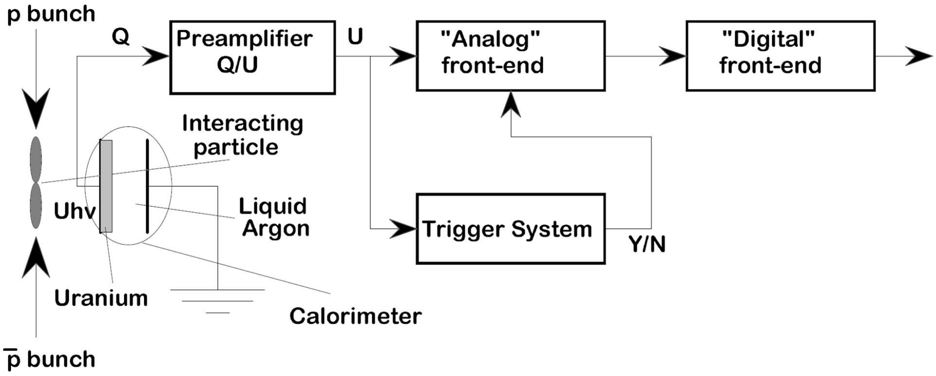

Figure 2.10: Simplified diagram of the calorimeter data flow path.

Chapter 3

Measurement Strategy

In the $Z \to ee$ events, the energy and directions of both electrons are measured precisely by the calorimeter(with fluctuations of order 4% for $p_T(e)$=50 GeV) and the tracking system respectively[31]. However, in the $W \to e\nu$ events, the neutrino escapes detection and leaves behind substantial missing energy. If the W or Z has transverse momentum energy from the recoiling system, the recoil system spreads over a wide range in the detector. It consists of clustered energy as well as unclustered hadronic particles, which cannot be detected. Some of the recoil particles might go along the beam direction and carry substantial longitudinal momentum p_Z. The initial longitudinal momentum sum is unknown, in addition. Therefore, the momentum component along the beam direction of the neutrino cannot be inferred. The invariant W boson mass is unable to be reconstructed. We then resort to the variables in the transverse plane for the W mass information. A variable "Transverse Mass" is defined as

$$m_T = \sqrt{2p_T(e)p_T(\nu)(1 - \cos(\phi(e) - \phi(\nu)))}, \tag{3.1}$$

where $\phi(e)$ and $\phi(\nu)$ are the azimuthal angles of the electron momentum and the $\overrightarrow{\not{E}_T}$ direction, respectively.

The variables m_T and $p_T(e)$ are the two main observables in this measurement. Figure 3.1 shows the different sensitivity of m_T and $p_T(e)$. In the left plot, m_T is relatively insensitive to the transverse momentum of the W boson. However, since m_T is calculated by using the $\not{E}_T$ which is subject to the recoil resolution, m_T is sensitive to the detector effects. In the right hand plot, $p_T(e)$ is sensitive to the $p_T(W)$, which requires a precise calculation of the production dynamics of the W boson. Thanks to the better resolution in measuring the energy of electrons than neutrinos, $p_T(e)$ is barely sensitive to the detector effects. The variables m_T and $p_T(e)$ thus provide us with two complementary distributions. The $p_T(\nu)$ is sensitive to both the detector and boson kinematic effects, which can serve as a cross-check.

3.1 Fast Simulation

Due to the fact that the three distributions are sculpted by the complex detector acceptance and resolution effects, their shapes cannot be calculated analytically. We build a fast parameterized Monte Carlo(fast MC) to simulate the detector and offline selection effects, which smears the events generated by certain event generators. A group of mass templates(distributions predicted by the fast MC) of the prediction of the m_T, $p_T(e)$ and $\not\!\!E_T$ are generated by varying the input W mass. We compare the templates with the corresponding distribution obtained from collider data to extract the W mass value with which the best agreement is achieved. High statistics($\sim 10^8$ events) is required to characterize the different systematic uncertainties with sufficient precision. It is unpractical to simulate the same number of events by using the detailed simulation based on GEANT(full MC), which uses physics principles to model the interaction between particles and detector material. It is also not feasible to tune the full MC to simulate the real detector to the precision needed for the W mass measurement. Due to the above reasons, the fast MC is a good choice, with which we can quickly simulate the necessary events and easily make modifications to find the best match with the data during the model tuning. In tuning the parameters used in the fast MC, $Z \to ee$ samples are extensively used to calibrate the detector response to the energy of electrons and the recoil system, find the selection efficiency, etc. The electron energy response is calibrated by forcing the simulated invariant mass of the two Z electrons to be consistent with the world average Z mass. Since the m_T and Z mass are equally sensitive to the electron energy response, we are essentially measuring the ratio of W and Z masses.

3.2 Fitting Method

In extracting the W mass by fitting the mass templates with the distributions from collider data, a binned negative log likelihood technique is used. The likelihood is calculated as the product of the Poisson probability for each bin, with n_i observed events and m_i expected events:

$$\mathcal{L} = \prod_{i=1}^{N} \frac{e^{-m_i} m_i^{n_i}}{n_i!}. \tag{3.2}$$

By taking the logarithm on both sides, we get

$$\ln \mathcal{L} = \sum_{i=1}^{N} \left(n_i \ln m_i - m_i \right) , \tag{3.3}$$

where the $\ln(n_i!)$ term is a constant so we can ignore it in performing the variations.

Using Minuit [30] we find the mass that minimizes $-\ln \mathcal{L}$ and the $\pm 1\sigma$ values that increase $-\ln \mathcal{L}$ by 0.5. The fits are performed separately for each of the m_T, $p_T(e)$ and $\not{E}_T$ distributions.

3.3 Blinding Technique

The W boson mass has been estimated to be a world average of 80.398 ± 0.025 GeV by combining results from many experiments. To avoid the influence on the analyzers from the world average W mass value, it is important to not let the analyzers know the true measured W mass value during the analysis. In light of that, we performed a "blind analysis" in the Run II W mass measurement[32]. The central value of the measured W mass was hidden from the analyzers and the rest of the collaboration until the agreement between the data and the fast MC reached sufficient quality and the analysis has received preliminary approval from the Editorial Board and the collaboration. An unknown offset in the range [-2 GeV, 2 GeV] was added to the measured W mass. To compare the measured W mass from the three variables(m_T, $p_T(e)$ and $\not{E}_T$), the same offset is applied to them.

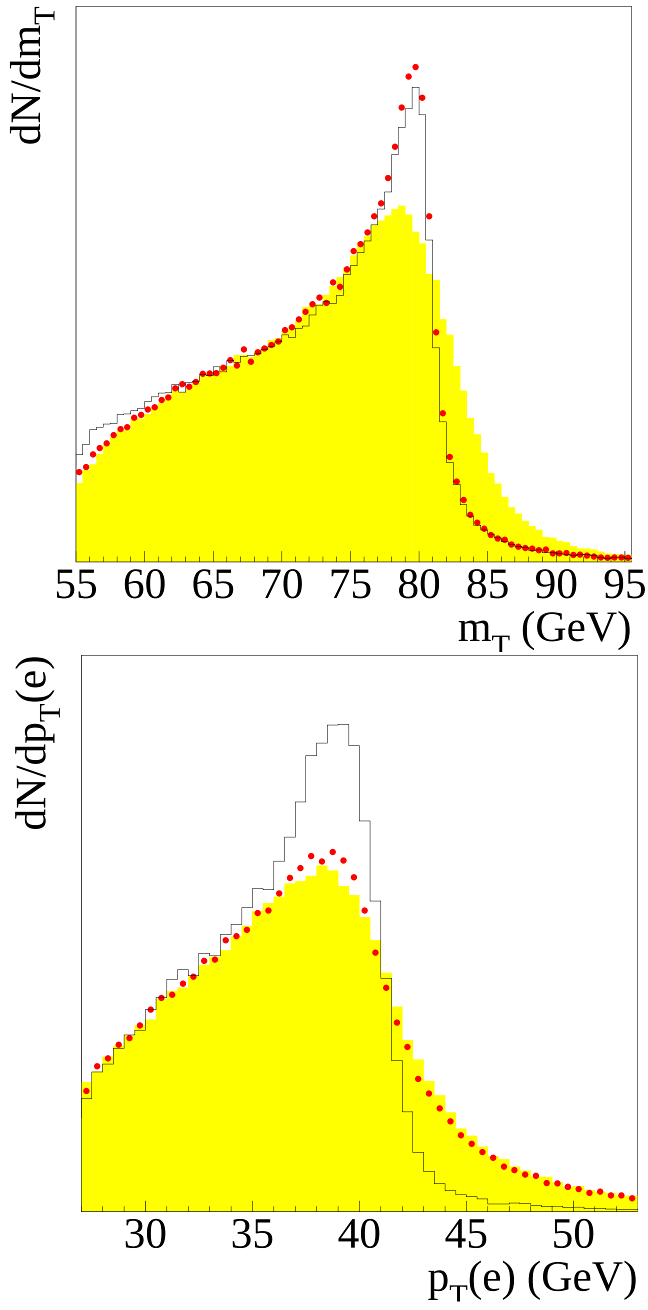

Figure 3.1: Top: m_T distribution; Bottom: $p_T(e)$ distribution(Black: generator level with zero $p_T(W)$; Red: generator level with non-zero $p_T(W)$; Yellow: Detector effect added)

Chapter 4

Data Samples

Three sets of data samples are used with an integrated luminosity of 1.046 fb^{-1} collected from 2002 to 2006 in Run II(figure 4.1): 2EM sample for selecting $Z \to ee$ events, EM+$\not\!\!E_T$ sample for selecting $W \to e\nu$ events and EM+Jet sample for selecting 2Jet events for QCD background study. The average instantaneous luminosity during this period was 41 $\times 10^{30}$ $\mathrm{cm}^{-1}\mathrm{s}^{-1}$ with an average of 1.2 interactions per bunch crossing.

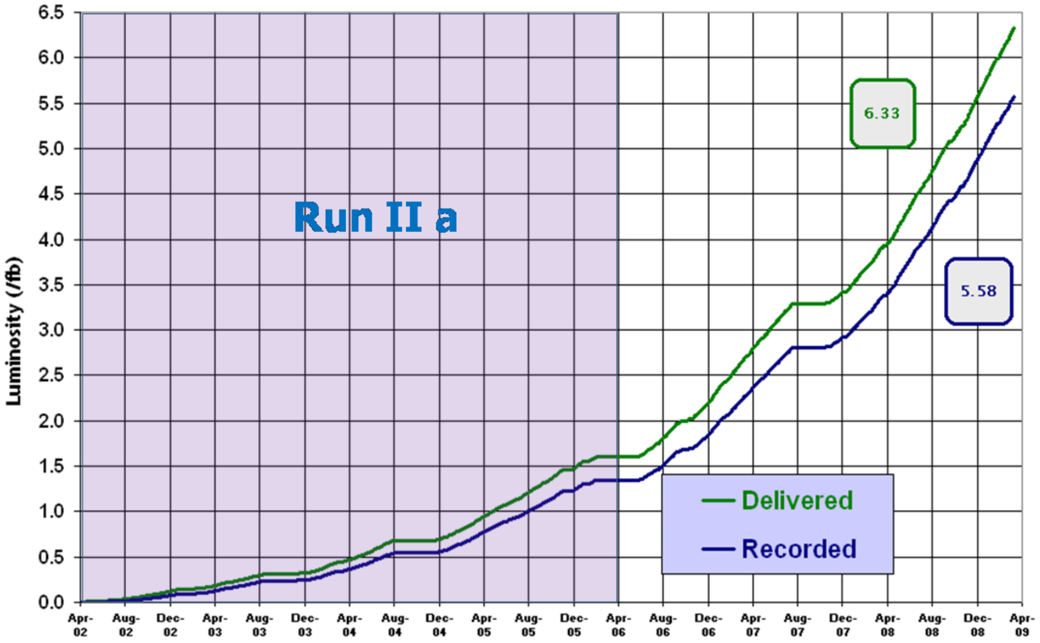

Figure 4.1: DØ RunII instantaneous luminosity vs time

The following requirements were used to select these three samples.

- EM+$\not\!\!E_T$:
  1 EM with $p_T > 20$ GeV, $|\ \eta_{det}\ | < 1.2$, $f_{EM} > 0.9$ and raw $\not\!\!E_T > 20$ GeV

- 2 EM:
  2EM with $p_T > 20$ GeV, $f_{EM} > 0.9$ and $f_{iso} < 0.2$[1]

- EM+Jet:
  1 EM with $p_T > 20$ GeV, $|\ \eta_{det}\ | < 1.2$, $f_{EM} > 0.9$, $f_{iso} < 0.2$,
  1 Jet with $p_T > 20$ GeV, $|\ \eta_{det}\ | < 0.8$ or $1.5 < |\ \eta_{det}\ | < 2.5$,
  0.05<emfrac<0.95, chfrac<0.4, hotcellratio< 10 and n90>10

Here, emfrac is the fraction energy deposited in the electromagnetic section of the calorimeter, chfrac is the fraction of the jet energy deposited in the coarse hadronic section of the calorimeter, hotcellratio is the ratio of the highest to the next-to-highest transverse energy cell in the calorimeter, n90 is the number of towers containing 90% of the jet energy[33].

The sam dataset definitions for the selected samples are:

- EM+$\not\!\!E_T$:
  WMASSskim3-EMMET-WMRESK_p17.09.03-ROOT-wm1,
  WMASSskim3-EMMET-WMRESK_p17.09.06-ROOT-wm1,
  WMASSskim3-EMMET-WMRESK_p17.09.06b-ROOT-wm1

- 2EM:
  WMASSskim3-2EM-WMRESK_p17.09.03-ROOT-wm1,
  WMASSskim3-2EM-WMRESK_p17.09.06-ROOT-wm1,
  WMASSskim3-2EM-WMRESK_p17.09.06b-ROOT-wm1

- EM+Jet:
  tmb_WMASSskim3-EMJET-WMRESK_p17.09.03,
  tmb_WMASSskim3-EMJET-WMRESK_p17.09.06,
  tmb_WMASSskim3-EMJET-WMRESK_p17.09.06b.

4.1 Triggers

During the period of this data collecting, 4 trigger lists were used in the order of time: v8-11, v12, v13 and v14. Each trigger list is a combination of three trigger levels: L1/L2/L3. The first level(L1) is composed of hardware trigger elements which generate an acceptance rate of 2 kHz. On the second

---

[1] f_{EM} and f_{iso} are defined in section 4.2.2.

level(L2), a trigger decision is made based on individual objects as well as object correlations with an acceptance rate of about 1 kHz. The third level(L3) uses sophisticated algorithms on the candidate events sent by L1 and L2 and reduces the rate to approximately 50 Hz.

In our analysis, a single electron trigger with a high efficiency is chosen for each trigger period, as follows: EM_HI_SH, E1_SHT_20, E1_SHT_22 and E1_SHT_25 for v8-11, v12, v13 and v14, respectively. The L1/L2/L3 requirements are listed in Table 4.1.

Trigger	L1	L2	L3
EM_HI_SH	CEM(1,10)	EM(1,12) for runs>169523	ELE_LOOSE_SH_T(1,20)
E1_SHT20	CEM(1,11)	none	ELE_NLV_SHT(1,20)
E1_SHT22	CEM(1,11)	EM(1,15)	ELE_NLV_SHT(1,22)
E1_SHT25	CEM(1,12)	EM(1,15)	ELE_NLV_SHT(1,25)

L1 triggers

CEM(1,10)	one EM trigger tower $E_T > 10$ GeV
CEM(1,11)	one EM trigger tower $E_T > 11$ GeV
CEM(1,12)	one EM trigger tower $E_T > 12$ GeV

L2 triggers

EM(1,12)	one EM candidate with $E_T > 12$ GeV (not present for runs below 169523)
EM(1,15)	one EM candidate with $E_T > 15$ GeV

L3 triggers

ELE_LOOSE_SH_T(1,20)	one electron with $\|\eta\| < 3.0$ and $E_T > 20$ GeV passing loose requirements including shower shape
ELE_NLV_SHT(1,20)	one electron with $\|\eta\| < 3.6$ and $E_T > 20$ GeV passing tight shower shape
ELE_NLV_SHT(1,22)	one electron with $\|\eta\| < 3.6$ and $E_T > 22$ GeV passing tight shower shape
ELE_NLV_SHT(1,25)	one electron with $\|\eta\| < 3.6$ and $E_T > 25$ GeV passing tight shower shape

Table 4.1: Single EM triggers used in this analysis.

4.2 Reconstruction

For each event that has fired the trigger and is therefore written to tape, further detailed offline reconstruction is performed.

4.2.1 Track and Vertex

Charged particles leave curved trajectories under the action of the magnetic field in the central tracking system. The transverse momentum(p_T) of the track is measured from the curvature of the track. The track path is reconstructed by using the hits from the SMT and CFT. Since Run I, the road-following algorithm has been used in finding tracks[34]. In Run II, a Kalman filter[35] is implemented in addition. Global track candidates are constructed after the track segments that are produced for each layer are matched between layers. A χ^2 calculated for the fit between a track and the nearby hits is used to determine whether to accept the track or not.

The primary vertex tells us the parton collision location of incoming particles, which is associated with a lot of tracks. Precise reconstruction of the primary vertex is crucial in calculating the transverse momentum of the recoil system. Long-lived particles such as B, K_S or D bring secondary vertices. The primary vertex candidate is selected by requiring global tracks with at least SMT hit. Then a vertex position is extracted by fitting these tracks until the fit result converges. More details about the primary and secondary vertex reconstruction can be found in [36].

4.2.2 Electron

An electron is identified as a cluster of adjacent calorimeter cells. Its energy is calculated as the sum of the energies in all the EM and FH1 cells in a cone of size $R = \sqrt{(\Delta\eta)^2 + (\Delta\phi)^2} = 0.2$, centered on the tower with the highest fraction of the electron energy. If the electron is associated with a track detected in the central tracking system, the track direction will be taken as the electron direction.

$$\begin{aligned} \theta(e) = & \quad \theta_{track} \\ \phi(e) = & \quad \phi_{track} \end{aligned}$$

Otherwise, the electron direction is calculated using the calorimeter shower centroid position and the primary vertex position. For the final Z and W samples, the track match is always required to select electrons, so the electron direction is using the track direction. When estimating the track match efficiency, we do use electrons without the track match where the electron cluster direction is used.

Electromagnetic clusters found by the reconstruction(EMReco) are required to satisfy $E_T > 1.5$ GeV, $f_{EM} > 0.9$ and $f_{iso} < 0.15$. E_T is the transverse energy of the EM cluster deposited in the calorimeter. f_{EM} is the EM cluster energy fraction in the EM part of the calorimeter

$$f_{EM} = \frac{E_{EM}}{E_{EM} + E_{Had}}, \tag{4.1}$$

where E_{EM} and E_{Had} are the energy measured in the EM and Hadronic part of the calorimeter in a cone of radius $R = \sqrt{\Delta\eta^2 + \Delta\phi^2} = 0.2$, respectively. f_{iso} is the isolation with the definition

$$f_{iso} = \frac{E_{Tot}(R < 0.4) - E_{EM}(R < 0.2)}{E_{EM}(R < 0.2)}, \tag{4.2}$$

where $E_{Tot}(R < 0.4)$ is the total energy in a cone of radius $R = 0.4$ around the direction of the cluster, summed over the entire depth of the calorimeter and $E_{EM}(R < 0.2)$ is the energy in a cone of $R = 0.2$, summed over the EM layers only. Figure 4.2 gives a straightforward view of the isolation definition.

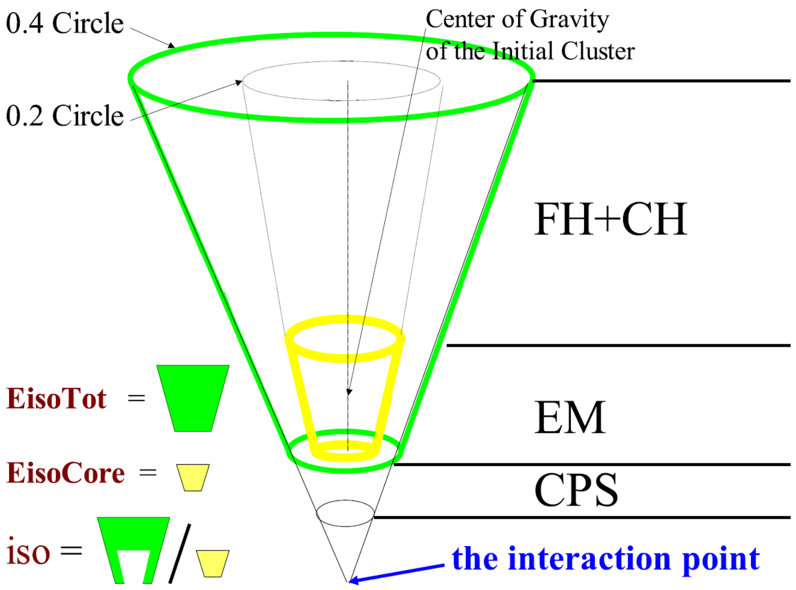

Figure 4.2: Isolation definition

The variables f_{EM} and f_{iso} provide powerful rejection to the hadronic jets that tend to deposit most of their energies in the hadronic calorimeter and are composed of nonisolated particles.

The shower shape of an electron is defined using a covariance matrix technique for electron candidates central calorimeter(CC). To achieve the best discrimination against hadronic jets, both longitudinal and transverse shower shape variables are used, along with the correlations between energy deposits in the calorimeter cells. The inverse of this covariance matrix is called the H-matrix. The H-matrix(7)(HMx7) for central calorimeter is built up with a set of seven variables[37]:

- EM fraction in EM calorimeter layers EM1
- EM fraction in EM calorimeter layers EM2
- EM fraction in EM calorimeter layers EM3
- EM fraction in EM calorimeter layers EM4
- transverse shower width in the ϕ direction
- log_{10}(Energy)
- vertex z position

HMx7 is optimized by using full MC to determine a χ^2 value. Typically we require HMx7 < 12 to select electrons. For electrons in the End Calorimeter(EC), HMx8 is used in stead, which is built up with the above seven variables and the following variable:

- transverse shower width in the z direction

To further reject the hadronic jets background, a spatial track match variable is defined using both the track and calorimeter information.

$$\chi^2 = (\frac{\Delta z}{\sigma_z})^2 + (\frac{\Delta \phi}{\sigma_\phi})^2, \tag{4.3}$$

where Δz and $\Delta\phi$ are the differences between the track position and the EM cluster position in the calorimeter. The σ_z and σ_ϕ are the tracking resolution in z and ϕ, respectively. For a good match, the spatial track matching χ^2 probability $P(\chi^2) > 0.01$.

In the DØ W mass measurement, we also require each track to have at least one hit in the SMT and the track p_T measured by the tracking system is greater than 10 GeV.

4.2.3 $\not{E}_T$

Since the neutrino escapes the detector without being detected, the rest of the event is the hadronic recoil system, which mainly comes from the initial gluon radiation and hadronization, along with the spectator partons interactions, additional proton-antiproton interactions, electronic noise, etc. Since transverse momenta of all the particles except the neutrino in each event are measured by the detector, we infer the neutrino transverse momentum by balancing the transverse momentum from other particles in the event:

$$\not{\boldsymbol{E}}_{\boldsymbol{T}}^{raw} = -\sum_i E_i \sin\theta_i \begin{pmatrix} \cos\phi_i \\ \sin\phi_i \end{pmatrix} = -\sum_i \boldsymbol{E}_T^i, \tag{4.4}$$

where the sum goes over all the calorimeter(central and forward) read out cells except cells in the coarse hadronic calorimeter. E_i are the cell energies, and ϕ_i and θ_i are the azimuth and colatitude of center of cell i with respect to the primary vertex. After we have the raw missing transverse energy, we then apply electron energy corrections on the selected EM cluster(s) from $W(Z)$ decay to get the corrected missing transverse energy $\not{E}_T$. The Intercryostat Detector(ICD) ($1.1 < |\eta_{det}| < 1.4$) is not included due to an unsatisfactory calibration. As previously mentioned, the primary vertex is crucial in calculating the $\not{E}_T$. In recognition of that, we compare the z-component of the electron(s) vertex with that of the event primary vertex. If they are consistent within 2 cm, we will still use the event primary vertex, otherwise we will take the electron(s) vertex as the primary vertex to calculate the $\not{E}_T$.

The scalar E_T (SET) is defined as

$$\mathrm{SET} = \sum_i E_i \mathrm{sin}\theta_i \tag{4.5}$$

in which cells in electron clusters are excluded from the sum. The sum goes through the whole calorimeter(both CC and EC) excluding the ICD and the coarse hadronic calorimeter.

In this analysis the raw energy is used for the recoil since we mostly study events with low boson transverse momentum. In this situation the hadronic recoil system is mainly composed of unclustered particles which spread widely in the detector and therefore no jet energy scale is applied.

4.2.4 Recoil

The recoil $\boldsymbol{u}_T$ for W/Z boson events can be defined from the $\not\!\!\boldsymbol{E}_{\boldsymbol{T}}$ and the electron(s) transverse momentum:

$$\boldsymbol{u_T} = -\not\!\!\boldsymbol{E}_{\boldsymbol{T}} - \sum_e \boldsymbol{p}_T^e = \sum_i \boldsymbol{E}_T^i - \sum_e \boldsymbol{p}_T^e \tag{4.6}$$

4.3 Offline Selection

The next step after the reconstruction is the offline selection.

- $|\mathrm{Z}| < 60$ cm

Electron selection:

- EM ID=10, ±11, $f_{EM} > 0.9$, $f_{iso} < 0.15$
  (EM=10 for an EM cluster without an associated track and ±11 with an associated track)
- $p_T > 25$ GeV
- HMx7< 12 in CC and HMx8< 20 in EC
- In calorimeter fiducial region (in_eta_fiducial and in_phi_fiducial)
- Spatial track match
- Associated track must have at least one SMT hit and $p_T > 10$ GeV

$Z \to ee$ requirements:

- At least one electron passes trigger requirements (L1/L2/L3)
- Both electrons have good matched track
- Electron $|\eta_{det}| < 1.05$
- $\boldsymbol{u_T} < 15$ GeV
- $70 < M_{ee} < 110$ GeV

$W \to e\nu$ requirements:

- The electron must pass trigger requirements (L1/L2/L3)
- The electron must have a good matched track

- Electron $|\eta_{det}| < 1.05$
- $\boldsymbol{u_T} < 15$ GeV
- $50 < M_T < 200$ GeV

After the offline selection we have 499,830 $W \rightarrow e\nu$ candidate events and 18,725 $Z \rightarrow ee$ candidate events.

4.4 Energy Loss Correction

The electron energy is measured by the DØ uranium/liquid-argon sampling calorimeter, where the electron largely develops its electromagnetic shower. However, before reaching the calorimeter, the electron has to travel through dead material(figure 4.3) such as the inner detector, solenoidal magnet, inter-cryostat detector, etc. This uninstrumented material(for calorimetry) is called the "dead" material and is in cylindrical shape around the beam line with a thickness of about 3.7 radiation lengths(X_0). The electron loses some of its energy in this material. The lost energy is estimated by using the standard DØ full MC single electron events. In the full MC, the interaction between the electron and the material in the detector is simulated. The concern is: is the amount of material in front of the calorimeter simulated correctly in the full MC or not? A detailed study did tell us the amount of the dead material is underestimated in the full MC compared to the data.

To best estimate how much material is missing in the full MC, we need a good way to test the performance of simulations, and in particular aspects related to the material model, for example, by checking the well-known invariant mass and the width of the Z boson. Another class of observables [38] are suggested to exploit the longitudinal segmentation of the calorimeter readout. In our case this means looking at the "EM fractions", *i.e.* at the fraction of the measured electron energy deposited in each one of the longitudinal layers (EM1, EM2, EM3 and EM4; and in principle also FH1 but the deposits in FH1 are typically negligibly small) for electrons from a well-characterized source. Figure 4.4 shows the average electron shower profile with two different angles of incidence. If we increase the amount of the dead material, the calorimeter will be "shifted" deeper into the shower. The second and third EM layers are sitting right on the edge of the shower peak, so the electron energy fraction deposited in these three layers is very sensitive to the amount of the dead material.

The two plots in figure 4.4 also demonstrate the amount of deal material that an electron travels through strongly depends on the electron incidence

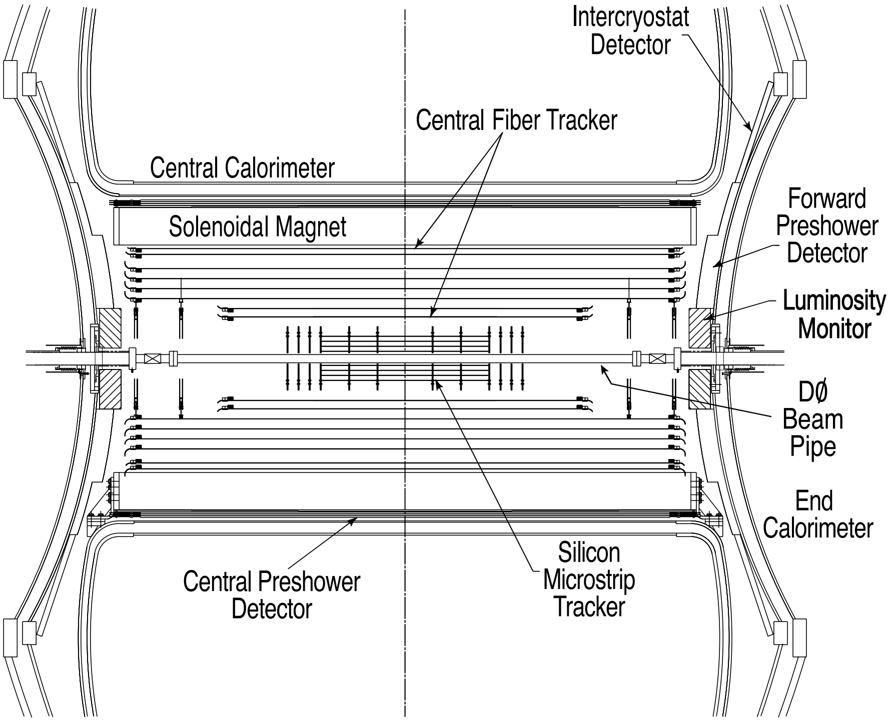

Figure 4.3: Overview of the uninstrumented (from the point of view of calorimetry) material in front of the Central Calorimeter. This drawing has been reproduced from Ref. [26] and shows a cross-sectional view of the central tracking system and in the $x - z$ plane. Also shown are the locations of the solenoid, the preshower detectors, luminosity monitor and the calorimeters.

angle. So instead of only looking at the observables averaged over our entire Z sample, we split the sample in a clever way, based on the electron energy and physics η (which is related to angle of incidence on the dead material). We define five bins in the absolute value of electron physics η ($|\eta_{\text{phys}}|$) which is used as a measure of the angle of incidence on the dead material. The exact definition is given in table 4.2. We classify these events into 15 distinct categories according to the $|\eta_{\text{phys}}|$ bin of each of the two electrons without distinguishing the leading and the subleading electron to avoid having to worry about the calorimeter energy resolution. Therefore we have 15 unique categories, which are defined in table 4.3.

To compare the different EM fractions for electrons from $Z \to ee$ be-

bin 0: $|\eta_{\text{phys}}| < 0.2$
bin 1: $0.2 \leq |\eta_{\text{phys}}| < 0.4$
bin 2: $0.4 \leq |\eta_{\text{phys}}| < 0.6$
bin 3: $0.6 \leq |\eta_{\text{phys}}| < 0.8$
bin 4: $0.8 \leq |\eta_{\text{phys}}|$

Table 4.2: Definition of bins in electron $|\eta_{\text{phys}}|$.

Category	Combination of η_{phys} bins
10	0 - 0
11	0 - 1
12	0 - 2
13	0 - 3
14	0 - 4
15	1 - 1
16	1 - 2
17	1 - 3
18	1 - 4
19	2 - 2
20	2 - 3
21	2 - 4
22	3 - 3
23	3 - 4
24	4 - 4

Table 4.3: Definition of "η categories" for $Z \rightarrow ee$ events.

tween data and the simulation, we make use of a combination of slow[2] first principles calculations and parametrized Monte Carlo. Based on the single electron events from the detailed simulation, we construct a parameterisation of the mean EM fractions and fluctuations as a function of true electron energy and η_{phys}. The single electrons are produced at different values of energy and η_{phys} and span the entire region of the energy/η_{phys} plane that is relevant for $Z \rightarrow ee$.

Figure 4.5 shows the data/MC comparison of the EM fractions of categories 10 and 23 respectively, in which there is this clear discrepancy between the data and simulation. The less energy in the first EM layer and more energy in the third EM layer from the simulation than from the data means, the electron shower is developing a littler later in the simulation than in the data, which also proves the underestimation of the dead material in the simulation. Figure 4.6 shows the means of the EM fractions for all EM layers and for all categories; separately for data and the simulation. We plot the data/simulation ratio for each of the mean EM fractions in figure 4.7. Although the data/MC disagreement(the ratio deviation from unity)that we see in figure 4.7 is not caused alone by the missing dead material(for example, the missing layer-intercalibration), it certainly is larger than what one would expect.

Now we need to add some additional uninstrumented material to the detector model and we chose a relatively low-Z material, namely copper, and place it inside the solenoid. More precisely, the shape of this chunk of copper is cylindrical, it has the same axis of rotational symmetry as the solenoid, and it extends over the whole length in z of the solenoid. The shape of the missing material is driven by the observation that the material in front of the central calorimeter all have a geometry that is close to cylindrical. We use the detailed first principles simulation to simulate single electrons with different amount of missing material added. Again, we build a parametrized model of the mean EM fractions and the fluctuations around the average. We take the number of radiation lengths(nX_0) of the missing material as the free parameter.

As shown in figure 4.7, we fit each of the data/MC ratios with a flat line and sum the fitted χ^2 from the three fits. Due to the small energy deposit in EM4, we do not include EM4 in our fits. The number of degrees of freedom for the combined χ^2 is $3 * 15 - 3 - 1 = 41$. The minimization of the χ^2 in the fit is shown in Fig. 4.8. The result of the minimization and the fit results of the per-layer constants for the optimal value of nX_0 are summarized in Tab. 4.4.

---

[2] Here, “slow” mainly means we used a smaller step size than in the standard full MC when simulating the interaction between an electron or photon and the detector material. So more time is taken to generate full MC events.

Additional material: $\mathrm{nX}_0 = 0.1633 \pm 0.0095$

Per-layer constants: $c(\mathrm{EM1}) = 1.0064 \pm 0.0013$
$c(\mathrm{EM2}) = 1.0001 \pm 0.0007$
$c(\mathrm{EM3}) = 0.9833 \pm 0.0008$
$c(\mathrm{EM4}) \simeq 1.05$

Table 4.4: Summary of the results of the adjustment of nX_0.

As a cross-check, we repeat the fit for nX_0, separately for each of the three layers. The results are summarized in figure 4.9. Good agreement is found between the results from each of the individual layers.

After adding the missing material into the full MC, we rederive the E-loss corrections and energy resolution function for this measurement and we interpret the small residual deviations from unity in the per-layer factors as layer-intercalibration gain factors that we use to correct the data. Figure 4.10 is an equivalent of Figure 4.5, except that the optimal value of nX_0 has been used and that the layer-intercalibration has been applied. Figure 4.10 is showing we have achieved a lot better agreement between the data and simulation after we add the missing material.

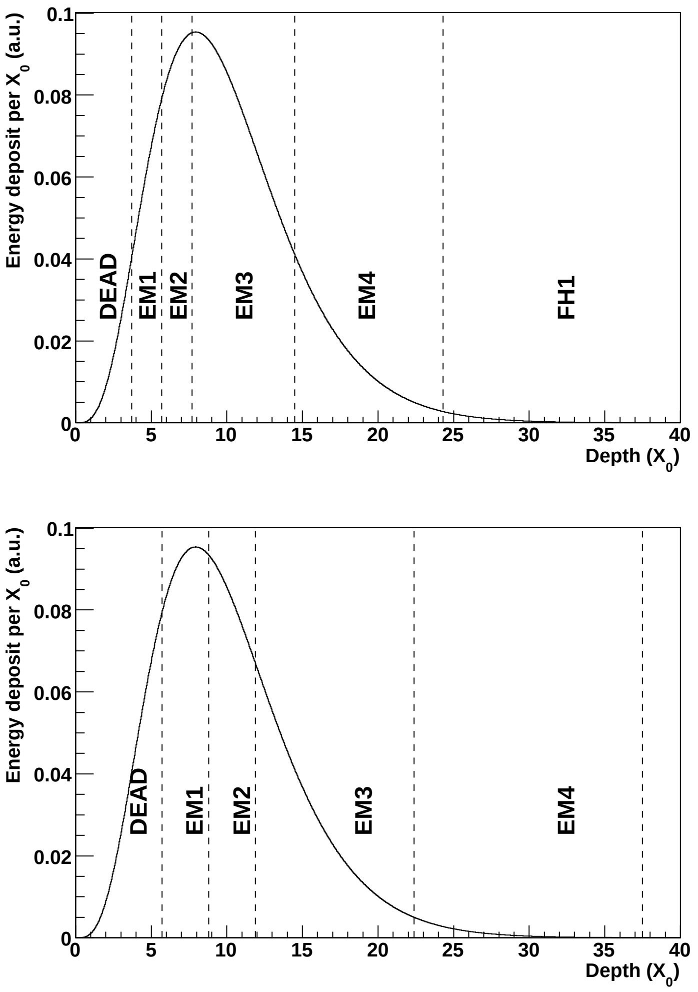

Figure 4.4: Top: Average longitudinal profile of showers from electrons with E = 45 GeV. Assuming normal incidence, the position of the active parts of the CC are also indicated. Bottom: The same average shower profile, but this time the active parts of the CC are indicated for highly non-normal incidence (specifically $\eta_{\mathrm{phys}} = 1$).

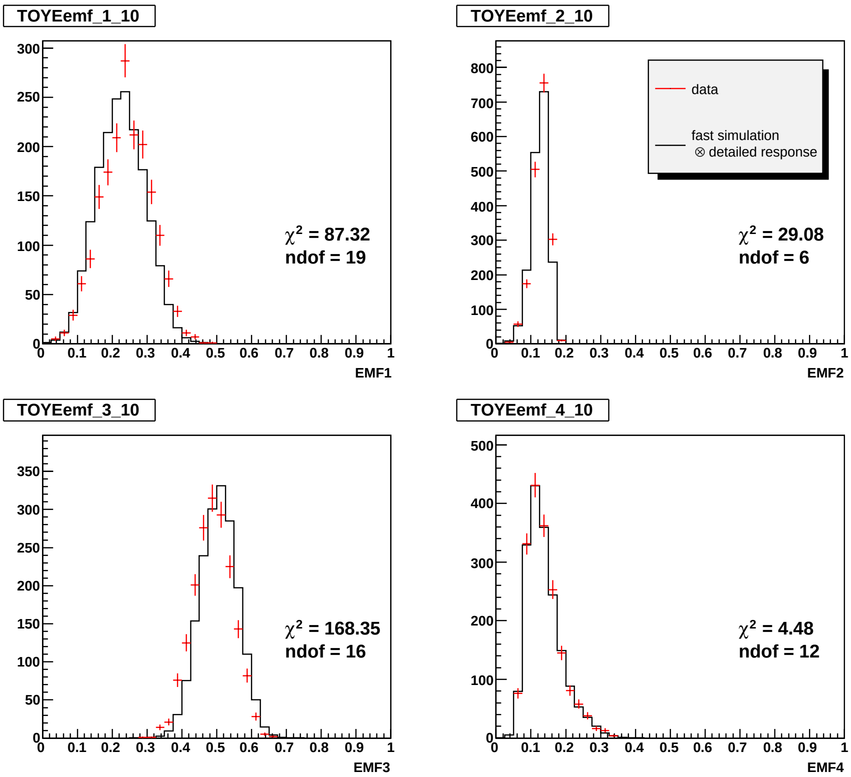

Figure 4.5: Comparison of EM fractions for electrons from $Z \to ee$ events in category 10 in data and simulation. The four individual plots show the energy fraction in each of the four EM layers. The detailed response simulation uses the default accounting of dead material.

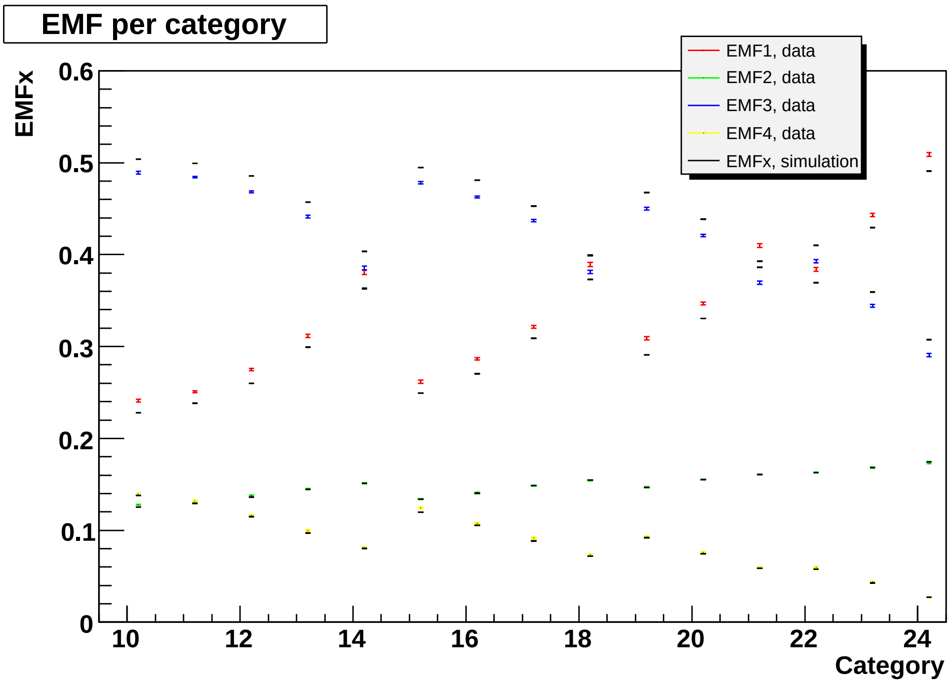

Figure 4.6: Summary of the means of the EM fraction distributions in $Z \rightarrow ee$ events for each of the four EM layers and each of the 15 η categories; separately for data and simulation.

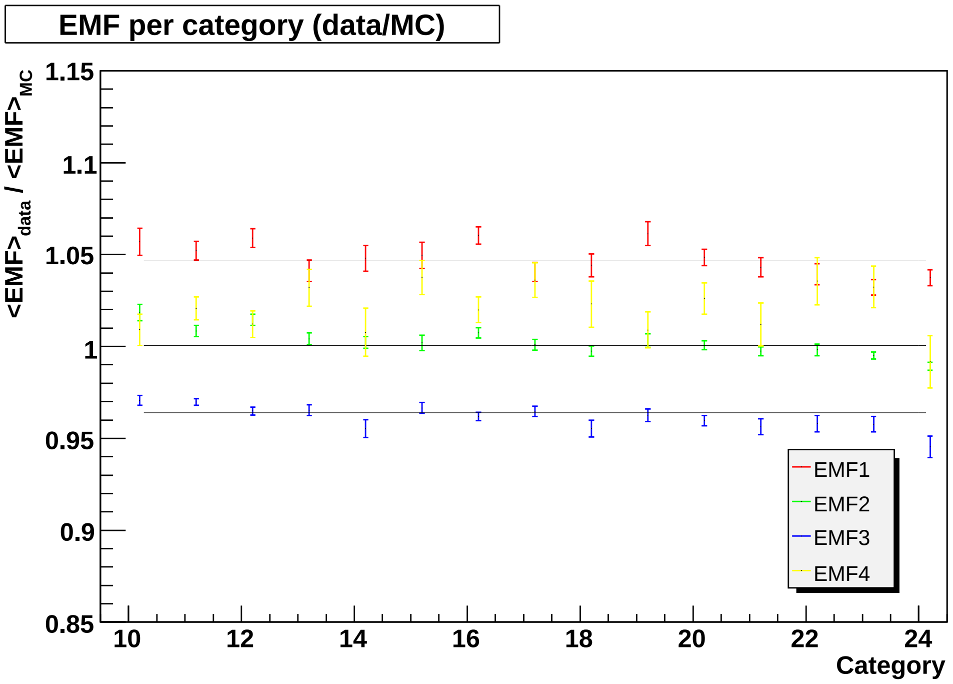

Figure 4.7: Summary of the data/simulation ratios for the means of the EM fraction distributions in $Z \rightarrow ee$ events for each of the four EM layers and each of the 15 η categories. Each of the three horizontal lines indicates the result of a fit of a common constant to the the 15 data points from a given EM layer. The fit was performed for EM1, EM2 and EM3. EM4 is not included because of the smallness of the energy deposits in it, especially at non-normal incidence.

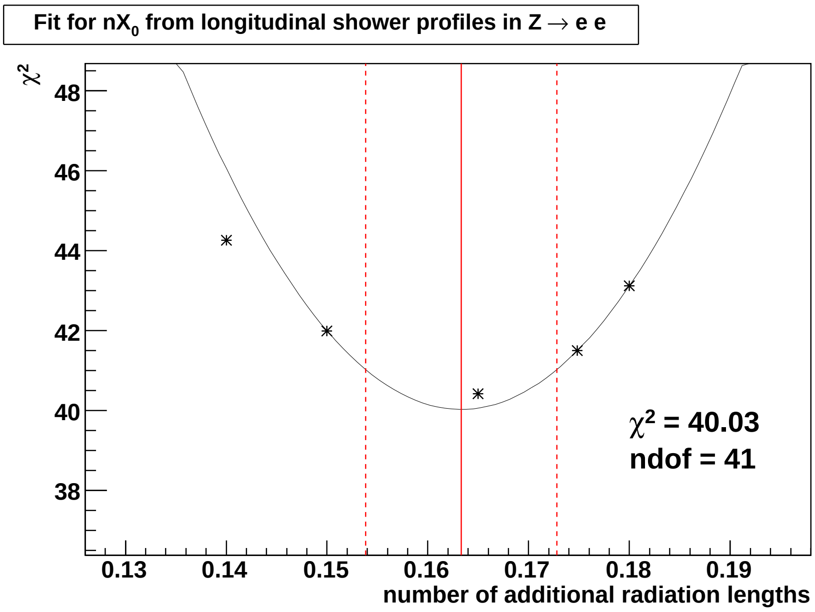

Figure 4.8: Fit for nX_0, the amount of uninstrumented material (in radiation legths) missing from the nominal material map in the detailed simulation of the DØ detector. The five stars indicate the value of the combined χ^2 for EM1-EM3, evaluated for five values of nX_0. A parabola is fit through these points in order to determine the minimum of the combined χ^2. Also shown in the figure are the value of the combined χ^2 at its minimum as well as the one-sigma variations of nX_0.

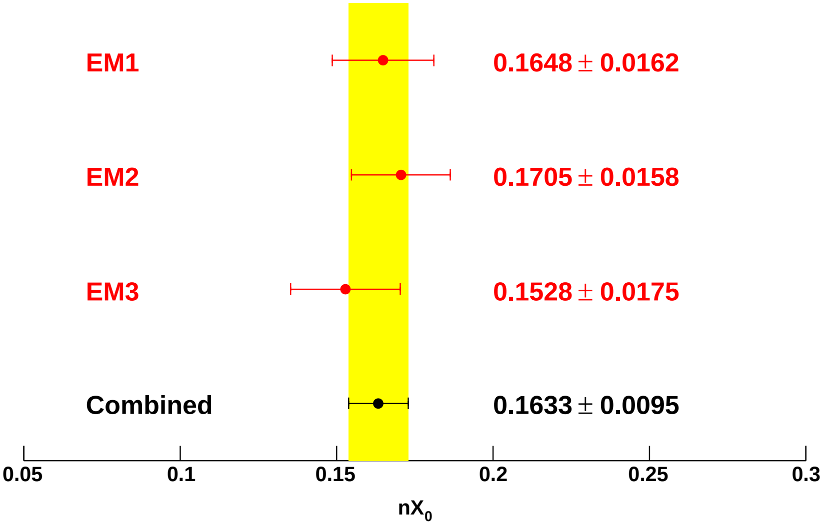

Figure 4.9: Stability check: results of the fit for nX_0, performed separately for each of the three layers (EM1, EM2 and EM3). The result of the combined fit is also shown for comparison.

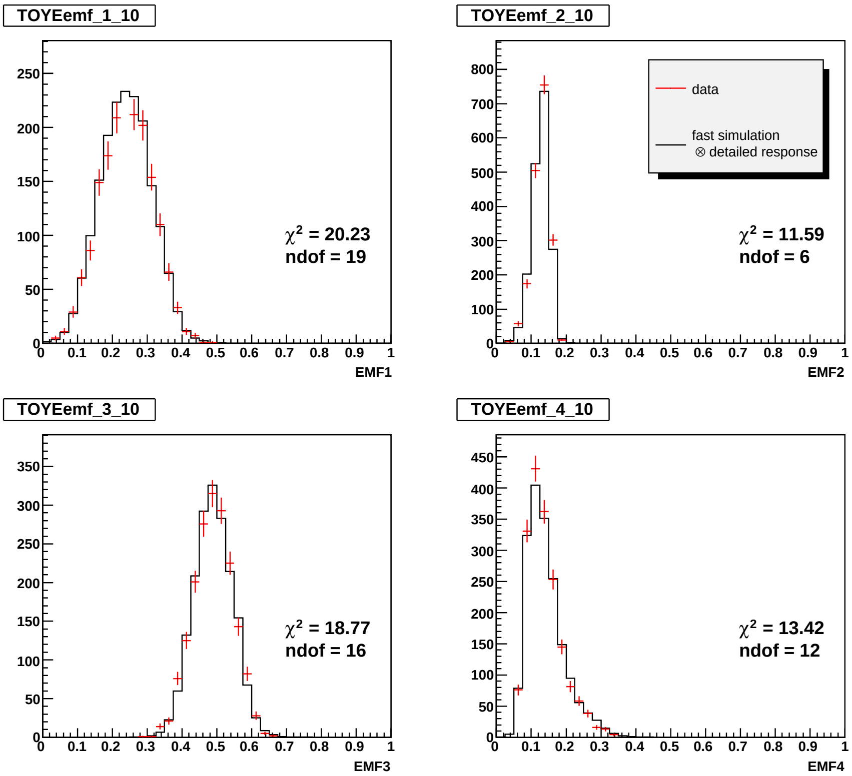

Figure 4.10: Comparison of EM fractions for electrons from $Z \rightarrow ee$ events in category 10 in data and simulation. The simulation used here includes $\mathrm{nX}_0 = 0.1633$ radiation lengths of extra uninstrumented material in front of the CC calorimeter. The four individual plots show the energy fraction in each of the four EM layers.

Chapter 5

Event Generation

The first step of the fast simulation is the event generation. Here the concise introduction will follow references [39] [40] [28].

5.1 Boson Production and Decay

At the Tevatron $p\bar{p}$ colliders large numbers of $W^{\pm}$ and Z^0 bosons are produced, which are important to measure electroweak parameters, probe the internal structure of nucleons, and monitor the collider luminosity. Any deviations of the observation from the theoretical prediction may imply new gauge interactions, supersymmetry, particle compositeness, or extra spatial dimensions. Understanding the boson production will also be crucial to the new physics searches since the Standard Model $W^{\pm}$ and Z^0 processes are the major irreducible backgrounds to these searches. At hadron colliders, the massive electroweak bosons are produced predominantly via quark-antiquark annihilation and detected by the decay into a pair of leptons. Typical W or Z observables are modified by QCD and electroweak radiation from the hadronic initial state; production, propagation, and decay of massive bosons; and electroweak radiation from the leptonic final state. Fig. 5.1 shows the lowest order diagrams for Z and W^+ boson production.

For a process ($p\bar{p} \to V$) (V stands for either the W or the Z intermediate vector boson) in the proton-antiproton collisions at the hadron collider, the parton-level cross section $\hat{\sigma}$ can be calculated as a function of the quark momenta, and then interplays with the distribution of quark momenta inside the proton and the antiproton

$$\sigma = \sum_{i,j} \int \int dx_1 dx_2 f_{i/p}(x_1, \hat{s}) f_{j/\bar{p}}(x_2, \hat{s}) \hat{\sigma}_{ij}(\hat{s}) \tag{5.1}$$

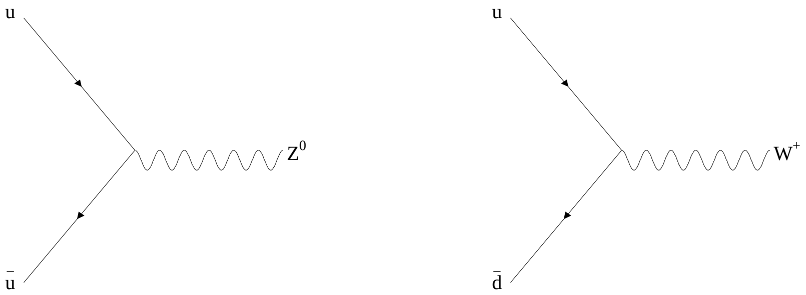

Figure 5.1: Lowest order Feynman diagrams for Z and W^+ boson production.

where the indices i and j run over the contributing quark flavors. The probability density functions f are parton distribution functions (PDFs). The distributions are functions of x (the fraction of the hadron momentum carried by the parton), and of $\hat{s}$ (the energy of the parton-parton collision). The integration is over the partonic momentum fractions x_1 and x_2, and the summation is over the relevant parton flavors.

The parton-level cross section for $q\bar{q}' \rightarrow V$ is given by

$$\hat{\sigma_{ij}}(\hat{s}) = \frac{1}{3}\frac{|V_{ij}|^2}{3\pi}\left(\frac{GM_V^2}{\sqrt{2}}\right)^2 \frac{\hat{s}\ \Gamma_V^2/M_V^2}{(\hat{s}-M_V^2)^2+(\hat{s}\Gamma_V/M_V)^2} \tag{5.2}$$

where V is the CKM matrix named after Cabibbo, Kobayashi and Maskawa and describes the quark mixing, G is the Fermi constant, and M_V and Γ_V are the mass and the total decay width of the boson respectively. The factor 1/3 in front accounts for the fact that the colliding partons must have the same color. The resonance shape is the relativistic Breit-Wigner distribution, the $\hat{s}$-dependent factor in $\hat{\sigma}$ above.

The non-zero transverse momentum of the W and Z bosons is mainly due to the initial gluon radiation off the interacting quarks and the initial transverse momentum of the interacting quarks. Higher order processes such as Gluon Compton scattering can also produce the W and Z bosons with significant transverse momentum. Figure 5.2 and 5.3 show the Feynman diagrams for the initial state radiation and Compton scattering in the W^+ and Z production, respectively.

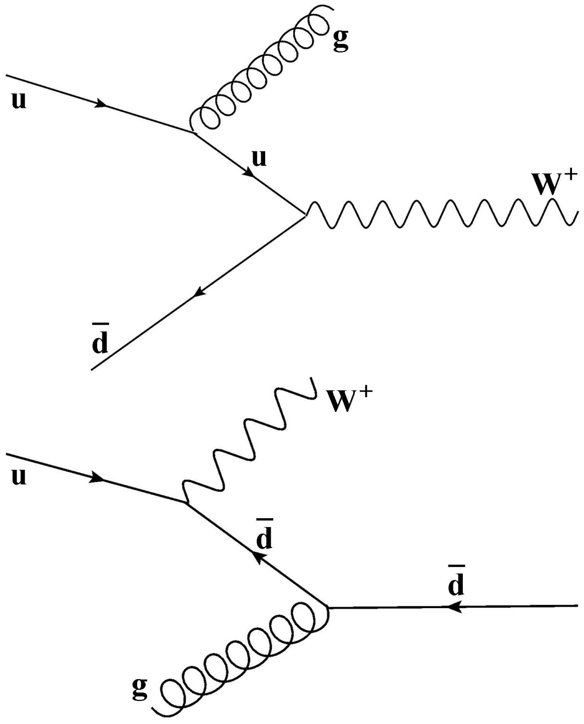

Figure 5.2: Initial state gluon radiation(Top) and Compton scattering(Bottom) in W^+ production.

Since W and Z bosons are unstable particles, they can decay into quark pairs(except to the higher-mass top quark) or other stable particles, such as leptons(figure 5.4), etc. Decays to quark pairs are not observable due to the large direct quark jets background. Decays to $\tau \to \nu_\tau$+hadrons are precisely measured and become a background for the electron channel decay. Since the thesis is about the W mass measurement in electron decay channel $W \to e\nu$, we restrict the discussion to the direct electronic decays. In the rest frame of the boson, the electron and neutrino are back-to-back and have the same energy as half the original W mass. The decay can be completely specified from the boson 4-vector by fixing the polar and azimuthal angles, θ and ϕ, of either decay product in the boson rest frame. The angles distributions depend on the boson polarization. The θ distribution of the electron in the W rest frame is given by the famous V-A coupling formula [40]

$$P(\theta) \propto (1 - \lambda Q \cos\theta)^2 \tag{5.3}$$

where λ is the W helicity, assumed to be ±1 and aligned along the $p\bar{p}$ axis, Q

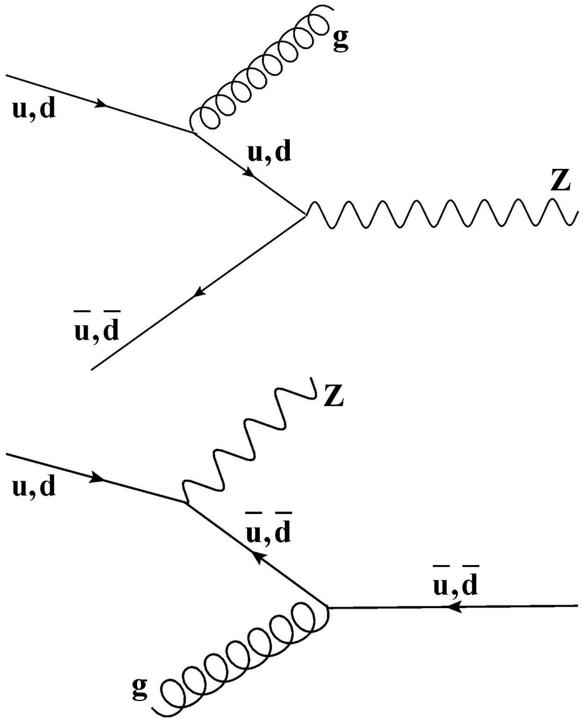

Figure 5.3: Initial state gluon radiation(Top) and Compton scattering(Bottom) in Z production.

is the W charge, and θ is the angle between the electron and the proton beam axis.

Figure 5.5 shows the spin states in W^+ production and decay[37]. In W boson production, because of the V-A structure of the weak interaction, the quark spin is mostly anti-collinear with its momentum direction(left-handed) and otherwise for the antiquark. Both spins are preferentially aligned in the $-z$ direction. Therefore, in the left one of figure 5.5 of the valence quark interaction, the outgoing positron will preferentially have its momentum pointing in the $-z$ direction and introduce a cross section dependence on the angle $d\sigma/d\cos\theta \approx (1-\cos\theta)^2$, where θ is the angle with respect to the $+z$-axis. For the interaction between two sea quarks as shown in the right panel of figure 5.5, the V-A coupling causes the positron to be emitted preferentially in $+z$ direction which is given in a cross section as $d\sigma/d\cos\theta \approx (1+\cos\theta)^2$. The opposite case, where the sea quark u is replaced by $\bar{\mathrm{d}}$, and $\bar{\mathrm{d}}$ is replaced by u, is equally probable.

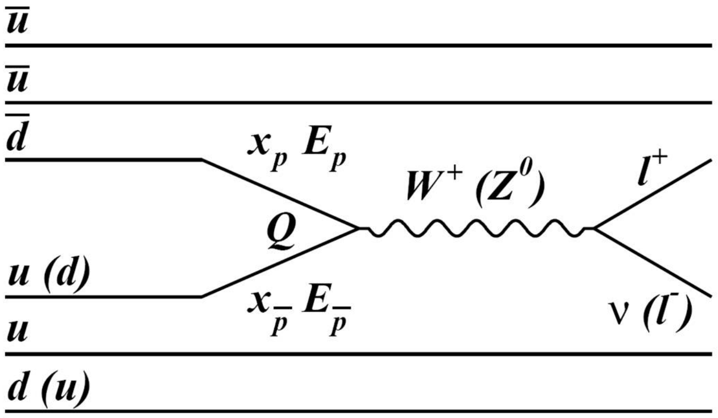

Figure 5.4: Leading order $W(Z)$ boson production and decay

5.2 Boson p_T

As discussed in chapter 3, the W boson p_T spectrum has a significant impact on the simulated $p_T(e)$ and $\not{E}_T$ spectra so an accurate description of this is an important ingredient of the W mass measurement. We used RESBOS [41] to simulate the boson production and decay process, which gives reasonable description of the transverse momentum of the vector bosons. It extends the Collins-Soper-Sterman resummation formalism[42], for on-shell vector boson production, to correctly include the effects of the polarization and the width of the vector boson to the distributions of the decay leptons. RESBOS computes the triple differential cross section $d^3\sigma/dp_T\,dy\,dm$ for Z/γ^* and W processes at hadron colliders, where p_T is the boson momentum in the plane transverse to the beam, $y = \frac{1}{2}\ln[(E + p_z)/(E - p_z)]$ is the boson rapidity and m is the boson mass. It uses a gluon resummation calculation for low boson transverse momentum p_T and perturbative QCD calculations at high boson p_T.

For low p_T W and Z bosons, the main higher order correction to the overall cross section comes from multiple soft and collinear gluon emission which is calculated using a gluon resummation technique. In impact-parameter space resummations, the W p_T spectrum is parametrized using a non-perturbative form-factor using three parameters called g_1, g_2 and g_3. The values of these three parameters need to be determined from experimental data. The Z boson p_T distribution at the Fermilab Tevatron is by far the most sensitive to the value of g_2, has limited sensitivity to g_1, and is quite insensitive to the value of g_3. We use the global fit values listed at Ref. [43] with $g_2 = 0.68 \pm 0.02$ and propagate the uncertainty on g_2 to the W mass measurement. The un-

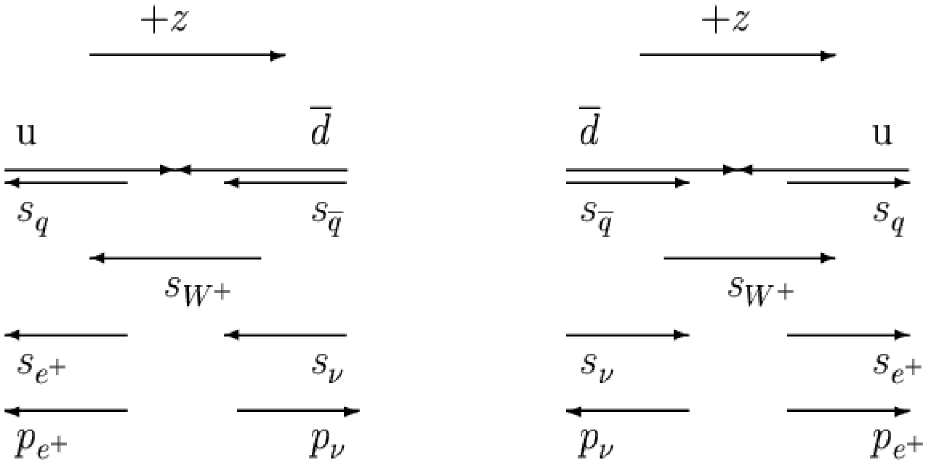

Figure 5.5: Spin states for W^+ production and decay. Left: W^+ produced with valence quarks; Right : One of the cases of W^+ production with sea quarks.(The opposite case with sea quark u and $\overline{\mathrm{d}}$ switched with each other is equally probable.)

certainties from g_1 and g_3 are negligible. Figure 5.6 shows the propagation of the error on g_2 to the measured value of the W mass uncertainty.

Table 5.1 lists the corresponding propagated uncertainty on the W mass.

	m_T fit	$p_T(e)$ fit	$\not{E}_T$ fit
$\Delta M_W/\Delta g_2(MeV)$	101	243	79
ΔM_W(MeV)	2	5	2

Table 5.1: Systematic uncertainty on W mass measurement due to g_2 uncertainty.

5.3 PDF

The partonic structure of hadrons plays a fundamental role in elementary particle physics. Parton distribution functions (PDFs) enter into the W mass measurement through their effects on the detector acceptance and kinematics of the decay electron. The PDFs are determined phenomenologically by a global analysis of experimental data from a wide range of hard-scattering processes, such as deep inelastic scattering, jet production and the W charge asymmetry. The PDFs are specified in a parameterized form at a fixed low

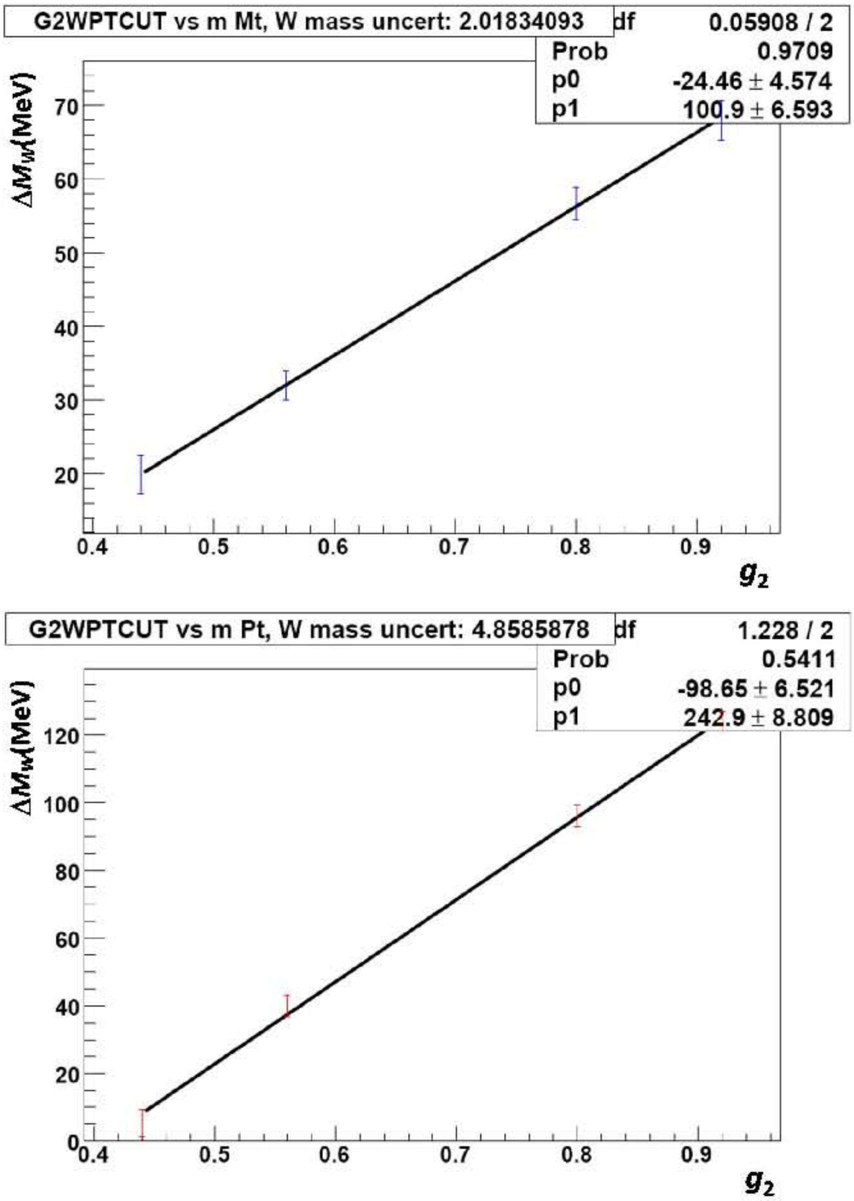

Figure 5.6: The corresponding M_W error versus g_2: top for m_T and bottom for $p_T(e)$ methods respectively

energy scale(1 GeV), from which the PDFs at high energies are determined by NLO perturbative QCD. CTEQ uses an effective global χ^2 function to measure the quality of the fit between theory and experiment. The global χ^2 is calculated by using 15 data sets from 15 differents experiments around the world. To study the uncertainties of PDF's, the variation of χ^2 is explored in the neighborhood of its minimum.

We determine the systematic uncertainty arising from the PDFs using a standard prescription for the CTEQ6.1M [44] parton distribution function. We used PYTHIA to generate $W \rightarrow e\nu$ events using the central PDF set. After passing through fast MC simulation and event selection, those events were treated as "data". Then we use the standard PDF reweighting method to generate mass templates for different "theories" involving variation of the PDF's. By performing the PDF reweighting, the statistical impact is minimized. There are 20 free parameters in the CTEQ6.1M PDF set. For the uncertainty calculation, 40 additional sets were defined by positive and negative variation of each parameter until the global χ^2 reached the 90% C.L. The default values of W mass and width used in PYTHIA are 80.450 GeV and 2.071 GeV respectively. For each PDF set, we generated 100 M_W templates centered at 80.450 GeV with a step size of 2 MeV. To determine each mass shift, we calculate the binned log-likelihood for the m_T (or $p_T(e)$, $\not\!\!E_T$) distribution using the central PDF and the 100 M_W templates for each of 40 PDF sets[45].

We use the following formula to obtain the uncertainty with 68% C.L. [46]:

$$\Delta M_W = \frac{1}{2 \times 1.6} \sqrt{\sum_{i=1}^{20} (M_i^+ - M_i^-)^2} \tag{5.4}$$

where M_i^+ and M_i^- are the W masses determined using the ith uncertainty PDF sets. The factor 1.6 is used to convert from a 90% confidence interval to the more standard 68% confidence interval.

We did the same analysis using $p_T(e)$ and $\not\!\!E_T$ methods. The final uncertainty is found to be 10 MeV for m_T method, 11 MeV for $p_T(e)$ method and 11 MeV for the $\not\!\!E_T$ method[47].

5.4 Electroweak Corrections

Radiation from the decay electron or the W boson biases the mass measurement. W or Z decays into leptons (+neutrino) through electro-weak interactions.

$$q'\bar{q} \rightarrow W \rightarrow l\nu(\gamma) \tag{5.5}$$

$$q\bar{q} \rightarrow Z \rightarrow ll(\gamma) \tag{5.6}$$

There is a certain probability that an electron will radiate a photon, which will take away some of the energy of the electron. The invariant mass of leptons (or lepton + neutrino) is lower than the original boson. The radiated photons are often collinear with the electrons and reconstructed as the same EM cluster, so modeling the photon radiation in generator and the fast simulation plays a crucial role in measuring the W mass.

The EW contributions to the W mass uncertainty mainly come from the following sources:

- photon radiation off the incoming quarks
- photon radiation off the W propagator
- photon radiation off the final-state electron (the most important contribution)
- all other EW processes: virtual corrections via photons or Z bosons

The dominant effect from EW corrections to the W mass measurement comes from radiation of a single photon from the final state charged lepton. The next-largest effect is due to two final state photon radiations. These processes are simulated by combining the PHOTOS program [48] with RESBOS.

PHOTOS is a universal Monte Carlo event generator simulating QED final-state radiation corrections in decays of particles and resonances. It takes the RESBOS output as the input to add the final state radiation and can radiate up to two photons off one electron.

The photon energy cut, controlled by the input parameter δ_s, is made on the fraction of the parton's energy carried by the emitted photon in the parton-parton center of mass system. Events with photon energy below the cut will be thrown away:

$$E_\gamma > \delta_s\sqrt{\hat{s}}/2 \tag{5.7}$$

where $\sqrt{\hat{s}}$ is the parton energy in the parton-parton center-of-mass system. So $\delta s = 0.001$ corresponds to the energy $E_\gamma = 40$ MeV. Events with photon $E_\gamma < \delta_s\sqrt{\hat{s}}/2$ are considered as two-body events.

In order to study the effect of varying the photon energy cut, we change δs from 0.00025 to 0.02, corresponding the minimum photon energy from 10 MeV to 800 MeV[49]. We run RESBOS+PHOTOS with variant δs, then go

δs ($\times 10^{-3}$)	$E_\gamma cut$ (MeV)	ΔM_W (m_T) (MeV)	ΔM_W ($p_T(e)$) (MeV)	ΔM_W ($\not{E}_T$) (MeV)	ΔM_Z (Z Mass) (MeV)	$\Delta(\frac{M_W}{M_Z})$ (m_T) ($\times 10^{-5}$)	$\Delta(\frac{M_W}{M_Z})$ ($p_T(e)$) ($\times 10^{-5}$)	$\Delta(\frac{M_W}{M_Z})$ ($\not{E}_T$) ($\times 10^{-5}$)
0.25	10	-25 ± 3	-23 ± 4	-22 ± 4	-34 ± 2	5.5	7.7	8.8
0.5	20	-29	-29	-27	-30	-2.8	-2.8	-0.6
0.6	24	-24	-27	-24	-32	4.6	1.3	4.6
0.7	28	-24	-29	-19	-32	4.6	-0.85	10.0
0.8	32	-21	-23	-20	-33	8.9	6.7	10.0
1	40	-20	-20	-20	-27	4.2	4.2	4.2
3	120	-17	-22	-14	-21	1.7	-3.8	5.0
5	200	-10	-13	-12	-15	3.5	0.25	1.3
10	400	0	0	0	0	0	0	0
15	600	5	8	6	11	-5.2	-1.9	-4.1
20	800	18	20	15	26	-5.4	-3.2	-8.7

Table 5.2: Mass shift of W and Z due to δs variation.

through the fast simulation, and fit the output using the mass templates with δs=0.01. δs=0.01 is the default value in our simulation. The variation range from 0.00025 to 0.02 well covers the default value. We also go through the same procedure for Z boson.

Table 5.2 shows the mass shifts of W and Z, and their mass ratio. As we lower the photon cut, more events will have FSR, so the W and Z mass will shift lower. Among three methods using m_T, $p_T(e)$ and $\not{E}_T$, the method $p_T(e)$ is most affected just as we expected. Z mass is more vulnerable to the photo radiation because it decays into two electrons and its mass heavily relies on the reconstructed electron energy. Since we use $Z \rightarrow ee$ events to do the calibration, what really matters is the W/Z mass ratio. We plot the mass ratio versus the photon energy cut and fit the plots with a flat line that gives a good $\chi^2/d.o.f.$ We take the fitted value multiplied by the Z mass to estimate the W mass uncertainty due the photon energy cut. So it introduces 2 MeV(m_T), 1 MeV($p_T(e)$) and 3 MeV($\not{E}_T$) into the W mass uncertainty.

The effect of the minimum distance between the radiated photon and the electron on the W mass measurement is negligible. We study the effects of ISR, ISR-FSR interference and other EW corrections by using the WGRAD(ZGRAD)[50][51] program. WGRAD(ZGRAD) provides an option that allows us to include FSR-only correction or the full electroweak corrections. By turning on and off this option and letting the generated events pass through the fast simulation, we measure the relative W mass shift between the two op-

cone size	ΔM_W (m_T) (MeV)	ΔM_W ($p_T(e)$) (MeV)	ΔM_W ($\not\!\!E_T$) (MeV)	ΔM_Z (Z Mass) (MeV)	$\Delta(\frac{M_W}{M_Z})$ (m_T) ($\times 10^{-5}$)	$\Delta(\frac{M_W}{M_Z})$ ($p_T(e)$) ($\times 10^{-5}$)	$\Delta(\frac{M_W}{M_Z})$ ($\not\!\!E_T$) ($\times 10^{-5}$)
0.2	-18±3	-16±4	-8±4	-21±2	0.57	2.8	11.5
0.25	-7	-8	-1	-6	-1.9	-3.0	4.7
0.3	0	0	0	0	0	0	0
0.35	6	7	0	7	-0.19	0.9	-6.8
0.4	12	15	3	16	-2.3	0.98	-12.2

Table 5.3: Mass shift of W or Z due to change of photon merge cone size

tions, which is taken as the uncertainty due to the effect of ISR, ISR-FSR interference and other EW corrections. The final uncertainty is found to be 5 MeV for m_T method, 5 MeV for $p_T(e)$ method and 5 MeV for $\not\!\!E_T$ method.

Besides the uncertainty that comes from the theoretical prediction on photon radiation, our treatment of radiated photons could also give us some biases. If a radiated photon is close to the electron, it will deposit most of its energy in the electron shower, which we need to take into account in our fast simulation. Here is how we treat photons in the fast simulation. If a photon is within the 0.3 cone around an electron, it will be merged into this electron and removed from the recoil system, otherwise it will be kept in the recoil system. The 0.3 photon merge cone size will bring up some uncertainty into W mass because some photons will change the electron shower shape and not be reconstructed as an EM object.

To quantify the impact of photon merge cone size change, we vary the cone size as 0.2, 0.25, 0.3, 0.35, 0.4 to see W and Z mass shift. Table 5.3 lists the mass shifts of W and Z. From the table, one can see that the W values of $p_T(e)$ and m_T are quite sensitive to the change of cone size while $\not\!\!E_T$ is not very sensitive. This is what we expected. The Z mass is even more sensitive to the change of cone size because in each Z event there are two electrons, and therefore the Z is more likely to have FSR than the W. Figure 5.7, shows the ratio of fitted W mass to Z mass versus cone size using m_T, $p_T(e)$ and $\not\!\!E_T$. The ratio is fit with a horizontal line, and the uncertainty propagated into the W mass results in uncertainties 1 Mev, 1 MeV and 5 MeV. As discussed before, W p_T(e), m_T and Z Mass are all sensitive to the cone size change. When we take the ratio between W and Z, the uncertainties cancel each other. $\not\!\!E_T$ is not sensitive to the cone size change, so its uncertainty does not cancel with the uncertainty in the Z mass as well.

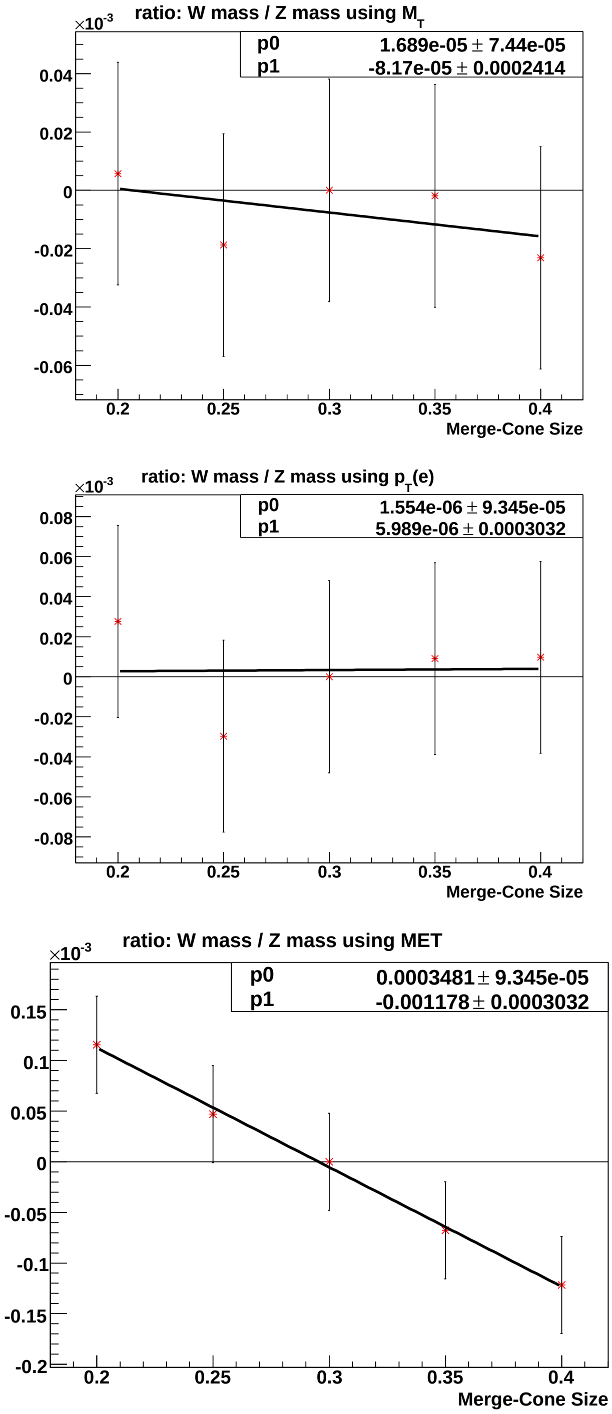

Figure 5.7: Mass ratio (W/Z) vs Photon Merge Cone Size: m_T(top), $p_T(e)$(middle) and $\not\!\!E_T$(bottom)

Chapter 6

Efficiency

A set of selection criteria are used to select electrons and events. These criteria are powerful in rejecting the background. Meanwhile, they can also reject some good electrons and $W(Z)$ events. However, the reason the efficiency is important is not in its absolute value, but in its different dependencies, especially the kinematic dependencies(for example, the $p_T(e)$ dependence). It is the dependence that will shape the final spectrum of the three variables(M_T, $p_T(e)$ and $\not\!\!E_T$) we are using to measure the W boson mass. Because of the existence of crack in the detector, we can only reconstruct events with electrons pointing into the fiducial region, which defines the geometric acceptance. The imperfection of the detector introduces the angular dependence of the efficiency, which is not only important to the kinematic variables, but also crucial to the EM energy resolution. Aside from the intrinsic $p_T(e)$ dependence, the efficiency is also subject to effects from the recoil system(both the relative direction and the absolute magnitude of the energy from the rest of the event). The fact we are using not just one selection criteria requires some extra measures, since different criteria have different sensitivities. The SMT hit requirement is extremely sensitive to the primary vertex z-component due to the limited coverage of SMT, while the variables based on the calorimeter information is free from this problem.

To study the efficiency in the data, a method called tag-and-probe [52] is used on the $Z \to ee$ events. The basic idea is we require one of the two electrons(tag) to pass all the standard selection cuts, and also require the other electron(probe) to pass all the selection cuts except the one we want to study(for example, the track match). We also require the invariant mass of the tag and probe electron to be in the neighborhood of the well-known Z mass(70 GeV$< M_{ee} <$ 110 GeV). By means of this, we have a good handle on selecting good $Z \to ee$ electrons. Then the probe electron is used to measure the efficiency. The two electrons can switch their roles in being the tag or probe, in some cases.

6.1 Geometric Acceptance

There are 32 EM modules in the ϕ direction of the central calorimeter, each module is $2\pi/32 \sim 0.2$ radian wide in ϕ. An intra-module ϕ variable, PhiMod, is defined as fmod[1]$(32\phi/2\pi, 1.0)$ with $0 \leq \text{phiMod} < 1$. In the region of inter-modular boundaries or gaps better known as the "ϕ cracks", we have less calorimeter signal response. We exclude these regions in the data selection. so 20% of the azimuthal CC phase space is removed. At fixed η_{det} each of the EM1, EM2 and EM4 layers in an EM module consists of 2 read out cells. The central value of PhiMod=0.5 corresponds to the inter-cell boundary, the values close to 0 and 1 are the module edges. The EM3 layer is segmented twice as finely in both eta and phi (0.05 radian wide). Thus in an EM module this layer contains 8 'readout cells' at a "fixed η_{det}" each with a width of 0.05.

Due to the EM clustering algorithms and the electronics, the electron cluster angle ϕ_{EM} calculated from the electron energy deposited in the third EM layer is biased towards the center of the module [53]. Figure 6.1 (Left) shows the PhiMod bias vs the PhiMod of the extrapolated track position across the module (fmod$(32\phi_{trk}/2\pi, 1.0)$). Since ϕ_{trk} is unbiased, we can see a strong tendency for the ϕ_{EM} to move towards the center of the module.

Due to the arrangement of the electrode pads in the calorimeter, the efficiency to find electron clusters varies with the ϕ of the incident particle [54]. Figure 6.1 (Right) shows the efficiency of finding an EM cluster vs PhiMod in data. For the final analysis, we only keep electrons with $0.1 < \text{PhiMod} < 0.9$.

Understanding both the efficiency and the bias is important for modeling the Z boson transverse momentum distribution in the fast simulation and further impact the electron p_T and recoil system p_T distributions. Both the efficiency and the bias are measured using electrons from $Z \to ee$ events.

6.2 Trigger Efficiency

The data used for this measurement was collected from 2002 to 2006, covering over four trigger periods, and the L1/L2/L3 requirements are different for different periods. The trigger efficiency is measured using the tag-and-probe method on $Z \to ee$ events. To pass the trigger requirement, an electron should have a matching trigger object at each level which passes all cuts for

---

[1] fmod(numerator,denominator) is the floating-point remainder of numerator/denominator.

the corresponding trigger. The electron candidate to trigger object matching requirements are expressed in terms of $\Delta R = \sqrt{\Delta\eta^2 + \Delta\phi^2}$ for L1, L2 and L3. Figure 6.2 shows the trigger efficiency as a function of $p_T(e)$ for the four trigger periods.

6.3 Preselection Efficiency

Preselection is used to find an electron as a calorimeter cluster which passes the EM fraction and isolation requirements $f_{EM} > 0.9$ and $f_{iso} < 0.15$. Tag-and-probe is used on the $Z \to ee$ events to measure this efficiency. Since the preselection is the first step to select an electron cluster formed in the calorimeter, we do not apply any calorimeter requirements on the probe electron. Instead, the tracking information is used in combination with the tag electron to select good $Z \to ee$ events. Figure 6.3 shows the measured preselection efficiency as a function of η_{det} in the regions used ($|\eta_{det}| < 1.05$) in this analysis. The only variation occurs in regions vetoed by the fiducial requirements. We do not observe $p_T(e)$ dependence of the preselection efficiency for $p_T(e) > 25$ GeV so no $p_T(e)$ dependence is modeled for the preselection efficiency.

6.4 HMx Efficiency

HMx is a variable to characterize the electron shower shape. Since HMx has 7(8) variables as the input, which includes both transverse and longitudinal shower information, we would naturally expect it to have η_{det} or even $p_T(e)$ dependence.

The η_{det} dependence is measured using the tag-and-probe method on $Z \to ee$ events, as shown in figure 6.4. Due to correlation between the η_{det} and $p_T(e)$ dependence for HMx, we parameterize the HMx efficiency as a 2D function of physics η and $p_T(e)$. Due to the limited statistics of the $Z \to ee$ data and the fact we are trying to model the intrinsic $p_T(e)$ dependence, we use the full MC single electron events for this 2D parametrization. It is defined simply as the ratio of the number of single electron MC events which pass the full ID requirements including f_{EM}, f_{iso} and HMx to the number which pass the preselection. The result is shown in figure 6.5. Here we can see significant overall inefficiency and kinematic variation along with the strong coupling between physics η and $p_T(e)$.

6.5 Tracking Efficiency

The track-matching requirement is the spatial track match plus at least one SMT hit and does not include the the track p_T cut. The tracking resolution and p_T cut are modeled separately in the fast MC. As briefly discussed at the beginning of this chapter, the limited SMT coverage introduces a strong coupling between the η_{phys} and primary vertex z position for the tracking efficiency, which is measured using the tag-and-probe on the $Z \rightarrow ee$ data, as shown in figure 6.6.

To determine the dependence of the tracking efficiency on electron p_T and η_{phys} , the same single electron full MC sample is used as previously. Similar to the HMx efficiency, the tracking efficiency is a relative efficiency, defined as the efficiency with which an electron that passes all of the calorimetric (EMID) requirements also passes the track-matching requirement. Figure 6.7 shows the tracking efficiency as a function of $p_T(e)$ for different η_{phys} bins.

6.6 $u_{||}$(Recoil Related) Efficiency

Among the electron selection cuts, isolation, HMx and track match are heavily affected by the recoil system, which is mainly composed of hadronic jets, along with the residuals from spectator parton interaction, electron noise and pileup from previous bunches. When the recoil system is not too far from the electron, it will change the electron shower shape and its isolation value. The recoil system also brings tracks, and therefore affects the track match. The projection of the recoil p_T to the electron transverse direction, $u_{\|}$, is used to parameterize the recoil effect on the electron selection criteria (electron isolation, HMx and track matching).

First, it is important to understand the $u_{||}$ efficiency difference [55] in Z and W events, I will present the discussion using the full MC events. To measure the $u_{\|}$ efficiency in full MC, we used two different methods: the truth method and the tag-and-probe method. For the truth method, since in the full MC samples we know we have true electron(s) which decay from the Z or W boson, we simply remove the cuts under study (isolation, HMx and track matching), and then apply those cuts to determine the efficiency. We did this for both W and Z full MC samples. For the tag-probe method, we only can use $Z \rightarrow ee$ events. We require one tag electron that passes tighter selection cuts, and then check the second electron. This method can be applied for real data analysis where the truth information is not available, although background subtraction is needed.

Figure 6.8 shows the $u_{||}$ efficiency using the truth and tag-and-probe method

	p_0 (GeV)	p_1 (GeV^{-1})	p_2
$Z \to ee$(truth)	1.473 ± 0.272	0.0071 ± 0.0004	0.8336 ± 0.0006
$Z \to ee$(tag-probe)	1.510 ± 0.290	0.0070 ± 0.0005	0.8442 ± 0.0007
$W \to e\nu$(truth)	1.064 ± 0.156	0.0078 ± 0.0003	0.8260 ± 0.0004
$W \to e\nu$(truth: fix p0)	1.473(fixed)	0.0083 ± 0.0002	0.8255 ± 0.0004

Table 6.1: p_0, p_1, p_2 of $Z \to ee$ and $W \to e\nu$

in $Z \to ee$ events. The distribution is fitted with a function of the form:

$$\epsilon(u_{\|}) = p_2 \begin{cases} 1 & \text{for } u_{\|} < p_0 \\ 1 - p_1(u_{\|} - p_0) & \text{otherwise} \end{cases} \tag{6.1}$$

The parameter p_2 is an overall efficiency ($\epsilon_{iso} \times \epsilon_{HMx} \times \epsilon_{trk}$), p_0 is the value of $u_{\|}$ at which the efficiency starts to decrease as a function of $u_{\|}$, and p_1 is the rate of decrease. If $u_{\|}$ is negative, the efficiency is basically flat because the recoil system and the electron are on the opposite hemisphere, and thus the recoil system has little effect on the electron identification. Once $u_{\|}$ is greater than p_0, the recoil system is getting closer to the electron and starts to distort the electron identification. The more positive $u_{\|}$ gets, the lower efficiency the electron will be found at. The slope parameter p_1 indicates how the electron selection will be affected by the recoil system. The fitted parameters using the truth method and tag-probe method are listed in table 6.1. The parameter values in table 6.1 clearly demonstrate the two methods give very consistent results, which means eventually we could use the tag-probe method when dealing with the data.

Figure 6.9 shows the $u_{\|}$ efficiency using the truth method in $W \to e\nu$ events. The fitted values are also listed in table 6.1. In figure 6.9, the left one allows the parameter p_0, the turning point, to float, which gives the slope $p_1 = 0.0078 \pm 0.0003$ GeV^{-1}, about 1.4σ larger than $p_1 = 0.0071 \pm 0.0004$ GeV^{-1} obtained from Z . However, we also notice the turning point is different between Z and W, which is highly correlated with the slope. To really compare the slopes obtained from Z and W, we fix the turning point at the same value. The right plot in Fig. 6.9 shows the same distribution as the left one, but with fixing the turning point p_0 at the value obtained from Z (left plot in Fig. 6.8). We find that the slope for W is even bigger with $p_1 = 0.0083 \pm 0.0002$ GeV^{-1}, 2.7σ larger than p_1 in Z.

One might wonder why Z and W give different $u_{\|}$ slope. The left picture in Fig.6.10 shows an event of $Z \to ee$. When we shrink each vector in this

	p_0 (GeV)	p_1 (GeV^{-1})	p_2
$Z \rightarrow ee$(truth)	1.137 ± 0.231	0.0077 ± 0.0004	0.8338 ± 0.0007
$Z \rightarrow ee$(tag-probe)	1.192 ± 0.247	0.0076 ± 0.0005	0.8443 ± 0.0007
$W \rightarrow e\nu$(truth)	1.064 ± 0.156	0.0078 ± 0.0003	0.8260 ± 0.0004
$W \rightarrow e\nu$(truth: fix p0)	1.137(fixed)	0.0078 ± 0.0002	0.8259 ± 0.0004

Table 6.2: p_0, p_1, p_2 of $Z \rightarrow ee$ after scaled to W and $W \rightarrow e\nu$

event by a factor 80.419/90.188, i.e. the boson mass ratio, and replace one of the electrons by a neutrino, we then get a $W \rightarrow e\nu$ event, as shown in the right hand picture. So the open angle between the electron and the hard recoil and their energy ratio is the same in the two pictures. On the first (linear) order approximation, we would expect the electrons in this particular Z and W event have the same efficiency. However, the hard recoil system in W event is softer, therefore gives a smaller $u_{||}$ when projected onto the electron direction. This translates into the fact that W $u_{||}$ efficiency presents a smaller turning point and steeper slope, as we have just seen. So if we scale the $u_{||}$ in Z by a factor 80.419/90.188, we should be able to get the same $u_{||}$ efficiency as W. Fig.6.11 shows the Z $u_{||}$ efficiency using the truth and tag-probe method after scaling to the W. Table 6.2 lists the new fitted parameters from Z by scaling it to W and the original values from W. These numbers clearly show the turning point and slope values from scaled Z agree very well with W.

We have been focusing on p_0 and p_1 because we only care about the turning point and the slope when parameterizing the efficiency in the fast simulation. However, we also have the plateau(p_2) difference between Z and W, and even between the truth and tag-and-probe method in Z. For Z events, the efficiency plateau difference between the truth and tag-and-probe method is about 1%, which is reasonable since we have a 2%[52] systematic bias due to this tag-and-probe method. As we have previously mentioned, when we transfer for a Z event to a W event, the hard component of the recoil system gets softer. But the soft component of the recoil system is approximately the same for Z and W, which is composed of the spectator parton interaction, electronic noise and pileup, etc. Since W electrons are softer than Z electrons on average, W electrons are more affected by the soft recoil and show a slightly lower average efficiency.

When we model the $u_{||}$ efficiency in the fast simulation, however, we need to make a little adjustment. In the fast simulation, we also model the pure p_T(e) dependence of the track match and HMx by studying the full MC single electron events that have no recoil. The $u_{||}$ efficiency, measured from full MC with the recoil, essentially consists of both the pure p_T(e) dependence and the recoil effect. When modeling the p_T(e) and the $u_{||}$ efficiency simultaneously in the fast simulation, the double counting of the pure p_T(e) dependence needs to be removed. To do the double counting removing, we perform the same procedure in the fast simulation as in full MC to measure the $u_{||}$ efficiency and compare it with the one we got from full MC. By adjusting the $u_{||}$ efficiency slope we put in the fast simulation, we can obtain the best agreement between full and fast simulation on the $u_{||}$ efficiency. This way we can get the adjusted $u_{||}$ efficiency slope for the fast simulation that is after the double-count-removing.

6.7 SET(Overall Hadronic Activity) Efficiency

The "rest of the event" mainly consists of hadronic activity from the spectator partons, additional $p\bar{p}$ interactions and the hadronic recoil that balances the vector boson. It has an important impact on the electron reconstruction and identification efficiency. SET(Scalar Transverse Energy) is a good observable to reflect the effects from the overall hadronic energy in an event. It basically accounts for the magnitude of activity in the rest of the event. The effect related to the relative direction between the electron and the rest of the event is parameterized using $u_{||}$.

Standard full MC plus overlay of collider data events are used to construct the SET efficiency model. The efficiency is parameterized versus the SET from the overlay of ZB events and applied to the total SET in the event. $Z \to ee$ full MC events passing the standard selection without recoil p_T requirement are used to derive the per-event reconstruction efficiency as a function of the SET of the ZB event used for overlay. The efficiency is defined as the number of selected events divided by the total as a function of SET. The measured SET efficiencies, separately for full MC Z and W events, are smoothed using a polynomial function with coefficients by fitting the efficiency versus SET histogram, shown in figure 6.12.

The higher p_T electron is more likely to survive the "rest of the event"to be reconstructed and pass the selection requirement. So we introduce a small multiplicative correction factor to the per-event efficiency depending on $p_T(e)$ and SET in the case of $W \to e\nu$ and two multiplicative correction factors (one per electron) in the case of $Z \to ee$. The same procedure is followed as the simple model above to derive the per-electron perturbations. But now we perform the analysis in bins of reconstructed electron p_T. Figure 6.13 shows per-electron correction factors for the $W \to e\nu$ events. The correction factor is multiplied to the SET efficiency shown in figure 6.12. We can see electrons with high $p_T(> 60\text{ GeV})$ need a correction factor greater than 1 for the reason mentioned above.

6.8 Final Efficiency Check

So far as we discussed, the geometric dependencies are measured using the tag-and-probe method on the $Z \rightarrow ee$ data. For the $p_T(e)$ related dependence, different full MC samples have been largely used. For example, the correlations between the electron p_T, the electron physics η and the event SET are studied and modeled in detail in the fast simulation. Due to the truth method we are using for the full MC and the limited statistics in the data, the corresponding procedure and binning in $\eta/p_T(e)$ can not be repeated in the data. Since the fast simulation has been tuned to describe the detailed MC well, the best thing to do is to check if there is any difference between the data and full MC when it comes to the $p_T(e)$ dependence of the selection efficiency. In case there is any difference, we can correct the efficiency measured in full MC by the ratio between the data and full MC. We perform the tag-and-probe method in both the data and full MC to measure the p_T dependence. Figure 6.14 shows the pT dependence of the HMx efficiency for CC electrons in the data and full MC(left) and their ratio(right). It clearly demonstrates that the data and full MC have the same p_T dependence to within the errors from limited data statistics, and we can simply fit their ratio by a flat line with a good χ^2/dof. We observe a similar behavior for the track match, as shown in figure 6.15. Given these results, we can now securely rely on the p_T dependence measured from full MC for the data measurement.

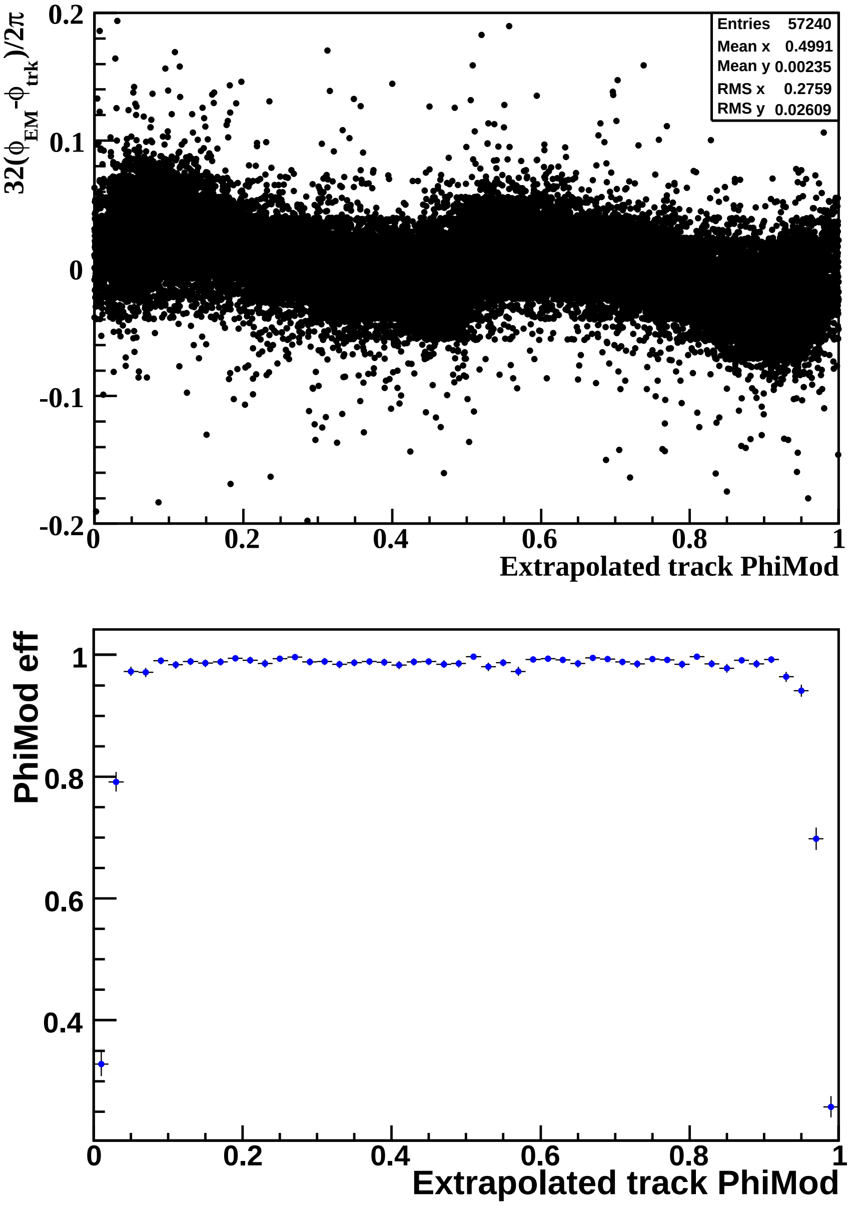

Figure 6.1: Top: Difference between ϕ_{EM} and ϕ_{trk} (fmod$(32(\phi_{EM} - \phi_{trk})/2\pi, 1.0)$) in module units vs track phimod (fmod$(32\phi_{trk}/2\pi, 1.0)$). Bottom: PhiMod efficiency as a function of the extrapolated track PhiMod.

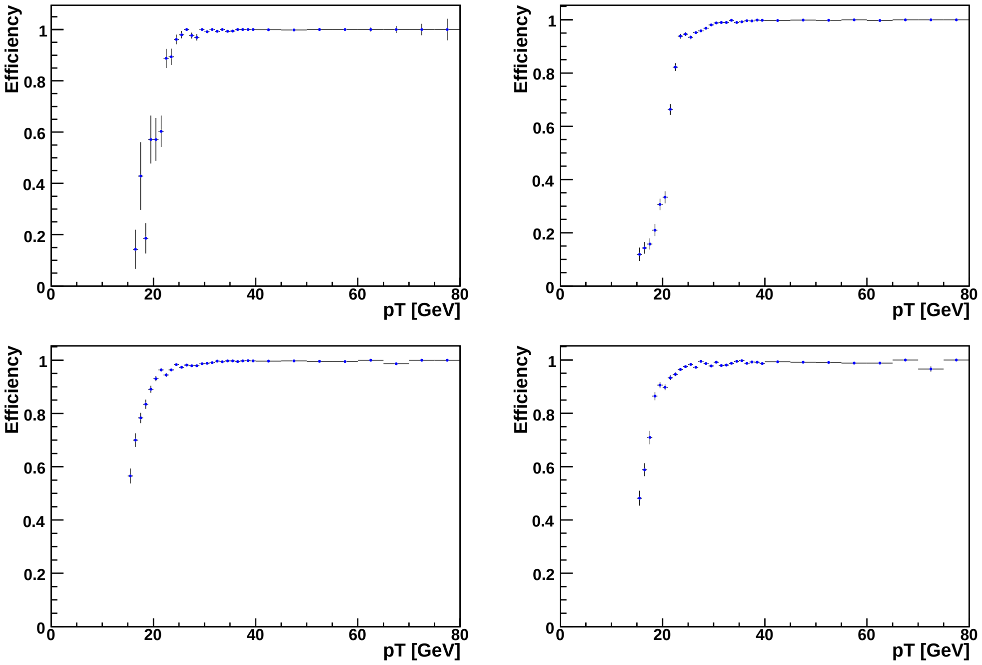

Figure 6.2: Trigger efficiency vs electron p_T for four different trigger periods. Top left: v8-11, top right: v12, bottom left: v13 and bottom right: v14.

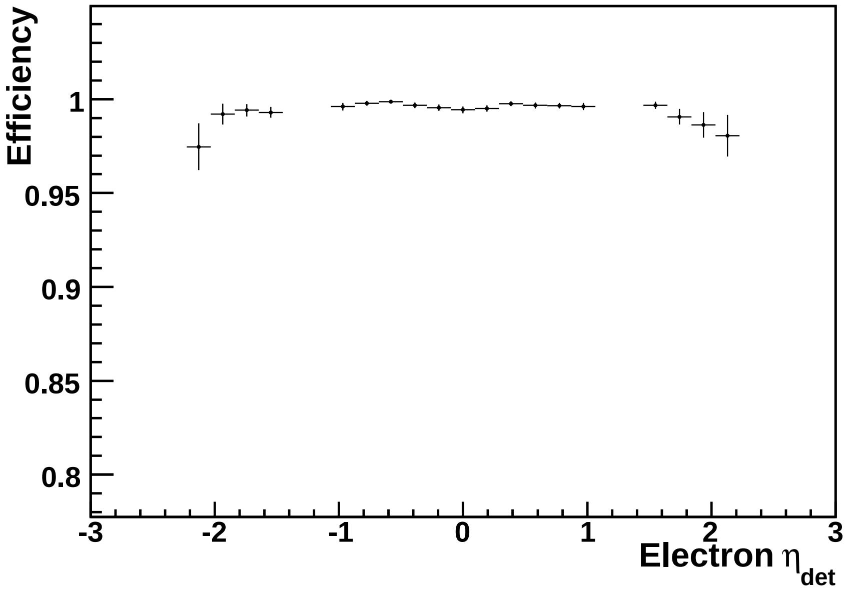

Figure 6.3: The efficiency for reconstructing a loose EM cluster. The efficiency is almost flat over the η region used here ($|\eta_{det}| < 1.05$).

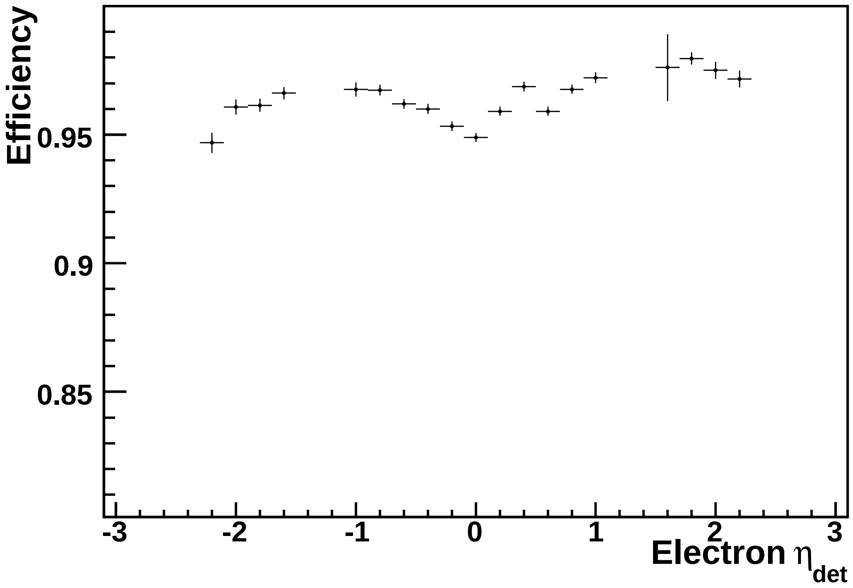

Figure 6.4: The η_{det} dependence of the final HMx requirements relative to the preselection.

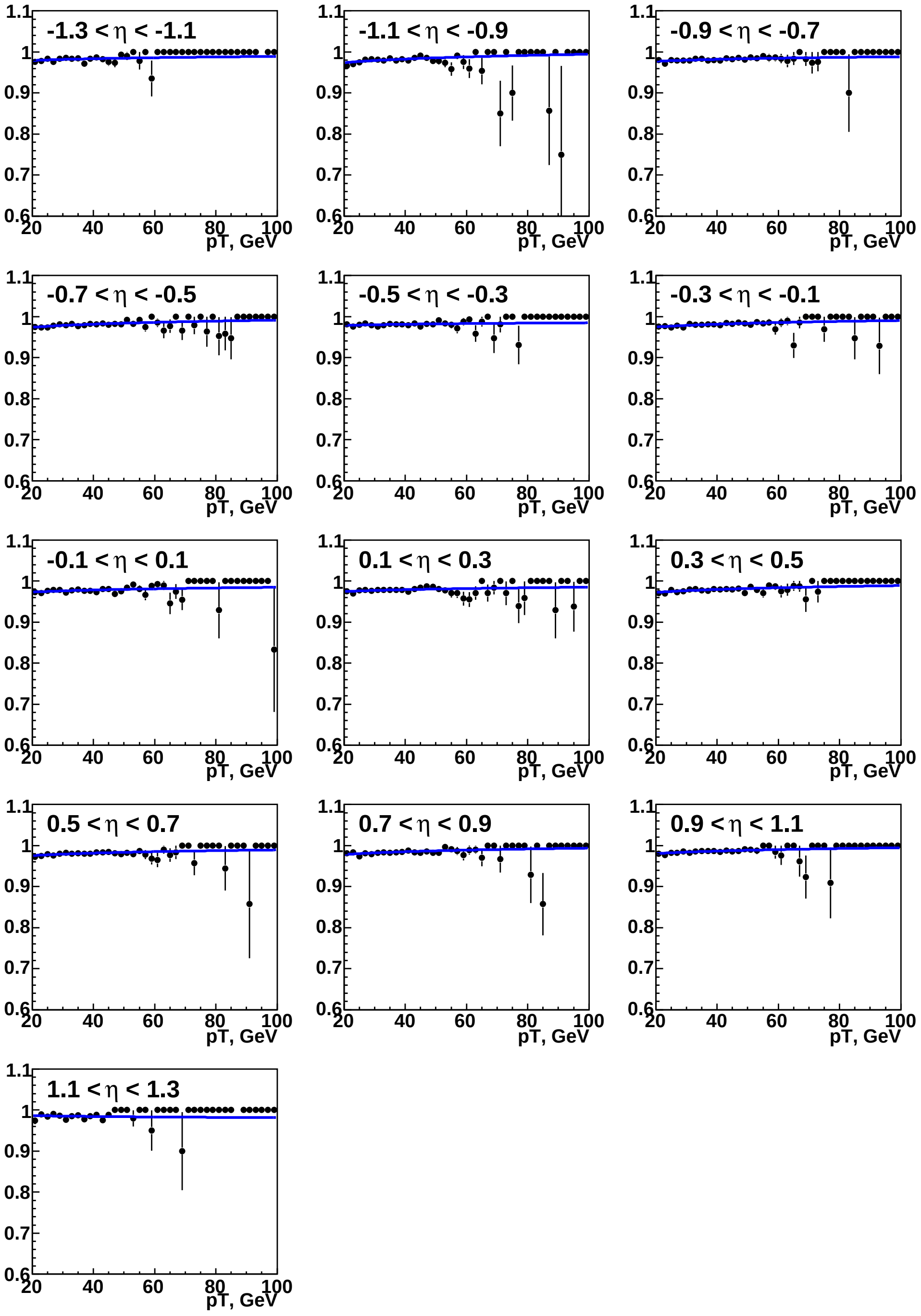

Figure 6.5: The η and p_T dependence of the HMx efficiency for single electrons relative to the preselection efficiency. Each pane shows the p_T efficiency in a given η bin. The bins are 0.2 units wide in η and cover the range $-1.3 \leq \eta \leq 1.3$, and the horizontal axes run from 20 GeV to 100 GeV.

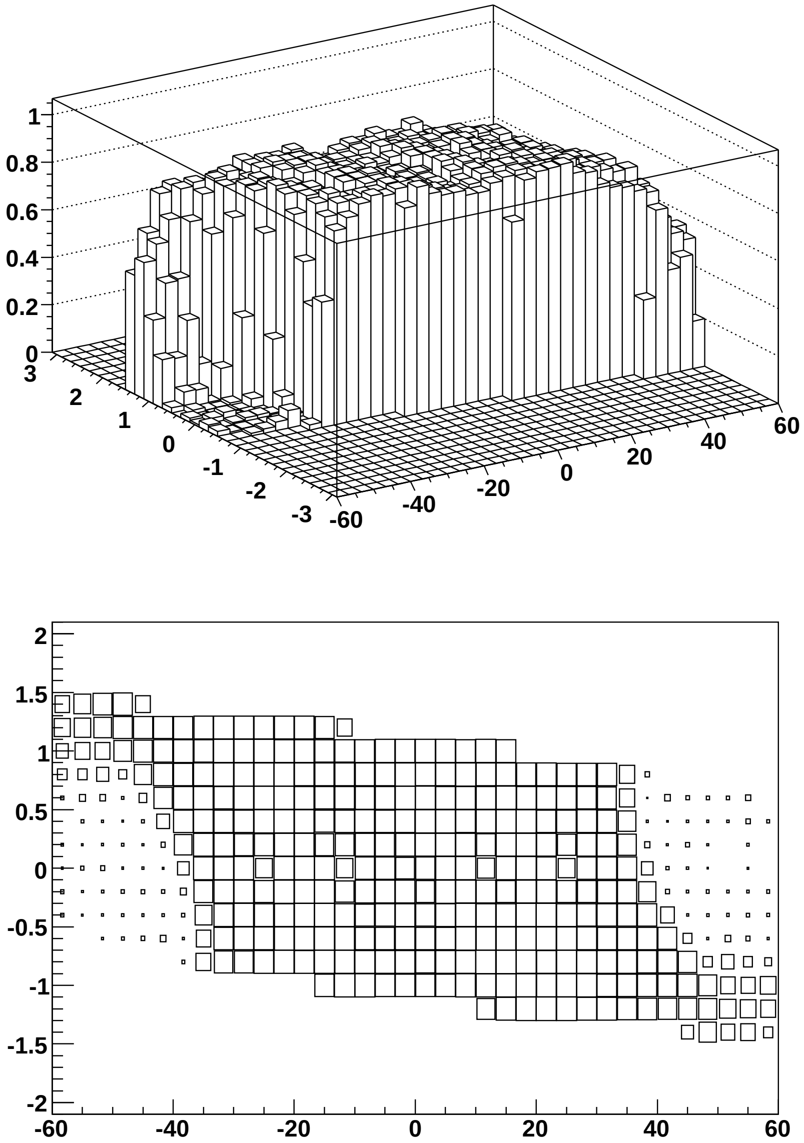

Figure 6.6: The tracking efficiency as a function of η_{phys} and vertex z position shown as a lego plot(top) and as a box plot(bottom).

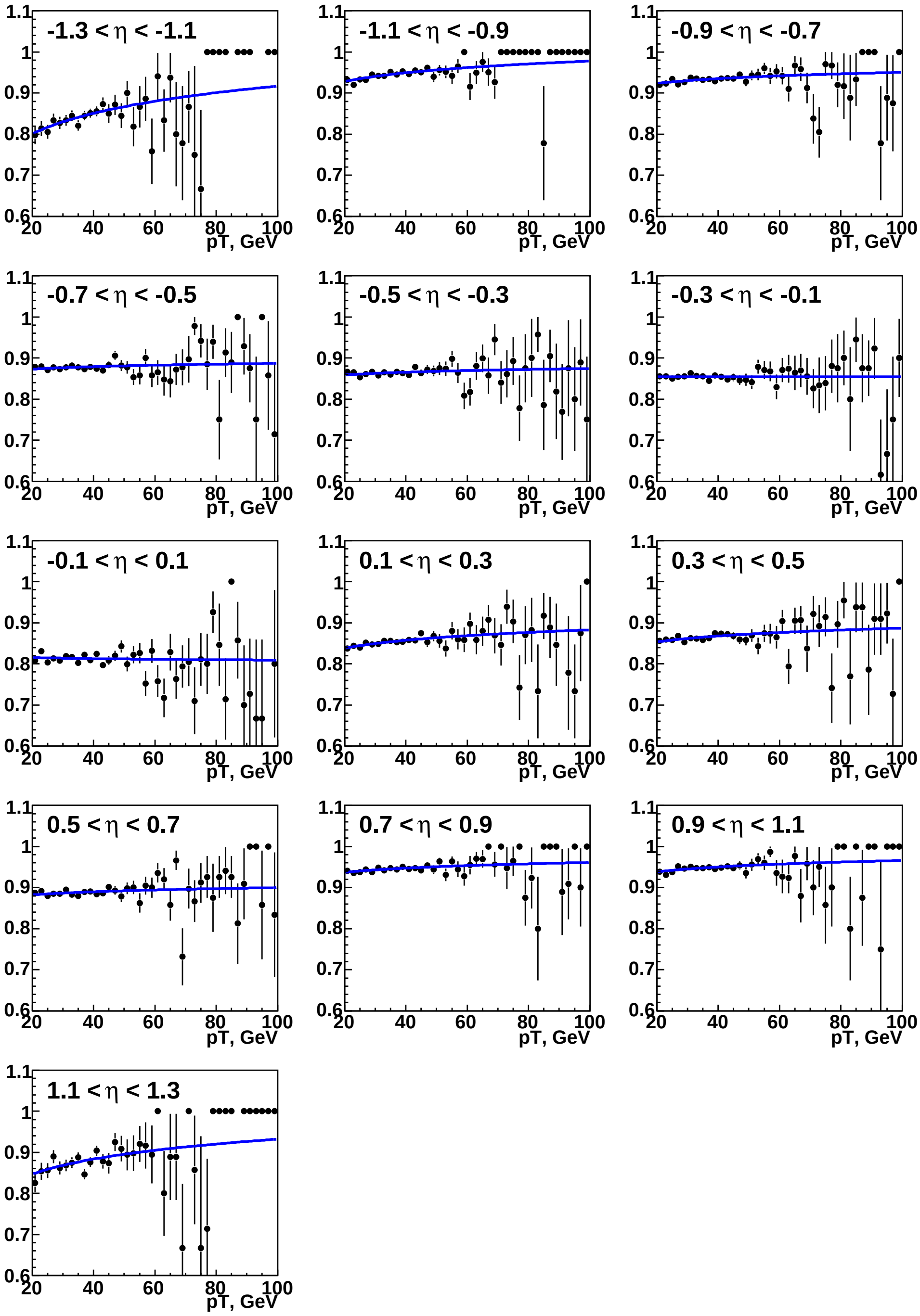

Figure 6.7: The tracking efficiency as a function of η and p_T determined using single electron events. Each panel shows the p_T efficiency in a given η bin. The η bins are 0.2 η-units wide and cover the range $-1.3 \leq \eta \leq 1.3$, and the horizontal axis in each figure runs from 20 GeV to 100 GeV.

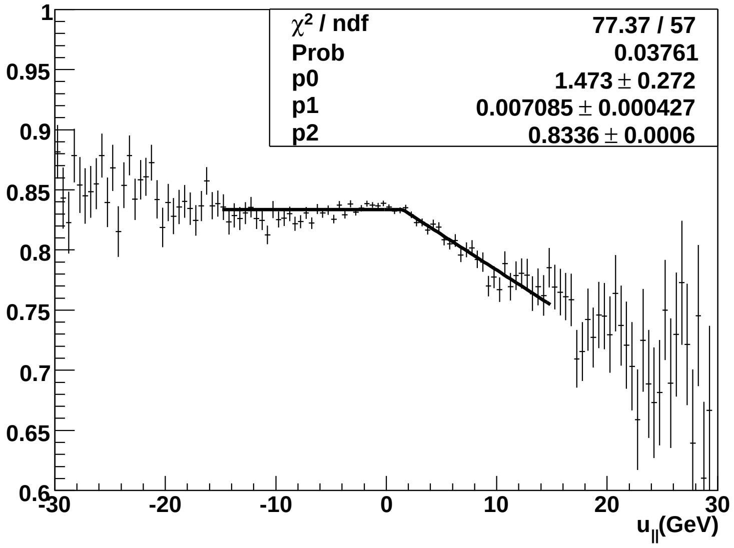

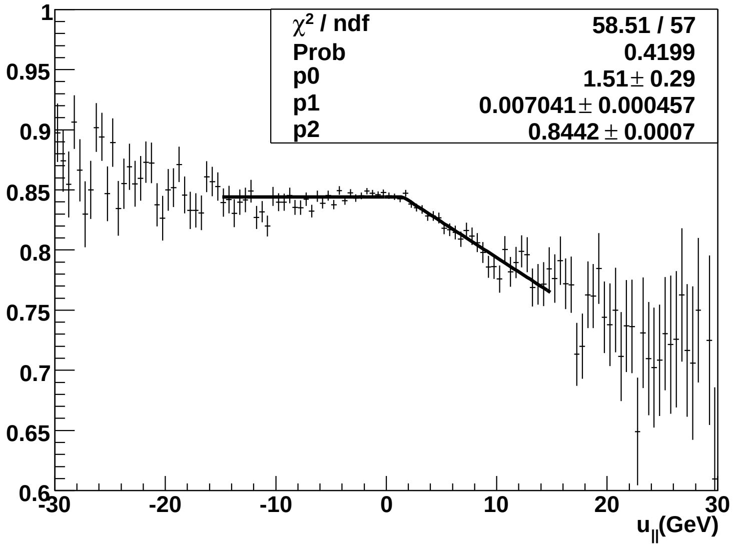

Figure 6.8: $u_{\parallel}$ efficiency in full MC $Z \rightarrow ee$: Top: Truth method; Bottom: tag-probe method

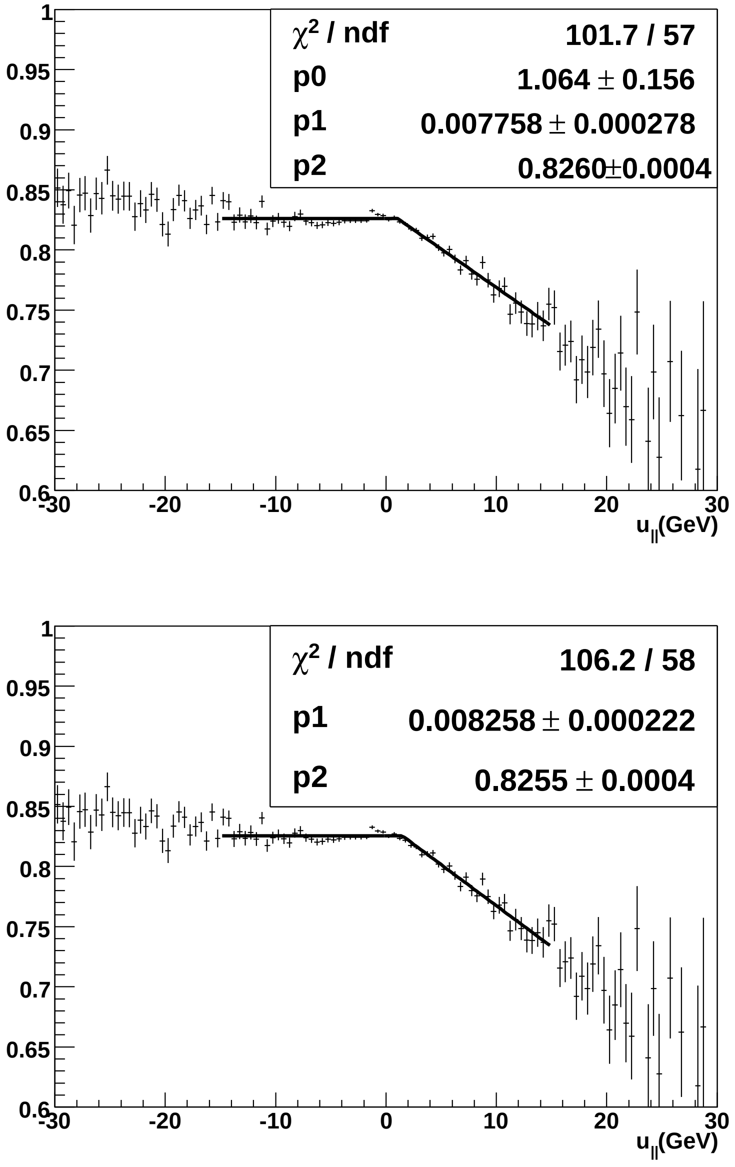

Figure 6.9: $u_{\parallel}$ efficiency in full MC $W \rightarrow e\nu$ using truth method: Top: allow p0 to float; Bottom: fix p0 the same as for Z

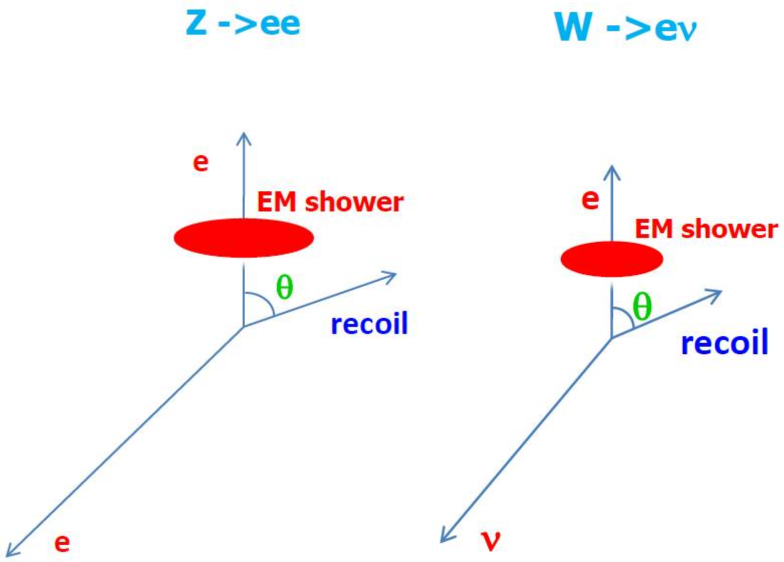

Figure 6.10: Left:$Z \rightarrow ee$; Right:$W \rightarrow e\nu$

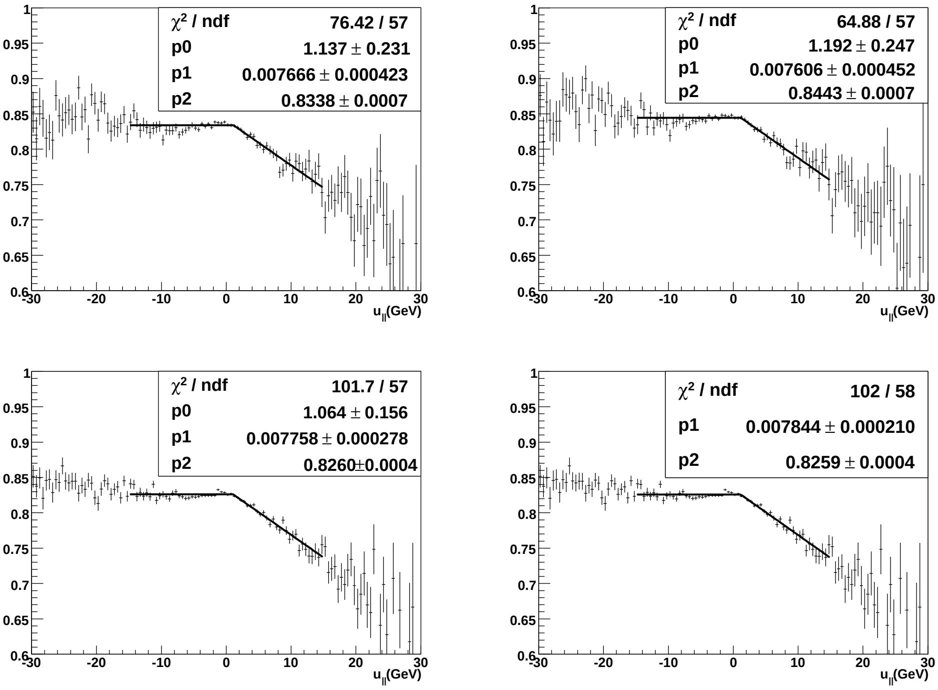

Figure 6.11: $u_{\parallel}$ efficiency in full MC $Z \rightarrow ee$ after scaled to W
Top: Left, Truth method in Z; Right, tag-probe method
Bottom: Left, Truth method in W; Right, Truth method in W by fixing p_0 at the value from Z

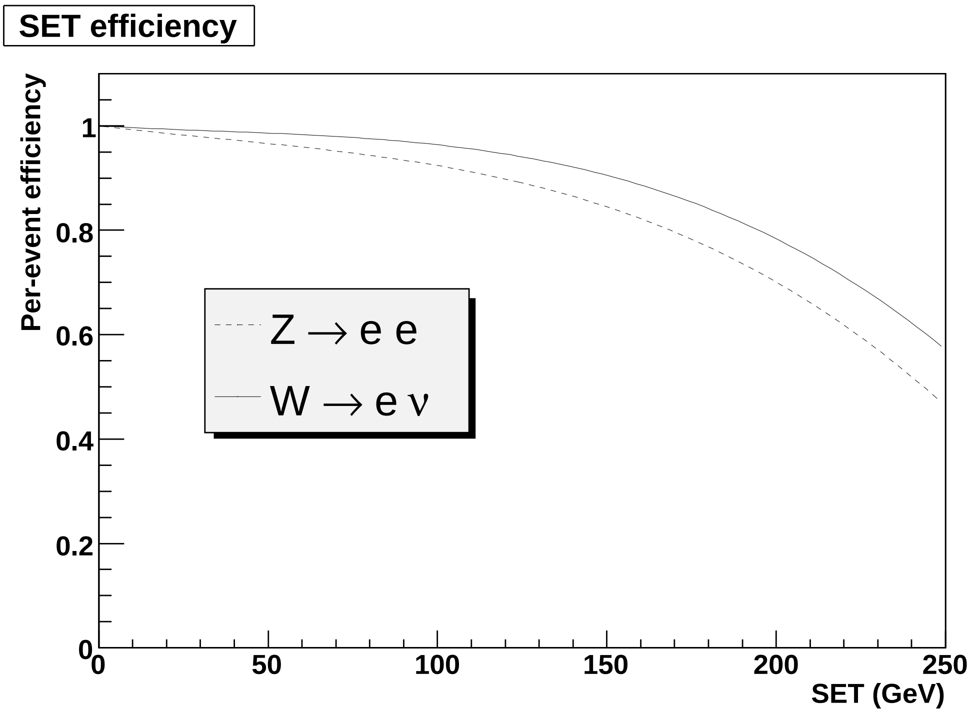

Figure 6.12: The event reconstruction efficiency as a function of SET shown separately for Z and W full MC events. The polynomial fits are used in the fast simulation.

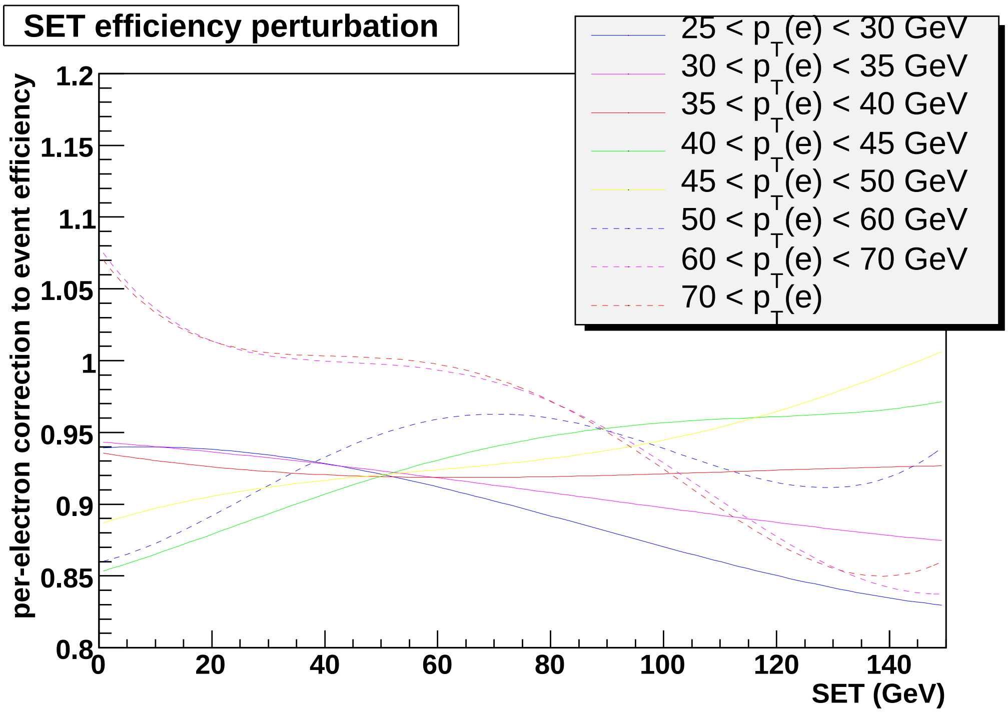

Figure 6.13: The electron p_T and SET based correction factors to the SET parameterization of event efficiency. Each curve corresponds to a different p_T range, and the horizontal axis is the SET.

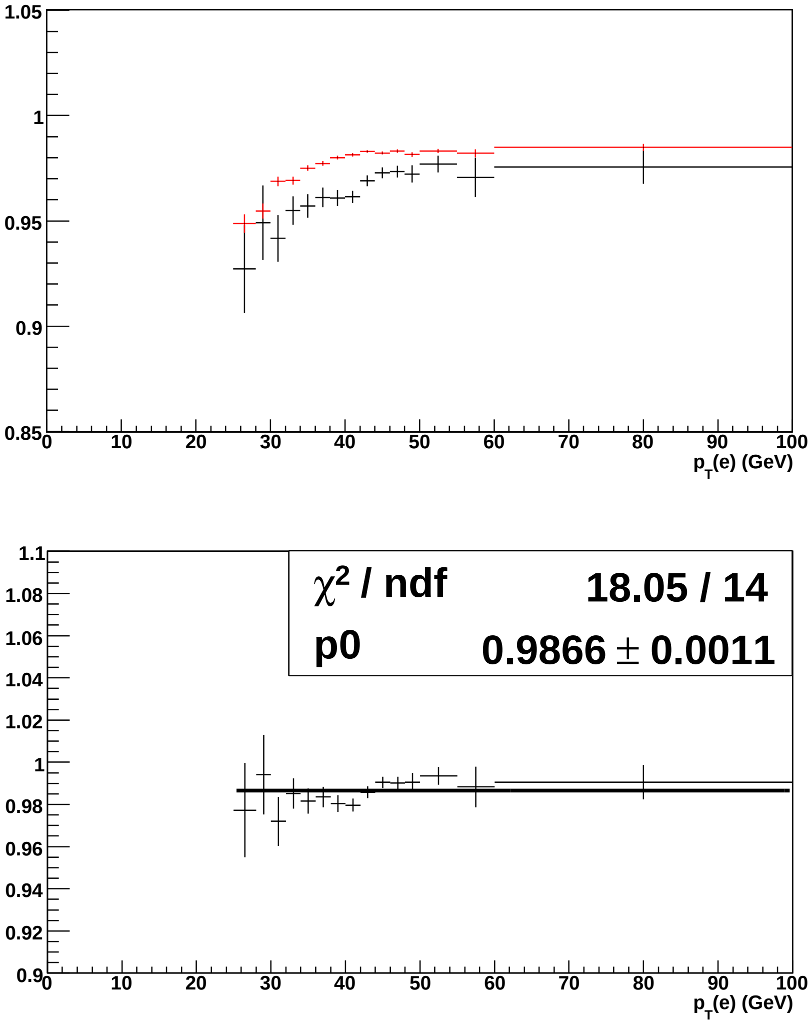

Figure 6.14: Top: $p_T(e)$ dependence of HMx for CC electrons in data(black) and full MC(red); Bottom: Ratio between the black and red curve in the left plot.

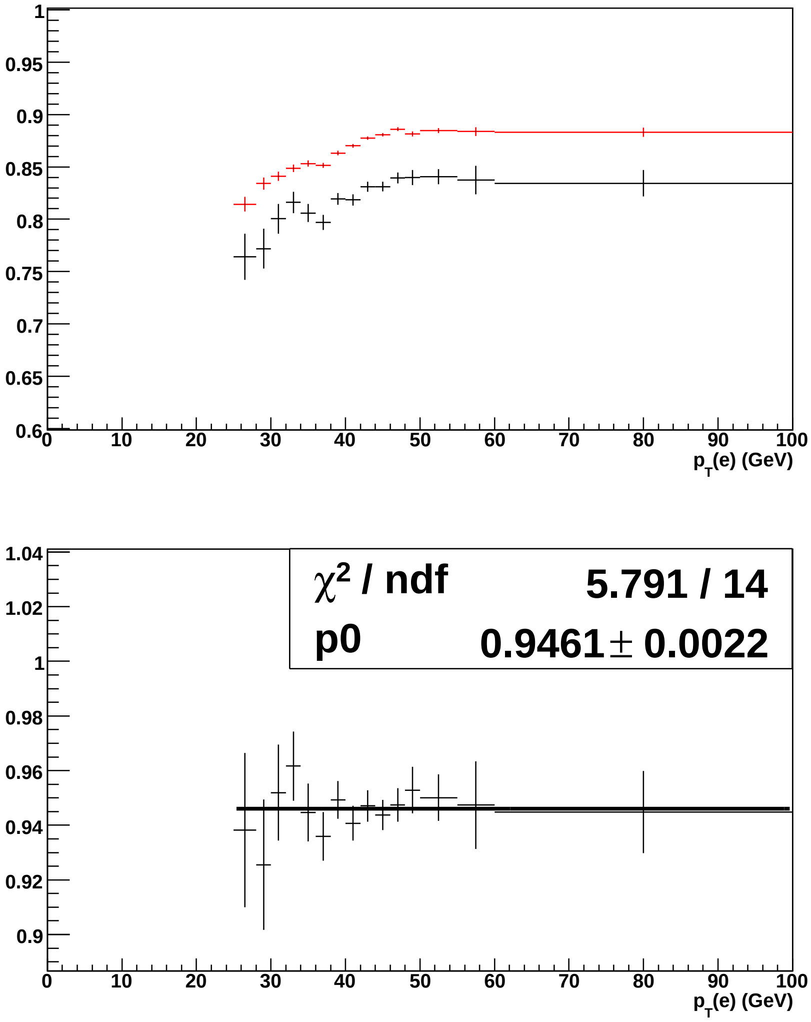

Figure 6.15: Top: $p_T(e)$ dependence of Track match for CC electrons in data(black) and full MC(red); Bottom: Ratio between the black and red curve in the left plot.

Chapter 7

Electron Response

After plugging the efficiencies in the fast MC, the next step would naturally be to model the electron energy response and resolution. In addition to the intrinsic detector response to the electron energy, there are also contributions from other sources, for example, photon radiation, the hadronic recoil system and zero-suppression, etc.

7.1 Photon Radiation

Photons radiated off the electrons in $W \rightarrow e\nu$ decays could carry substantial energy. If a radiated photon is distant enough from the electron, the photon energy will not be calculated as part of the electron energy, thus will lower the measured electron energy and W boson mass. An electron can radiate photons at the generation (internal bremsstrahlung) or during the interaction with material (external bremsstrahlung). The external photon effect is corrected for by the electron energy loss correction.

Since the photon radiation effect on the measurement of electron energy strongly depends on the distance between the photon and the electron, we parameterize both the electron efficiency and the electron energy versus the distance between the photon and the detected electron.

$$\Delta R = \sqrt{[\phi(e) - \phi(\gamma)]^2 + [\eta(e) - \eta(\gamma)]^2}$$

Two full MC samples are used to study the electron and photon responses: one with single electrons(from $W \rightarrow e\nu$) without FSR(final state radiation) and the other with exactly the same events, but some of which could have FSR. Figure 7.1 shows the electron reconstruction efficiency versus the fraction of the energy carried by the leading photon (X). The events are binned in 12

ΔR bins, with the first bin (top left) corresponding to $0.0 < \Delta R < 0.05$ and the last bin (bottom right) corresponding to $0.55 < \Delta R < 0.6$.

In these plots, we can see the efficiency is influenced by the combination of the isolation, HMx and track match requirements, which are dominating in different situations. The first few plots show similar dependence because they are mainly affected by the track match requirement while the electron isolation and shower shape are not that biased when the photon is still very close to the electron. The bump in the next few plots is a little complicated. In these cases, the photon starts to be not too close to and also not too far from the electron. When the photon energy grows, the photon might be reconstructed as the electron, therefore the efficiency could increase. That is how we see a bump in these plots. In the last few plots, the photon is distant from the electron and has no direct impact on the electron reconstruction unless its energy is very large.

Aside from the effect on the electron efficiency, the photon radiation also impacts the electron energy response. The radiated photon will take away some of the electron energy. If the photon is close to the electron, it will also bias the electron shower shape and change the reconstructed electron energy. Figure 7.2 shows the average electron energy response difference between no FSR and FSR. The same 12 ΔR bins are used here. The horizontal axis is still the fraction of energy carried by the leading photon (X). The vertical axis is defined as the difference between the reconstructed electron energy with and without FSR divided by the true energy without FSR and divided by the fraction of energy carried out by the leading photon.

$$\kappa = \frac{(E_{reco}[\mathrm{withFSR}] - E_{reco}[\mathrm{noFSR}])/(E_{true}[\mathrm{noFSR}])}{X}$$

In plots with high ΔR, it is easy to understand that $\kappa = -1$ because the photon is far away from the electron and just gets lost. The efficiency and energy response shown in figure 7.1 and 7.2 are modeled in the fast MC.

7.2 $\Delta u_{||}$ Correction

The electron is reconstructed with a cone size 0.2. However, the energy deposited in this cone is not completely from the electron. The hadronic recoil system generally spreads over a large range in the detector. Some of the recoil particles could go into the electron cones and contribute their energies. This contribution is called $\Delta u_{||}$.

To estimate the contribution from the recoil system, we use $W \rightarrow e\nu$ events that pass the standard W selection. Each electron energy is calculated by summing the energy deposited in an electron window. We rotate the electron reconstruction window azimuthally away from the electron cluster, just outside the isolation region($0.4 < \Delta\phi < 0.6$), which is still close to the electron. Therefore we have a control region which has a minimal bias in estimating the energy contribution to the electron from other sources. To avoid the region where there are some jet activities from to the W/Z recoil, we require the ratio between the energy for the rotated position and the raw electron energy should be less than 0.15. Fig. 7.3 shows the transverse energy per region, $\Delta u_{||}$. The average is 120 MeV, giving slightly less than 10 MeV per tower [56].

As the luminosity increases, the number of additional interactions per event also increases and contributes more energy into the electron window. When the $u_{||}$ is larger, which means the recoil is closer to the electron, more recoil energy will go into the electron cluster. So we need to measure the $\Delta u_{||}$ dependence on the luminosity and $u_{||}$. Figure 7.3 shows the $\Delta u_{||}$ parametrization on the luminosity and $u_{||}$, which will be implemented in the fast MC.

7.3 Energy Response: EM Scale and Offset

After all the corrections have been done to the data, we need to study the electron energy response that could be parameterized in the fast MC. In the fast MC, the measured electron energy is related to the true electron energy by

$$E_{meas} = \alpha \times E_{true} + \beta, \tag{7.1}$$

where α is the scale and β is the offset[57]. The reason we do not have a non-linear term in the equation is because the non-linear term is mainly caused by the dead material which has already been dealt with by the energy loss correction. We used Z decay events that pass the standard EM requirements and both electrons need to have a matching track, which reduces the background contamination to a negligible level.

When the offset β satisfies $\beta \ll E(e_1) + E(e_2)$, the observed Z mass can be expressed as

$$M_{obs.}(Z) = \alpha M_{true}(Z) + \beta f_Z^{obs} + \mathcal{O}(\beta^2), \tag{7.2}$$

where f_Z^{true} is a kinematic variable defined as:

$$f_Z^{obs} = \frac{E_{obs}(e_1) + E_{obs}(e_2)}{M_{obs}(Z)}(1 - \cos\theta), \tag{7.3}$$

where $E_{true}(e_1)$ and $E_{true}(e_2)$ are the true energies of the two electrons, $M_{true}(Z)$

is the true Z mass, $M_{obs.}(Z)$ is the observed Z mass, and θ is the opening angle between the electrons. f_Z characterizes the energy spread of the two electrons from the Z decay. The scale and offset cannot be distinguished to the precision required using only the M_Z distribution. So the fact that the two electrons from Z decays are not monochromatic is used as an additional constraint. The fast MC is used to make templates of $M_{obs.}(Z)$ vs f_Z^{obs} for different combinations of α and β values. Figure 7.5 and 7.6 show the $M_{obs.}(Z)$ vs f_Z^{obs} distribution in the full MC and the data respectively. The templates are compared with the same $M_{obs.}(Z)$ vs f_Z^{obs} plot obtained from the data to extract the best α and β value. Figures 7.7 shows the measured result of α and β, which is highly anti-correlated. The fitted values are

$$\begin{aligned} \alpha &= 1.0111 \pm 0.0043 \\ \beta &= -0.40 \pm 0.21 \text{ GeV}, \end{aligned}$$

with the correlation -0.997.

We propagate the α and β errors along with the anti-correlation into the W mass uncertainty. The estimated $M(W)$ uncertainty due to electron energy scale and offset is found to be 34.0±0.9, 33.5±0.5, and 33.6±0.7 MeV from $M_T(W)$, $p_T(e)$, and $pT(\nu)$ measurements respectively. It is the dominant uncertainty in this W mass measurement and primarily limited by the number of $Z \to ee$ events, which are used to do the calibration.

7.4 Energy Resolution: Constat, Sampling and Noise Terms

For an electromagnetic calorimeter, the energy resolution of can be approximately written as

$$\frac{\sigma_{EM}(E)}{E} = \sqrt{C_{EM}^2 + \frac{S_{EM}^2}{E} + \frac{N_{EM}^2}{E^2}} \tag{7.4}$$

with C, S and N as the constant, sampling and noise terms respectively. [58]The constant term accounts for the non-uniformity of the calorimeter response. It has a constant effect on the fractional resolution, independent of the energy, and therefore is the dominant effect at high energies. The sampling term is due to the fluctuations related to the physical development of the shower, especially in sampling calorimeters where the energy deposited in the active medium fluctuates event by event because the active layers are interleaved with absorber layers. The noise term comes from the electronic noise of the readout system, radioactivity from the Uranium, and underlying events. Since the noise contribution is proportional to 1/E and the analysis is dealing with high energy electrons, it is basically negligible.

Due to the large amount of material in front of the calorimeter, S_{EM} is no longer a constant and need to be parameterized as

$$S_{EM} = (S_1 + \frac{S_2}{\sqrt{E}}) \times \frac{e^{S_{exp}/\sin\theta}}{e^{S_{exp}}}$$

where

$$S_{exp} = S_3 - S_4/E - S_5^2/E^2$$

This formula and the constants $S_i,\ i = 1, ..., 5$ were derived using the full MC with the missing dead material added in(chapter 4). The noise term was found to be 0.29 GeV, whose contribution, for the reason mentioned above, is negligible. The constant term is derived by a fit to the width of the Z boson mass distribution in the data with the sampling term fixed to the value determined above. Z mass templates are made by using the fast MC for different values of the constant term and compared with the Z mass distribution in the data to extract the best value of the constant term [59]. The measured constant term is found to be

$$C_{EM} \quad = \quad (2.04 \pm 0.13)\%$$

7.5 Quality of the Electron Energy Loss Corrections

In chapter 4, we introduced the energy loss correction functions parameterized as a function of energy and η_{phys}, which are derived from the full MC sample. So the precision of the corrections are limited by the full MC sample. As discussed in the previous section, the final tuning of the electron energy response using $Z \to ee$ events from the data does fix some of imperfections in the E-loss parameterizations, for example, a global scale mistake in the energy loss function.

The electrons from $Z \to ee$ populate one “band” in E/η_{phys} space, and electrons from $W \to e\nu$ populate another band in E/η_{phys} space. The energy scale tuned based on $Z \to ee$ events might have a slightly different effect when applied to $W \to e\nu$ events.

To estimate the effect from the different E/η_{phys} space of $Z \to ee$ and $W \to e\nu$, we did the following study. In the full MC $Z \to ee$ and $W \to e\nu$ events, we calculate the difference between the reconstructed and the true energy and divide it by the true energy as a function of the true electron energy. This fractional energy difference reflects the imperfection of the energy loss corrections. Any difference in the imperfection of $Z \rightarrow ee$ and $W \rightarrow e\nu$ events will be translated into the reconstructed W electron energy and then into the measured W mass. After propagating the imperfection difference into the W mass, we found the effect is negligible. And we put 4 MeV as the systematic uncertainty due to the different E/η_{phys} space of electrons from $Z \rightarrow ee$ and $W \rightarrow e\nu$ for the variables m_T, $p_T(e)$ and $\not{E}_T$. This 4 MeV is limited by the statistics of the full MC events used for this study.

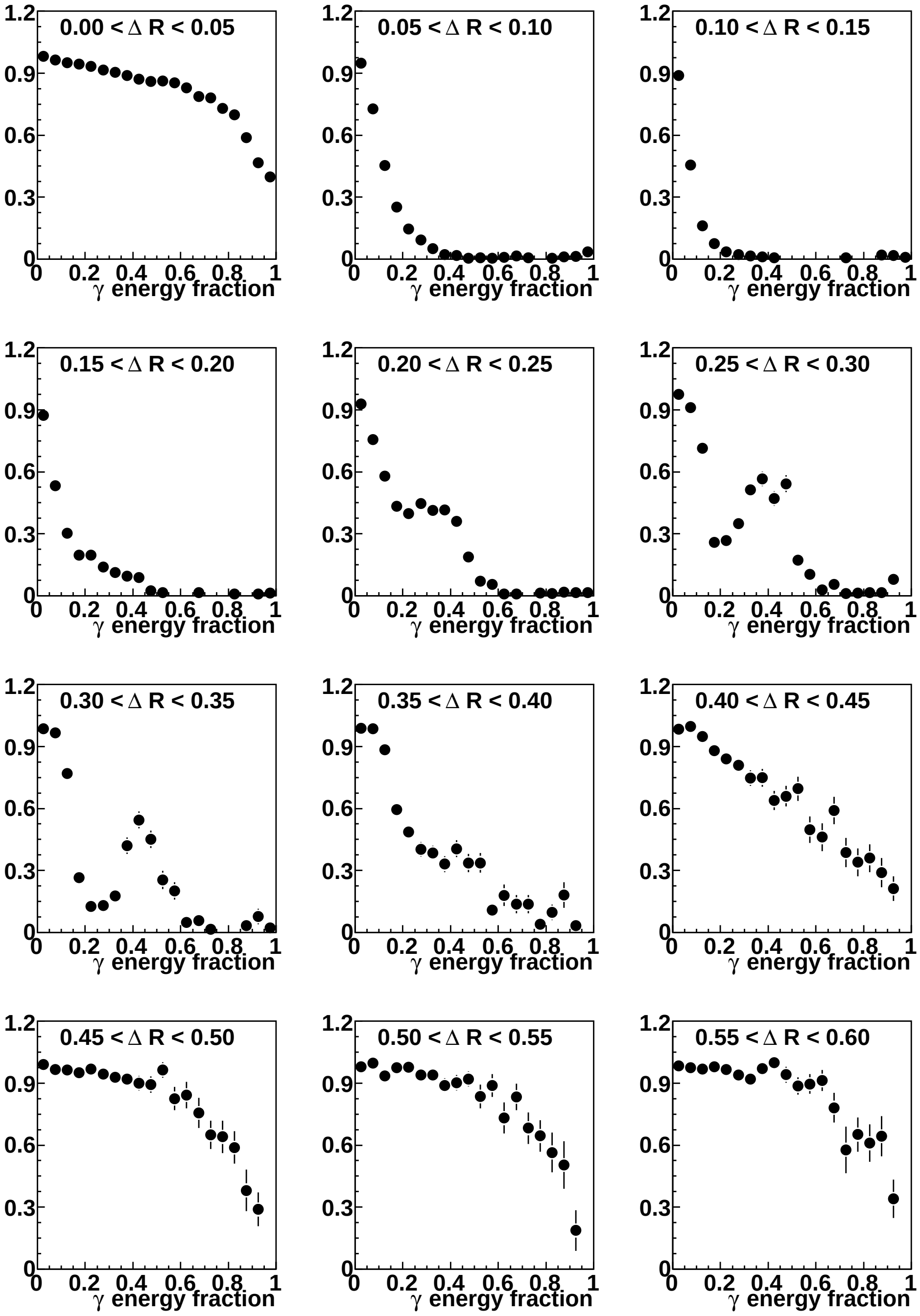

Figure 7.1: Electron identification efficiency as a function of fraction of the energy carried out by the leading photon.

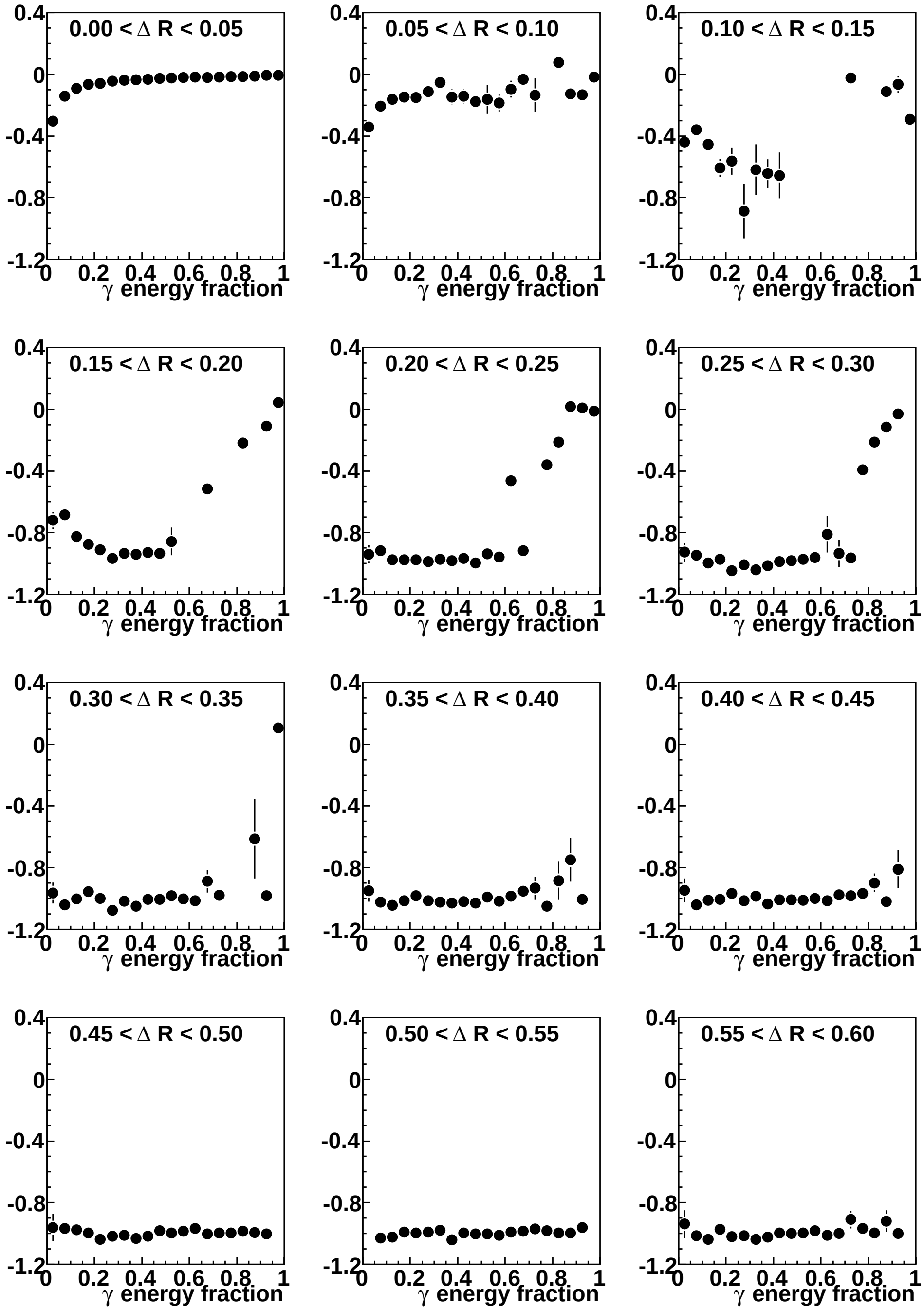

Figure 7.2: Electron energy correction as a function of fraction of the energy carried out by the leading photon.

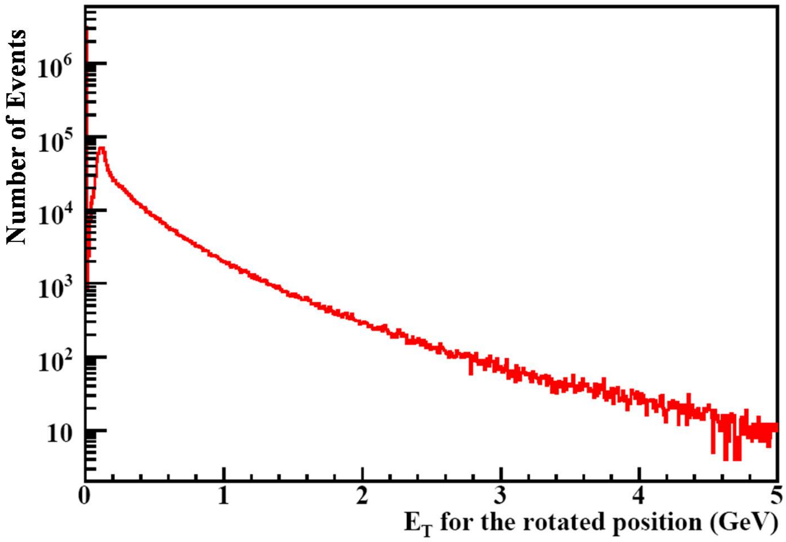

Figure 7.3: $\Delta u_{\parallel}$ distributon in collider data.

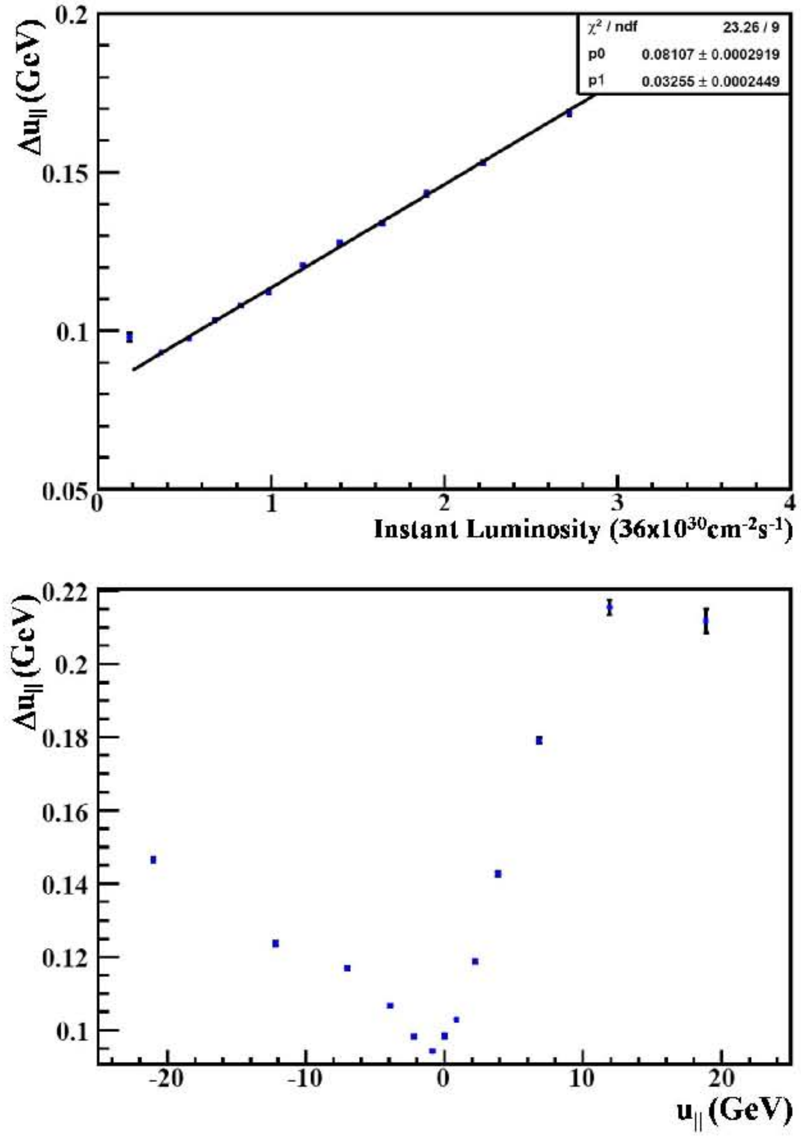

Figure 7.4: Average $\Delta u_{\|}$ as functions of luminosity (top) and $u_{\|}$ (bottom) in collider data.

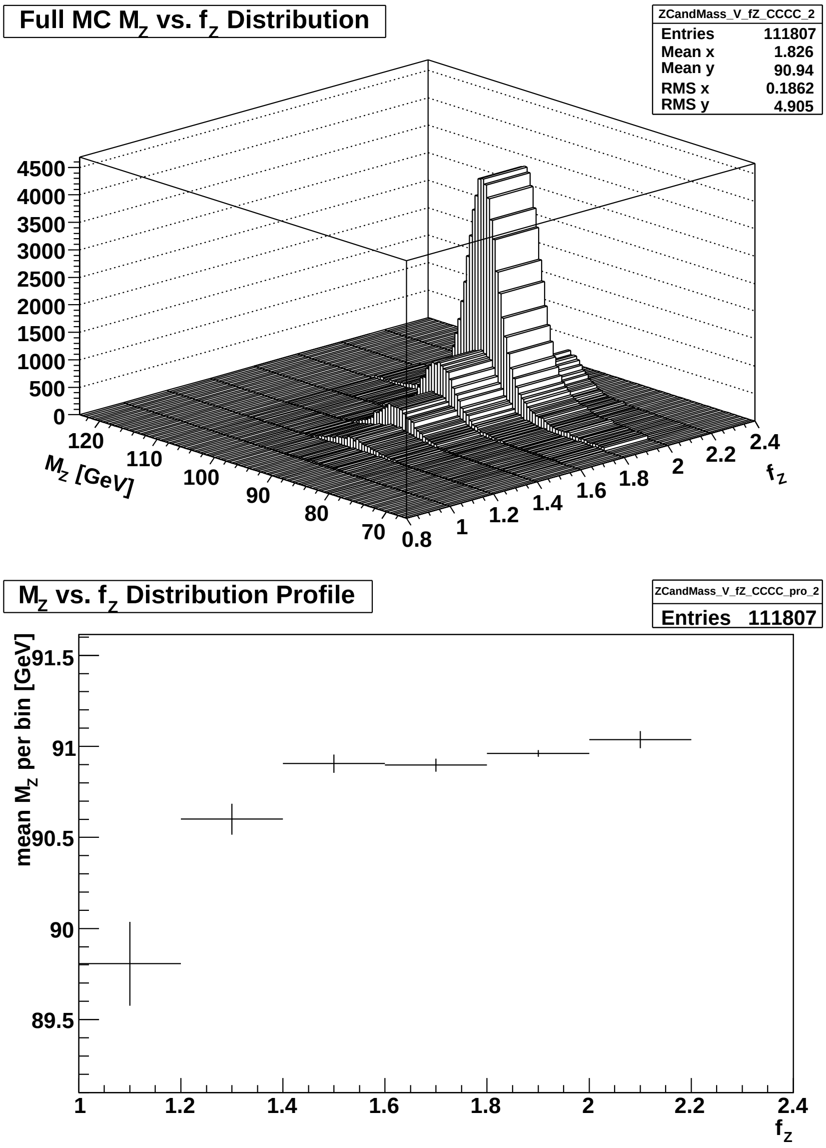

Figure 7.5: Top: An example of the f_Z vs. M_Z distribution(full MC); Bottom: The profile histogram of the 2D distribution(full MC).

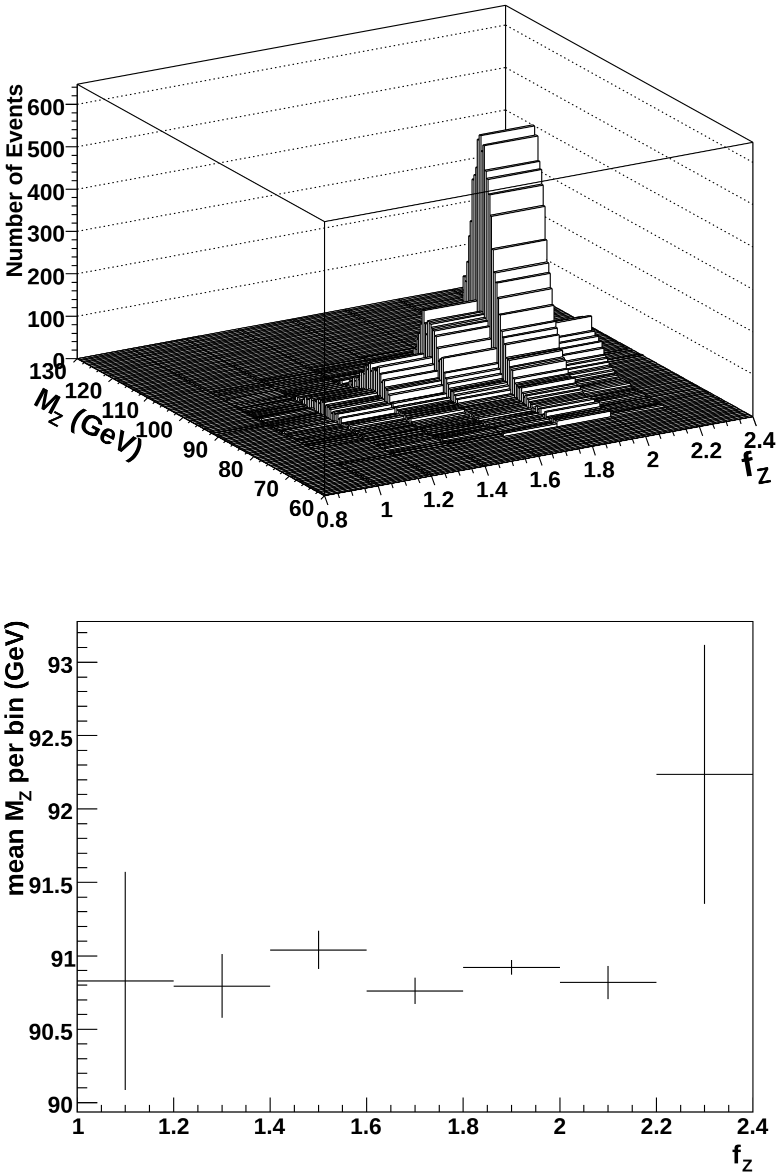

Figure 7.6: Top: An example of the f_Z vs. M_Z distribution(data); Bottom: The profile histogram of the 2D distribution(data).

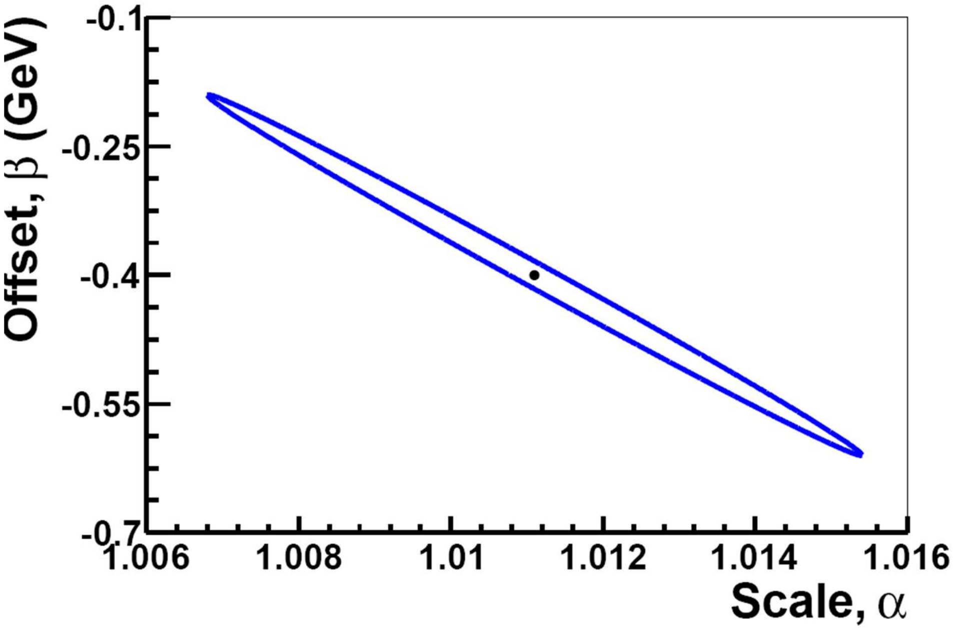

Figure 7.7: The central value for α and β as determined from the fit to the Z mass distribution and the error ellipse defined by $\Delta\chi^2 = 1$.

Chapter 8

Hadronic Recoil

The hadronic recoil system is defined as everything else except the electron(s) in each W or Z event. Correct understanding and modeling of the hadronic recoil is crucial because the recoil basically affects almost every aspect of the W mass measurement: $\not{E}_T$ is calculated by balancing $p_T(e)$ and the recoil p_T; the recoil contributes to the energy in the electron window by $\Delta u_{||}$ correction; the existence of the recoil also affects the electron reconstruction and selection efficiency; since we make a cut on the recoil p_T, it further affect the boson p_T and the electron p_T. Figure 8.1 is an illustrative picture of a $W \rightarrow e\nu$ event in the transverse plane.

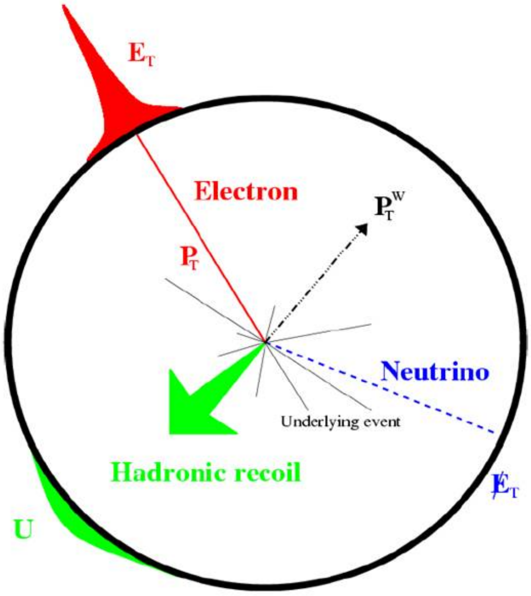

Figure 8.1: $W \rightarrow e\nu$ event in the transverse plane

8.1 Concept of the Hadronic Recoil

The recoil p_T in a $W(Z)$ boson event mainly results from quark or gluon radiation in the initial state. A quark or gluon typically fragments into multiple hadrons and deposit their energies in the calorimeter. There are also contributions coming from other sources such as the underlying events, photon radiation, etc. The W and Z boson have similar boson p_T and recoil p_T distribution. And we can also select very clean $Z \to ee$ sample. So in constructing the model to describe the recoil response and resolution, $Z \to ee$ events in both the full MC and data are largely used.

To simulate the hadronic recoil system in the fast MC, we separate the recoil into four parts based on the source[60][31].

$$\boldsymbol{u}_T = \boldsymbol{u}_T^{\text{HARD}} + \boldsymbol{u}_T^{\text{SOFT}} + \boldsymbol{u}_T^{\text{ELEC}} + \boldsymbol{u}_T^{\text{FSR}} \tag{8.1}$$

- $\boldsymbol{u}_T^{\text{HARD}} = \boldsymbol{f}(\boldsymbol{q}_T)$
  Here $\boldsymbol{u}_T^{\text{HARD}}$ denotes the recoil component coming from the initial gluon radiation and hadronization, associated with the hard scattering of the $q\bar{q}$ pair that generates the $W(Z)$ boson. This "hard" component balances the transverse momentum of the vector boson. Here $\boldsymbol{q}_T$ is transverse momentum of the boson on the generator level. The $\boldsymbol{f}(\boldsymbol{q}_T)$ is an ansatz function used for smearing the $\boldsymbol{q}_T$. It is derived from $Z \to \nu\nu$ full MC events as described in [60].

- $\boldsymbol{u}_T^{\text{SOFT}} = -\,\alpha_{mb} \cdot \not\!\!\boldsymbol{E}_{\boldsymbol{T}}^{\text{MB}} -\ \alpha_{zb} \cdot \not\!\!\boldsymbol{E}_{\boldsymbol{T}}^{\text{ZB}}$
  Here $\boldsymbol{u}_T^{\text{SOFT}}$, named the "soft" component, represents the other interactions that contribute to the hadronic recoil. There are two subcomponents here. The first is the "underlying event" and the second is the "additional energy content in the event". The underlying event consists of the interactions of the spectator partons of the same $p\bar{p}$ pair that produces the vector boson. It is modeled with the help of minimum bias (MB) events. The additional energy content is associated with all the other interactions occuring in the $p\bar{p}$ pairs present in the same or previous beam crossings. Interactions contributing to detector noise are also included in this sub-component. It is modeled using Zero Bias (ZB) events. We set α_{zb} to unity because the ZB events are a reliable control sample directly obtained from collider data, which has the same luminosity profile as events with W and Z.

- $\boldsymbol{u}_T^{\text{ELEC}} = -\sum_e \Delta u_{\parallel} \cdot \hat{p}_T(e)$
  This component serves as a correction for the recoil energy that is parallel to the electron direction. It is present under the electron window, is

measured as part of the electron energy and is thus subtracted from the recoil energy.

- $\boldsymbol{u}_T^{\mathrm{FSR}} = \sum_\gamma \boldsymbol{p}_T(\gamma)$
  The FSR component contains the energy of the Final State Radiation (FSR) photons that are far away from the electron(s) and hence reconstructed as recoil energy.

8.2 Modeling the Hadronic Recoil

8.2.1 Hard Component: $\boldsymbol{u}_T^{\mathrm{HARD}}$

To study the detector response and resolution, the part of the recoil that only comes from the hard scatter, which balances the transverse momentum of the vector boson, we use a special full MC $Z \to \nu\nu$ sample. These special $Z \to \nu\nu$ events are generated using PYTHIA without underlying event, which means there are only hard scatters in these events. The PYTHIA events then go through the full chain of the DØ detector simulation and reconstruction software without adding any Zero-bias overlay to them. Since both neutrinos escape from the detector, what is left is the hadronic recoil system. This full MC sample contains 600,000 $Z \to \nu\nu$ events. In order to obtain kinematics similar to the $Z \to ee$ events used in the final tuning procedure that will be discussed later in this chapter, both the neutrinos from a Z boson decay are required to be centrally located (i.e. physics pseudorapidity $|\eta_\nu| < 1.3$).
The two main variables used to parameterize the hard component are the recoil p_T resolution (R) and the angular resolution ($\Delta\phi$).

$$R = \frac{u_T - q_T}{q_T} \qquad (R < 1) \tag{8.2}$$

$$\Delta\phi = \phi(\boldsymbol{u}_T) - \phi(\boldsymbol{q}_T) \qquad (|\Delta\phi| < \pi) \tag{8.3}$$

Here $\boldsymbol{q}_T$ (= - $\boldsymbol{p}_T^Z$) is the true recoil vector and q_T its magnitude. $\boldsymbol{u}_T$ is the smeared recoil vector and u_T its magnitude.

The parameterization of the hard component of the recoil is described in the following steps. More details have been provided in the recoil note [60].
1) The $Z \to \nu\nu$ sample is split into 32 variably sized bins of q_T from 0 to 100 GeV.
2) For each q_T bin a two-dimensional distribution as a function of R and $\Delta\phi$ is constructed. Two examples of such event *probability density functions (pdf)* are shown in Figure 8.2 and 8.3 as coloured box histograms for $q_T \in [4.5, 5]\, GeV$

and $q_T \in [18,\,20]\,GeV$ bins respectively. From here it is evident that for low values of q_T there is a correlation between R and $\Delta\phi$. Moreover the distributions of R for slices of $\Delta\phi = const$ are non-gaussian.
3)For each q_T bin a fit to the *pdf* observed in the FULL MC sample was preformed using an ansatz parameterisation:

$$pdf(x,y) \;=\; p_0\,\exp\left[-\frac{1}{2}\left(\frac{x-\mu(y)}{\sigma_x(x,y)}\right)^2\right]\,\exp\left[-\frac{1}{2}\left(\frac{y}{\sigma_y(y)}\right)^2\right],$$

where: $x \;\equiv\; R, \quad y \;\equiv\; \Delta\phi\,[rad], \;\; \mu(y) \;=\; p_1 \,+\, p_2\cdot y,$

$$\sigma_x(x,y) \;=\; \begin{cases} p_3, & x < \mu(y) \\ p_4, & x > \mu(y) \end{cases}, \quad \sigma_y(y) \;=\; p_5 \,+\, p_2\cdot y \;\text{ and}$$

$p_0 \,\ldots\, p_5$ are parameters of the fit.

Effectively only 5 parameters are needed to describe the two-dimensional distribution of $\{R,\,\Delta\phi\}$ pairs for a given q_T bin since p_0 is for normalization only. Two such fits are shown in Figures 8.2 and 8.3 as coloured contours for $q_T \in [4.5,\,5]\,GeV$ and $q_T \in [18,\,20]\,GeV$ bins respectively.
4) A smearing function ($\boldsymbol{f}(\boldsymbol{q}_T)$) is built based on these 32 fits. Hence $\boldsymbol{f}(\boldsymbol{q}_T)$ determines the smeared momentum (or $\boldsymbol{u}_T$) of the boson from its generator level momentum (or $\boldsymbol{q}_T$) as the input. The smearing of the hadronic response and resolution (p_T and ϕ) are performed in a single step by $\boldsymbol{f}(\boldsymbol{q}_T)$, inherently including the correlations between them.

8.2.2 Soft Component: $\boldsymbol{u}_T^{\mathrm{SOFT}}$

In the DØ Run I W mass measurement[10], the soft component(underlying event and the additional $p\bar{p}$ interactions) were modeled together by using minimum bias (MB) events adjusted by a factor that scaled the $\not{E}_T$ two-vector of these events. This approach, however, is not sufficient for the RunII scenario due to the much higher instantaneous luminosities and event complexities. In Run II, the underlying event and the interactions of the additional $p\bar{p}$ pairs, on average, have comparable scalar E_T (SET), as shown in figure 8.4. Scalar E_T of an event is defined as the energy flow in the plane transverse to the beams. Specifically in the Run IIa $Z \to e^+e^-$ sample, we find 0.9 vertices in addition to the vertex of the hard scatter, on average. Table 8.1 summarizes the average scalar E_T observed as a function of the number of primary vertices reconstructed in a Z event. To deal with the more additional activity coming from the higher luminosity, we handle the underlying event and the additional $p\bar{p}$ interactions by using two separate models, minimum-bias(MB)

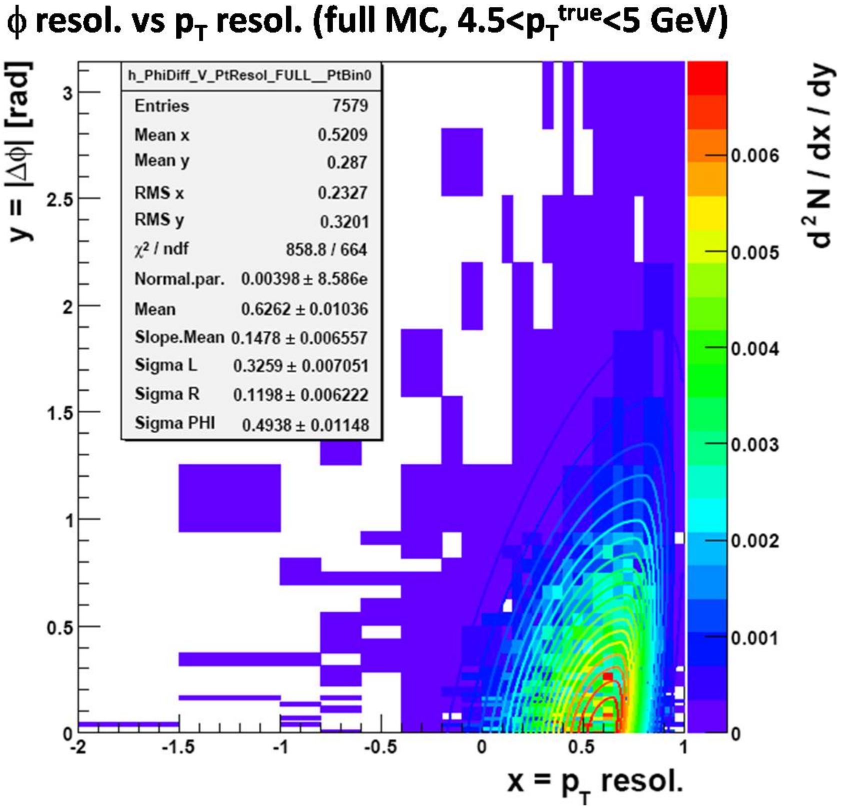

Figure 8.2: The 2-D distribution of the recoil p_T and ϕ resolutions for: full MC (boxes) and fit (contours) for $q_T \in [4.5,\, 5]\, GeV$.

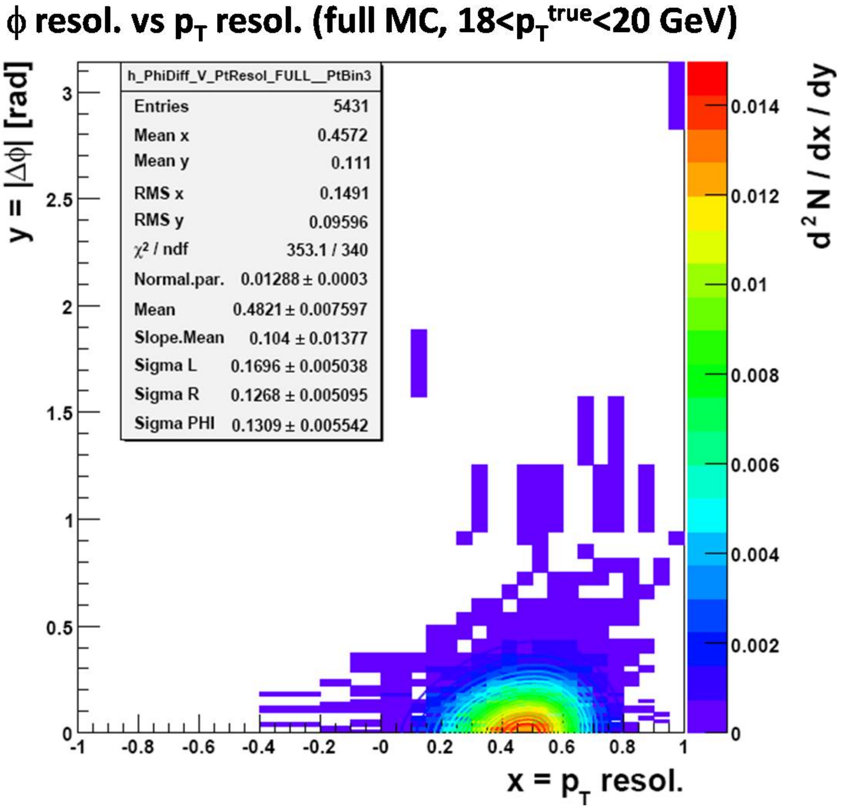

Figure 8.3: 2-D distribution of the recoil p_T and ϕ resolutions for: full MC (boxes) and fit (contours) for $q_T \in [18,\, 20]\, GeV$.

and zero-bias(ZB) events respectively, as the first step in modeling the soft component.

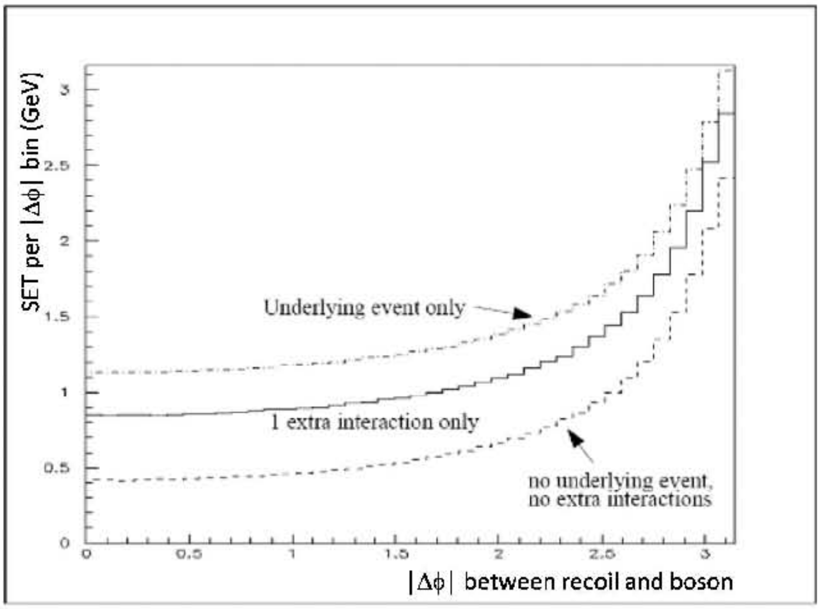

Figure 8.4: Underlying event and additional energy contributions to the Z energy content. The horizontal axis represents the angle $\delta\phi$ between the recoil and the boson. The vertical axis shows the transverse energy flow.

Underlying Event

The underlying event accounts for the interactions between spectator quarks in the same $q\bar{q}$ collision that produced the $W(Z)$ boson, which does not depend on the instantaneous luminosity. To model this part,we use the Minimum Bias(MB) events with only one reconstructed primary vertex. Minimum bias events are chosen by a trigger requiring hits in both luminosity counters which are in time with a beam crossing.

There is no perfect model to describe the underlying event. We need to first reweight the MB events to match the data. The MB events are reweighted to make their scalar E_T (SET) match the scalar E_T of those $Z \rightarrow ee$ events where the electron energy contribution has been removed [60]. The reweighting helps the MB events model the underlying event better. The reweighted MB event information is stored in an event library that is used as a lookup table and the $\not{E}_T$ of the MB events are used for modeling the underlying event. To improve the underlying event model, a multiplicative scale factor called α_{mb} is also used as part of final tuning parameters for the hadronic recoil. α_{mb} is introduced to

Table 8.1: Average SET for different numbers of primary vertices in a Z event

Number of primary vertices (excluding vertex of Z)	Mean SET [GeV] (excluding electron cones)
0	33
1	53
2	74
3	92

remove any possible double-counting(explained in the next page) and account for the difference between the full MC($Z \to \nu\nu$) and the data.

Additional Activity

The additional activity consists of the additional $p\bar{p}$ interactions that occur in the same or previous beam crossings, detector noise and pileup, etc. The "noise" describes all the sorts of noise in the calorimeter (e.g. from electronics, uranium decays, cosmics, beam related backgrounds, etc.). The "pileup" refers to the residual energy in the calorimeter from previous beam crossings. These components are not correlated with the boson p_T and do depend on the instantaneous luminosity.

This part is modeled by using zero-bias(ZB) events. The ZB events were defined by a trigger requiring only synchronization with the beam crossing clock. The instantaneous luminosity profiles and run number sets of the ZB overlay have been recorded in the non zero-suppressed[1] mode and are used in the modeling of the recoil to match those of the $W(Z)$ data taking period.

The fact we are using two event information libraries obtained from the data to model the two sub-components of the "soft" component of the recoil will cause double counting between the MB and ZB events. Both event libraries contain the detector noise and soft interactions which do not possess a primary vertex. As mentioned in the above underlying event section, this double counting effect is eliminated by introducing the multipurpose factor α_{mb} for the MB events and tuning α_{mb} to the $Z \to ee$ data.

---

[1] zero-suppress is a way to suppress energy from the detector noise when recording data. If the signal in one channel is within 1.5 σ around zero after the noise subtraction, the signal will not be read out. Here, σ is the standard deviation of the noise level.

8.2.3 Energy Exchange between Electron and Recoil: $\boldsymbol{u}_T^{\text{ELEC}}$

Since we use a limited cone size to reconstruct the electron energy, some of the electron energy outside the reconstruction cone will be calculated into the recoil energy. This is what is called the "electron energy leakage". On the other hand, as discussed in chapter 7, some of the recoil energy is deposited in the electron reconstruction window($\Delta u_{||}$), which should be subtracted from the recoil energy.

8.2.4 Final State Radiation: $\boldsymbol{u}_T^{\text{FSR}}$

For final state radiated photons, which are far way from the electron, their energies will be included into the hadronic recoil system instead of the electron.

8.3 Over-smearing: Final tuning to the $Z \to ee$ data

As the first step, we have built the hadronic recoil model by dividing it into four parts. There are correlations between the four parts, along with the double-counting we mentioned earlier in this chapter. In simulating the hard component of the recoil, $Z \to \nu\nu$ full MC events have been used and there is always some difference between the full MC and data. To account for the correlation between the four parts and the difference between the full MC and the data, and also to eliminate the double-counting, we introduce "fine-tuning" or "over-smearing", in the form of free tunable parameters, to reflect the differences between our modeled recoil ($Z \to \nu\nu$ + MB + ZB) and collider data.

There are six free parameters, of which three are for the recoil response and the other three for the recoil resolution. These parameters are determined by comparing the simulated recoil using the fast MC to collider data for $Z \to ee$ events and will be plugged back into the fast MC to simulate the recoil of the $W \to e\nu$ events.

Figure 8.5 shows the variables of the η and ξ that we are using in determining the tuning parameters[17]. The η axis is defined as the inner bisector of the angle between the two electrons. The electron direction can be measured very precisely by the tracking system, but the electron energy measured by the calorimeter could fluctuate due to the calorimeter resolution. So the projection of the p_T of the two electrons onto the η axis only depends on the

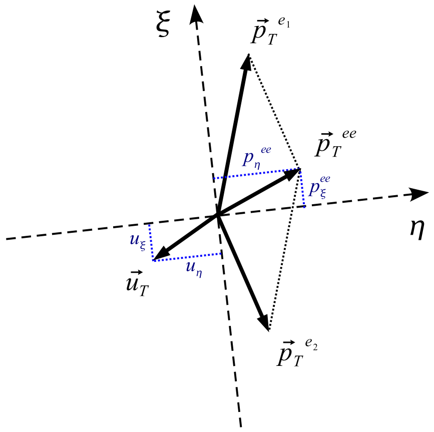

Figure 8.5: The $\eta - \xi$ coordinate system in a $Z \to ee$ event.

directions of the electrons and is less sensitive to their measured energy. By definition, η imbalance (η_{imb}) is the sum of these two projections :

$$\eta_{imb} = \boldsymbol{u}_T \cdot \hat{\eta} + \boldsymbol{p}_T^{ee} \cdot \hat{\eta} \tag{8.4}$$

The mean of the η_{imb} is sensitive to the recoil response and the width of the η_{imb} is sensitive to the recoil resolution. Therefore, the mean and width of the η_{imb} are used to tune the the recoil response and resolution respectively by using the $Z \to ee$ events with a kinematical upper limit of 30 GeV on the recoil p_T both in the both data and the fast MC. We make plots of the mean and width of the η_{imb} versus $\boldsymbol{p}_T^{ee}$. The high $\boldsymbol{p}_T^{ee}$ bins are mainly dominated by the hard component from the initial gluon radiation and hadronization, while the low $\boldsymbol{p}_T^{ee}$ bins are more affected by the soft component from the initial gluon radiation and hadronization. So by dividing events into different $\boldsymbol{p}_T^{ee}$ bins, we can gain some extra sensitivity.

8.3.1 Tuning the Hadronic Response

The formula to over-smear the hadronic response `RelResp` is defined in terms of three tuning parameters named `RelScale`, `RelOffset` and $\tau_{\mathtt{HAD}}$ as follows :

$$\mathtt{RelResp} = \mathtt{RelScale} + \mathtt{RelOffset} \cdot \exp \frac{-q_T}{\tau_{\mathtt{HAD}}} \tag{8.5}$$

Here $\tau_{\mathtt{HAD}}$ describes the response of the calorimeter at low values of the recoil momentum. RelResp is a relative response applied after the hard component modeling in section 8.2.1. It greatly affects the mean value of η_{imb}. q_T is the magnitude of the recoil momentum at the generator level. To determine the fine-tuning parameters, templates of the η imbalance distribution with high statistics are made for the same p_T^Z ranges using the fast MC by varying the values of the above three parameters. A χ^2 is defined by comparing the mean of the η_{imb} versus $\boldsymbol{p}_T^{ee}$ from the data with that from the fast MC templates. By minimizing the χ^2, we found the best fit values are

`RelScale` $= 0.9413 \pm 0.0109$
`RelOffset` $= 1.2016 \pm 0.1783$
$\tau_{\mathtt{HAD}} = 3.1758 \pm 0.8981$ GeV

Figure 8.6 shows the central value and the one standard deviation contour for the `RelScale` and `RelOffset` from the tuning of the hadronic response. Figure 8.7 shows a comparison of the mean of the η imbalance between the data and fast MC, for the ten different p_T^Z bins.

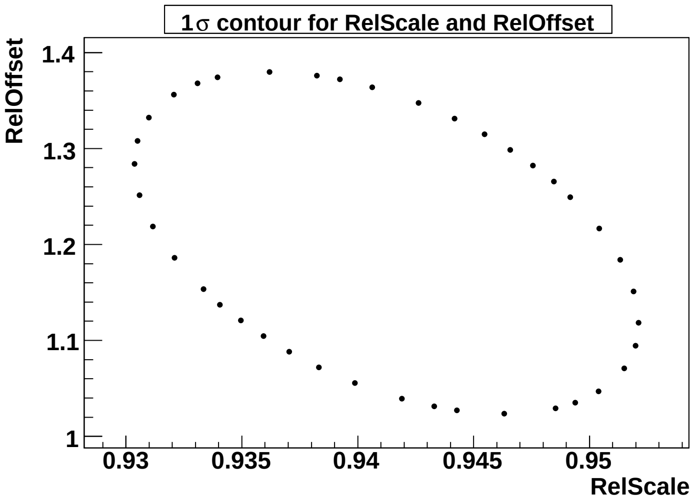

Figure 8.6: Central value and one sigma contour plot for `RelScale` and `RelOffset` corresponding to an optimum value of $\tau_{\mathtt{HAD}} = 3.1758$

8.3.2 Tuning the Hadronic Resolution

The two parameters for the tuning of the hadronic resolution of soft component in our recoil model are `RelSampA` and `RelSampB`. The relative resolution `RelResn` is defined as follows :

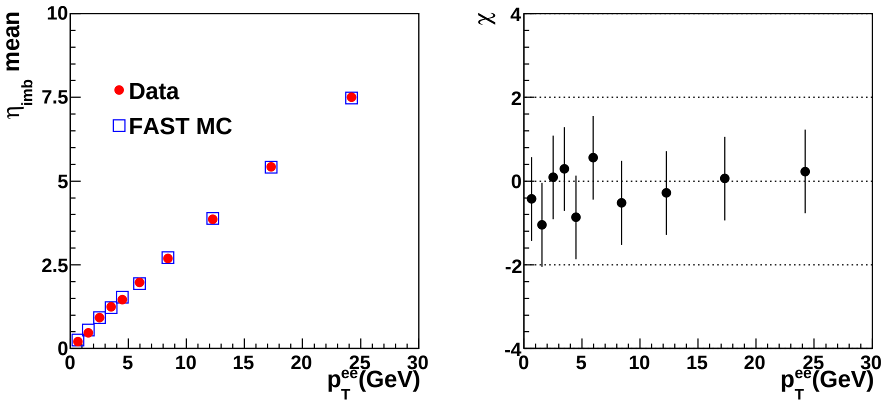

Figure 8.7: DATA and FAST MC comparison of the mean of the η imbalance for the ten different bins in p_T^Z.

$$\texttt{RelResn} = \texttt{RelSampA} + \frac{\texttt{RelSampB}}{\sqrt{q_T}} \tag{8.6}$$

Here q_T is the magnitude of the recoil momentum at the generator level. RelResn is used as a relative resolution smearing applied after the hard component modeling in section 8.2.1. To tune the resolution of the soft component, the multipurpose scale factor α_{mb} introduced earlier is tuned here. The implementation of α_{mb} to tune the soft component is in the same step that has been shown earlier in this chapter as follows :

$$\boldsymbol{u}_T^{\text{SOFT}} = -\ \alpha_{mb} \cdot \boldsymbol{\not{E}_T}^{\text{MB}} -\ \alpha_{zb} \cdot \boldsymbol{\not{E}_T}^{\text{ZB}} \tag{8.7}$$

The α_{mb} is a free parameter used to adjust the MB events in the soft component to help the modeled recoil match the recoil in the data.

The over-smeared hard component by `RelSampA` and `RelSampB` and the over-smeared soft component by α_{mb} and α_{zb} are added to predict the final hadronic recoil p_T, which is used to calculate the η_{imb} in the fast MC to study the hadronic resolution. Just as the previous tuning for the hadronic response, a χ^2 is defined by comparing the width of the η_{imb} versus $\boldsymbol{p}_T^{ee}$ from the data with that from the fast MC templates. By minimizing the χ^2, we found the best fit values are

$\texttt{RelSampA} = 1.0839 \pm 0.0573$
$\texttt{RelSampB} = 0.0$
$\alpha_{mb} = 0.6180 \pm 0.0662$

Here `RelSampB` $= 0.0$ without showing the error is because during the fitting we found `RelSampB` is very consistent with 0 and therefore we fixed it at 0. Figure 8.8 shows the central value and one sigma contour of the α_{mb} and `RelSampA` from the tuning of the hadronic resolution. Figure 8.9 shows a comparison of the width of the η imbalance between the data and FAST MC, for the ten different p_T^Z bins.

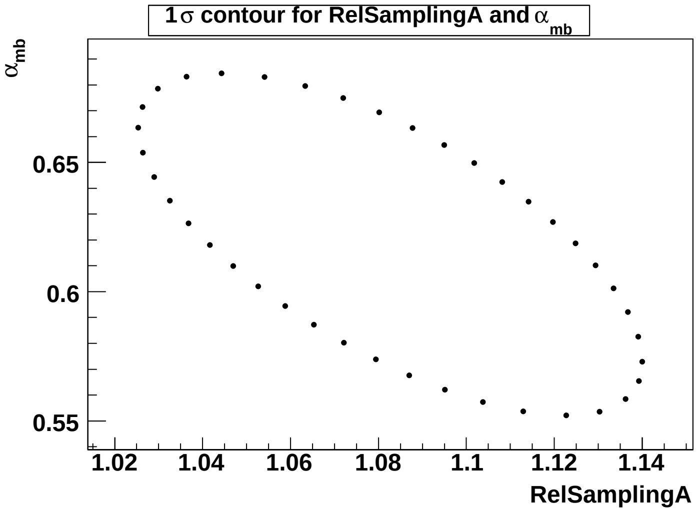

Figure 8.8: Central value and one sigma contour plot for α_{mb} and `RelSampA` corresponding to an optimum value of `RelSampB` $= 0.0$

After tuning the free parameters for the response and resolution of the recoil model, we plug the tuned values into the fast MC to combine with the other components ($\boldsymbol{u}_T^{\mathrm{ELEC}}$ and $\boldsymbol{u}_T^{\mathrm{FSR}}$) to form the final smeared recoil $\boldsymbol{u}_T$.

8.4 W Mass Uncertainty from the Hadronic Recoil

To estimate the effect on the W mass from the hadronic recoil, we propagate the errors of the tuned parameters into the W mass uncertainty. Any imperfections of the model we built as the first step are transferred into the free parameters we are tuning. The procedure to determine the W mass uncertainty due to the various uncertainties here is by performing fast MC studies [60]. Fast MC $W \rightarrow e\nu$ event samples with high statistics are generated by varying the optimal value of the relevant parameter in steps of its standard deviation ($\pm 1\sigma$, $\pm 2\sigma$). These fast MC samples(“fast MC toy samples”) are

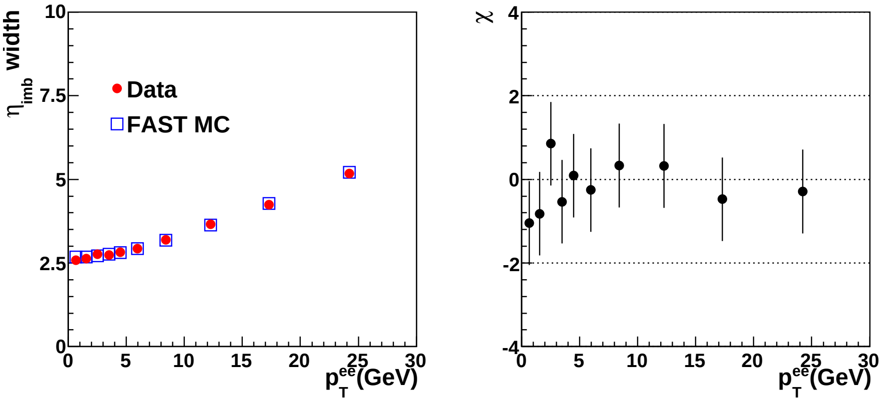

Figure 8.9: Right: DATA and FAST MC comparison of the width of the η imbalance for the ten different bins in p_T^Z.

fit to the templates (also generated from fast MC with the optimal settings of the parameters) to determine the systematic error.

The estimated W mass uncertainty for the three variables(M_T, p_T^e and $\not{E}_T$)are shown in table 8.2.

Table 8.2: Systematic Uncertainties on the W mass obtained for data, due to the recoil model (for $p_T^W < 15$ GeV).

p_T^e method(MeV)	m_T method(MeV)	p_T^ν method(MeV)
12	6	20

Chapter 9

Background

The QCD multi-jet (mostly di-jet) production, $W \to \tau\nu \to e\nu\nu\nu$ and $Z \to ee$ events are the major background sources for $W \to e\nu$ events. QCD and $Z \to ee$ background are measured from the real data and the $W \to \tau\nu$ background is obtained from Geant MC.

9.1 QCD background

Dijet events can pass the W selection cuts if one of the jets mimics an electron and the other is mismeasured. The 2EM and EM+Jet events from collider data(see chapter 4) are used for this background study. The number of W events is extracted using the matrix method:

$$N = N_W + N_{QCD} \tag{9.1}$$

$$N_{trk} = \epsilon_{trk} N_W + f_{QCD} N_{QCD} \tag{9.2}$$

where N_{trk} and N are the numbers of the W candidate events with and without the track matching requirement, N_W is the true number of the real W bosons and N_{QCD} is the number of QCD events for W candidates without track matching requirements. f_{QCD} is the track match fake probability and ϵ_{trk} is the track match efficiency, as described below. f_{QCD} and ϵ_{trk} are measured using em+jet and diem events. The track match requirement we used in our analysis is the good spatial track matching, which means the matched track must have at least one SMT hit and with the track $p_T > 10$ GeV.

Detailed study [62] shows the η_{det} and vertex dependence do not affect the final QCD background shape significantly, even though the fake rate and electron efficiency are strongly dependent on them. We rely on the kinematic spectrum to measure the W mass. The $p_T(e)$ dependence of f_{QCD} and ϵ_{trk}

need to be considered in estimating the QCD background shape and fraction.

9.1.1 f_{QCD} and ϵ_{trk}

EM+jet events are used to study the fake track match probability. These EM+jet events are really dijet events where one of the jets fakes an EM object. The EM+jets samples are skimmed from RunIIa data with an integrated luminosity of 1 fb^{-1}. We select events by requiring an EM cluster that passes the EMID requirements and is back-to-back with a jet passing the JET ID requirements. The fake probability is then the fraction of those EM objects that are found to have a matching track. Figure 9.1 shows the pT dependence of f_{QCD} binned in η_{det}. η_{det} is binned as (-∞, -1.3), (-1.3, -1.1), ..., (1.1, 1.3), (1.3, +∞).

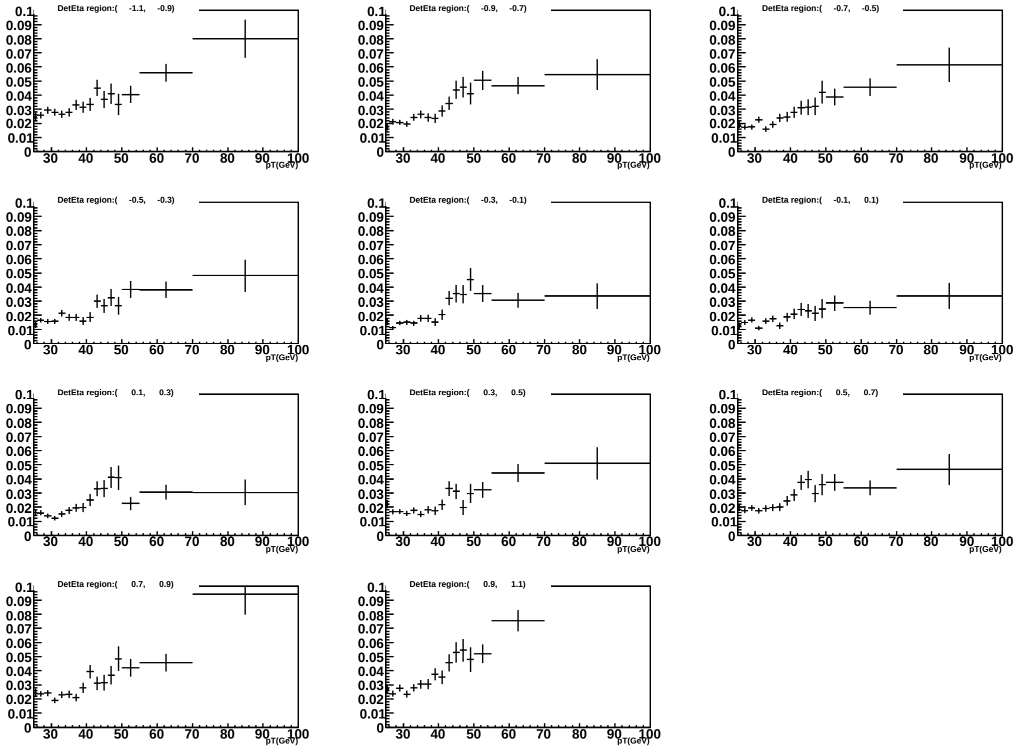

Figure 9.1: f_{QCD} in η_{det} bins

$Z \rightarrow ee$ events from RunIIa are used to study the single electron efficiency. The tag-and-probe method is used [52]. This method was found to bring some bias based on GEANT MC studies. A 2% uncertainty due to the tag-and-probe method bias [52] is added as the systematic uncertainty of track matching efficiency measured using the tag-probe method. Figure 9.2 shows the p_T dependence of ϵ_{trk} binned in η_{det}.

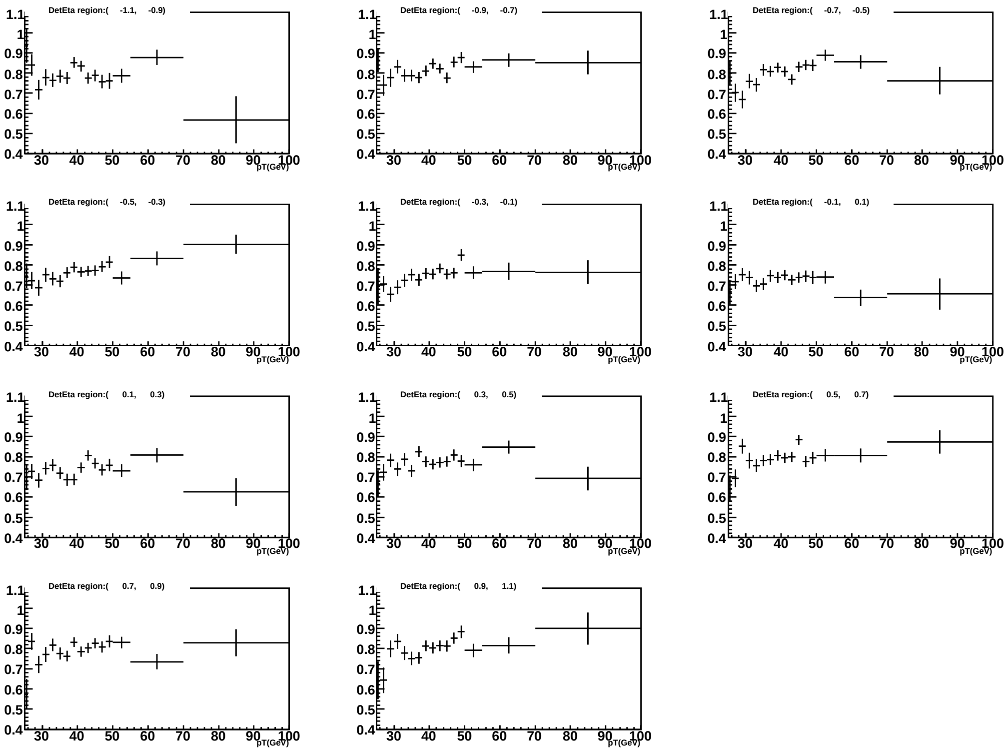

Figure 9.2: ϵ_{trk} in η_{det} bins

With the fake rate and electron efficiency we obtained, we are able to calculate the background shape using the matrix method described above. The QCD background fraction is $(1.49 \pm 0.03)\%$.

9.2 $Z \rightarrow ee$ Background

The $Z \rightarrow ee$ events enter the $W \rightarrow e\nu$ sample when one of the electrons is not identified and there is substantial missing transverse momentum from mismeasurement. First let us scrutinize how $Z \rightarrow ee$ events fake $W \rightarrow e\nu$ events. By plotting the true η_{det} of the two electrons in full MC $Z \rightarrow ee$ events which pass the standard $W \rightarrow e\nu$ selection in figure 9.3, we see the $Z \rightarrow ee$ events fake $W \rightarrow e\nu$ events mainly by one of the electrons falling into the Intercryostat region(ICR)($1.1 < |\eta_{det}| < 1.4$) and getting lost, therefore causing a large missing energy reconstructed. Since our geant simulation is not doing a good job in describing the real ICR detector, it is certainly necessary to find another way to estimate the $Z \rightarrow ee$ Background. We directly extract the $Z \rightarrow ee$ events from the real $W \rightarrow e\nu$ data.

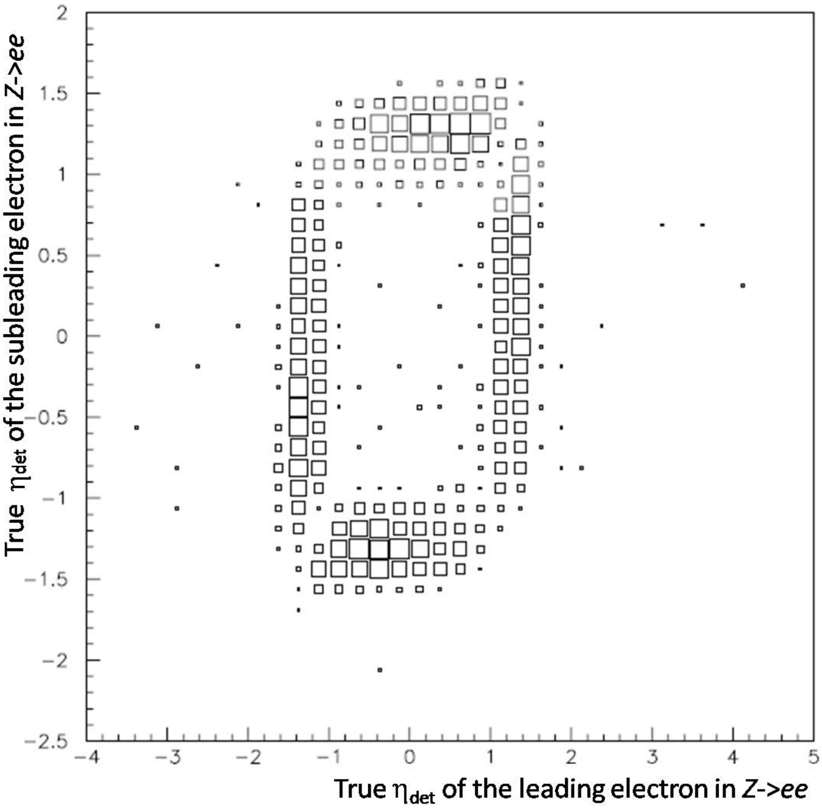

Figure 9.3: True η_{det} of the two electrons in the full MC $Z \rightarrow ee$ events

The requirements used in selecting $Z \rightarrow ee$ events out of $W \rightarrow e\nu$ data are listed below.

- Pass standard $W \rightarrow e\nu$ selection.
- Require a track with the following properties:
  - back to back with the electron
  - $p_T > 25$ GeV
  - $1.0 < |\eta_{det}| < 1.5$
  - $|z_0 - z_{PV}| < 1$ cm

- opposite charge of the track to the electron
- Scalar sum over p_T of all other tracks within a cone of $\Delta R < 0.4$ around our track has to be smaller than 4 GeV. Here ΔR is the distance in $\eta \times \phi$ space
- Mass cut: 70 <invariant mass(track, cluster)< 110 GeV

Using this method, the fraction of $Z \to ee$ background is found to be $(0.80 \pm 0.01)\%$.

9.3 $W \to \tau\nu$ Background

The $W \to \tau\nu$ events, where the τ decays into $e\nu\nu$, could fake the $W \to e\nu$ signal. The electron from τ decay is much softer than the one directly from W decay. Instead of the Jacobian peak at $M_W/2$, the peak appears at low momenta and falls off rapidly. According to lepton universality, the cross sections of W decays into electrons and τ leptons are the same, but the τ background is further reduced by the branching ratio of the subsequent $\tau \to e\nu\nu$ decay. Using a detailed simulation of this process, we determine the $W \to \tau\nu \to e\nu\nu\nu$ background fraction to be $(1.60 \pm 0.02)\%$.

9.4 Systematics from backgrounds on the W mass Measurement

The backgrounds from QCD, $W \to \tau\nu$ and $Z \to ee$ are normalized in the same plot, which is shown in figure 9.4. The W mass uncertainty due to each background is estimated separately by varying it by $\pm\sigma$ after adding all the three background to the signal predicted by the fast MC. The results are summarized in table 9.1. We take the background systematic uncertainties to be uncorrelated with each other.

	Fraction	Uncertainty M_T (MeV)	Uncertainty $p_T(e)$ (MeV)	Uncertainty $\not\!\!E_T$ (MeV)
QCD	(1.49±0.03)%	2	4	3
$Z \to ee$	(0.80±0.01)%	1	2	2
$W \to \tau\nu$	(1.60±0.02)%	1	2	2

Table 9.1: W mass uncertainty due to the QCD, $W \to \tau\nu$ and $Z \to ee$ backgrounds.

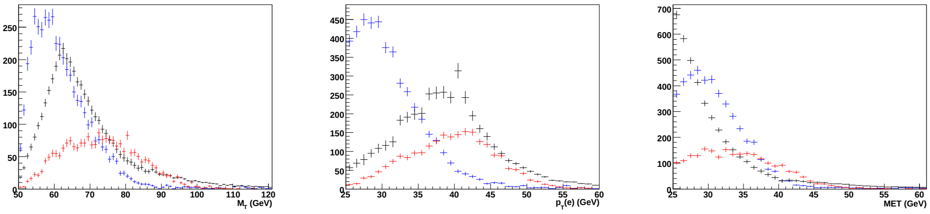

Figure 9.4: m_T, $p_T(e)$ and $\not\!\!E_T$ of three different backgrounds with the proper relative normalization. Black: QCD, Red: $Z \to ee$, Blue: $W \to \tau\nu$.

Chapter 10

Systematic Uncertainties

As discussed separately in the previous chapters, the fast MC is composed of different parts from different sources, which are parameterized. The parameters of these different parts have their own uncertainties and therefore have their own effects on the W mass uncertainty. To estimate the W mass uncertainty due to one specific parameter of the fast MC, we use a large ensemble of pseudo-experiments simulated using the fast MC. A set of high statistics W mass templates are generated using the fast MC with the default parameters. Pseudo-experiments are performed in a way that a specific parameter is varied individually $\pm 1\sigma$ and $\pm 2\sigma$ while keeping all the other parameters unchanged. The pseudo-experiments are fitted using the W mass templates and therefore the W mass shifts due to the variance of the specific parameter by $\pm 1\sigma$ and $\pm 2\sigma$ are obtained. The W mass change due to the change of the parameter is fit to a line and the slope of the line is used in the usual error propagation formula:

$$\sigma^2_{M_W}(X) = \left(\frac{\partial M_W}{\partial X}\right)^2 \sigma^2_X, \tag{10.1}$$

where $\frac{\partial M_W}{\partial X}$ is the slope and σ_X is the uncertainty on parameter X. This formula does not include correlations and in many cases we can safely assume the parameters are nearly uncorrelated. In case there is a strong unavoidable correlation, we use the more correct formula which is (here for just two parameters. The extension to three or more parameters can be easily achieved in the same manner.):

$$\sigma^2_{M_W}(X) = \left(\frac{\partial M_W}{\partial X_1}\right)^2 \sigma^2_{X_1} + \left(\frac{\partial M_W}{\partial X_2}\right)^2 \sigma^2_{X_2} + 2\sigma^2_{12}\left(\frac{\partial M_W}{\partial X_1}\right)\left(\frac{\partial M_W}{\partial X_2}\right) \tag{10.2}$$

where σ_{12} is the covariance found using the error matrix[1].

10.1 Theoretical Uncertainties

The theoretical uncertainties of the W mass measurement are coming from the theoretical model we use to generator the events. In chapter 5, we already introduced the event generation and their contribution to the W mass uncertainty. Here is the summary.

10.1.1 PDF

The Parton Distribution Functions(PDFs) are derived from fitting experimental results and the uncertainties are propagated to the PDF and then to the W mass measurement. The contribution to the mass uncertainty is 10 MeV for m_T, 11 MeV for $p_T(e)$ and 11 MeV for $\not{E}_T$. The systematic error due to the PDF uncertainties is the leading uncertainty from the theoretical description of W boson production.

10.1.2 Boson p_T

For the DØ W mass measurement, the uncertainty due to the theoretical description of the transverse momentum spectrum of the boson depend most significantly on the value of g_2 in the BLNY parametrization[43] of the non-perturbative region of the spectrum. We use the global fit value of 0.68 ± 0.02 and propagate this uncertainty to the W mass measurement. We find the W mass uncertainty of 2 MeV when using m_T, 5 MeV when using $p_T(e)$ and 2 MeV for the $\not{E}_T$ distribution.

10.1.3 Electroweak Corrections

The dominant electroweak uncertainties come from the final state radiation(FSR). Other electroweak processes, such as ISR, ISR-FSR interference, etc., are studied using WGRAD and ZGRAD programs [50], which are not actually event generators and are used to calculate the cross-sections for these processes. The electroweak effect contains the minimum photon energy cut, ISR, ISR-FSR interference, photon merge, etc. We find that the uncertainty contribution to

---

[1] Error matrix contains information of errors of individual parameters and their correlation. The diagonal elements are the square of each parameter error. Other elements are the covariance of a pair of parameters, which takes into account their correlation.

the W mass to be 7 MeV for $p_T(e)$, 7 MeV for m_T and 9 MeV for the $\not\!\!E_T$ distribution.

10.2 Experimental Uncertainties

10.2.1 Electron Energy Response

The electron energy response has been tuned using the $Z \rightarrow ee$ data(Chapter 7). Although the individual errors of the scale and the offset are large, the propagated W mass uncertainty after taking into account of the their high anti-correlation(almost -100%) are greatly reduced. Using this correlation we find that the systematic uncertainty on the electron energy is 33 MeV,using m_T, $p_T(e)$ and $\not\!\!E_T$. It is the dominant systematic uncertainty for the W mass measurement and simply limited by the $Z \rightarrow ee$ statistics.

10.2.2 Electron Energy Resolution

The electron energy resolution is described by three terms: Constant, Sampling and Noise(chapter 7). Thanks to the fact we are dealing with electrons with high energy, the noise contribution is negligible. The sampling term was determined using the single electron full MC events. Then the constant term was determined by forcing the simulated Z in the fast MC to agree with the one measured in the data. So the error of the constant term from the final step tuning contains the uncertainty from both the noise and constant terms. The W mass uncertainty from the electron energy resolution is found to be small and is estimated to be 2 MeV for m_T and $p_T(e)$ of the electron and 3 MeV for $\not\!\!E_T$.

10.2.3 Electron Energy Non-linearity - Detector Material Understanding

The non-linearity of the electron energy response is mainly caused by the upstream material, namely the dead material in front of the calorimeter. The impact of the dead material was accounted for by the energy loss correction applied to the data(chapter 4). The error of the amount of the dead material used is propagated into the W mass uncertainty. The uncertainty of the amount of the upstream material results in a W mass uncertainty of 4 MeV m_T, 6 MeV $p_T(e)$ and 7 MeV for the $\not\!\!E_T$.

10.2.4 Quality of the Electron Energy Loss Corrections

In chapter 7, we discussed the possible bias caused by the different E/η^{phys} space of electrons from $Z \to ee$ and $W \to e\nu$ events, which we found was negligible in the end. Its propagated W mass uncertainty is 4 MeV by using m_T, $p_T(e)$ and $\not{E}_T$.

10.2.5 Efficiency

The most influential efficiency for the W mass uncertainty is the $u_{\|}$ efficiency(chapter 6). The $u_{\|}$ efficiency was fitted with three parameters. Among them, what really matters to the W mass measurement is the kink point and the slope. Their errors along with the correlation are propagated into the W mass uncertainty. This uncertainty was determined in two steps: First, the determination of the efficiency itself from the $Z \to ee$ events, and second the scaling of this efficiency to the W events, determined using the DØGeant detector simulation. Together the uncertainty is 5 MeV for m_T, 6 MeV for $p_T(e)$ and 5 MeV for $\not{E}_T$.

10.2.6 Hadronic Recoil

The hadronic recoil is another major source for the W mass uncertainty because it largely affects the determination of $\not{E}_T$ and therefore m_T(chapter 8). The errors of the parameters for the final tuning of the hadronic recoil are propagated into the W mass uncertainty due to the recoil. The total uncertainty including the hadronic response and resolution is 6 MeV for m_T, 12 MeV for $p_T(e)$ and 20 MeV for $\not{E}_T$.

10.2.7 Background

The systematics from the background(chapter 9) are 2 MeV for m_T, 5 MeV for $p_T(e)$ and 4 MeV for $\not{E}_T$. They have a small contribution to the total W mass uncertainty.

10.3 Summary of the W Mass Uncertainties

The systematic uncertainties due to different sources are summarized in table 10.1. First listed are the experimental uncertainties and second are the theoretical uncertainties, both summed separately. The dominant experimental systematic uncertainty is from the electron energy response. Other major contributions such as the hadronic recoil and efficiency, etc. are also studied by

Source	$\sigma(m_W)$ MeV m_T	$\sigma(m_W)$ MeV $p_T(e)$	$\sigma(m_W)$ MeV $\not{E}_T$
Experimental			
Electron Energy Scale	34	34	34
Electron Energy Resolution Model	2	2	3
Electron Energy Nonlinearity	4	6	7
W and Z Electron energy loss differences	4	4	4
Recoil Model	6	12	20
Electron Efficiencies	5	6	5
Backgrounds	2	5	4
Experimental Total	35	37	41
W production and decay model			
PDF	10	11	11
QED	7	7	9
Boson p_T	2	5	2
W model Total	12	14	14
Total	37	40	43

Table 10.1: Systematic uncertainties on the W mass results.

using the $Z \rightarrow ee$ events from collider data. So the $Z \rightarrow ee$ statistics is the limiting factor in improving the experimental systematics.

Chapter 11

Result

11.1 Monte Carlo Closure Test

In previous chapters, the procedure and the various techniques in measuring the W boson mass have been introduced, some of them in detail. To validate the whole procedure and the techniques that will be used on data, we performed a closure test using the standard DØ full Monte Carlo simulation. We treated the full MC sample as collider data to apply the analyzing procedure, including performing the Z boson-based tuning using simulated events.

The differences Δm_W between the fitted W mass and input W mass value of 80.450 GeV are $\Delta m_W = -0.009 \pm 0.015(\text{stat}) \pm 0.011 \pm 0.010$ GeV, $\Delta m_W = -0.009 \pm 0.019(\text{stat}) \pm 0.007 \pm 0.010$ GeV and $\Delta m_W = -0.021 \pm 0.019(\text{stat}) \pm 0.011 \pm 0.010$ GeV for the m_T, $p_T(e)$ and $\not{E}_T$ fits respectively. The first uncertainty is from W statistics in the full Monte Carlo sample, the second uncertainty is from the statistics of the Z used in the tuning, and the third uncertainty is due to the residual difference between Z and W in the energy loss corrections because electrons in the full Monte Carlo sample from W decay have different energy and η distributions from those from Z decay.

11.2 Result for 1 fb^{-1} Collider Data

$Z \to ee$ events have been largely used as control sample in many aspects of the analysis, including the data calibration, parameter tuning of the fast MC. In particular, $Z \to ee$ events were used to calibrate the electron energy response by forcing the reconstructed Z mass to agree with the world average. So after all the tuning for the fast MC, it is necessary to check how we have done in predicting the $Z \to ee$ events using the fast MC, especially if the measured Z mass agrees with with world average as expected. The Z mass fit is shown in figure 11.1. For an input value $m_Z = 91.188$ GeV used in the tuning, the value returned from the fit is 91.185 ± 0.033(stat).

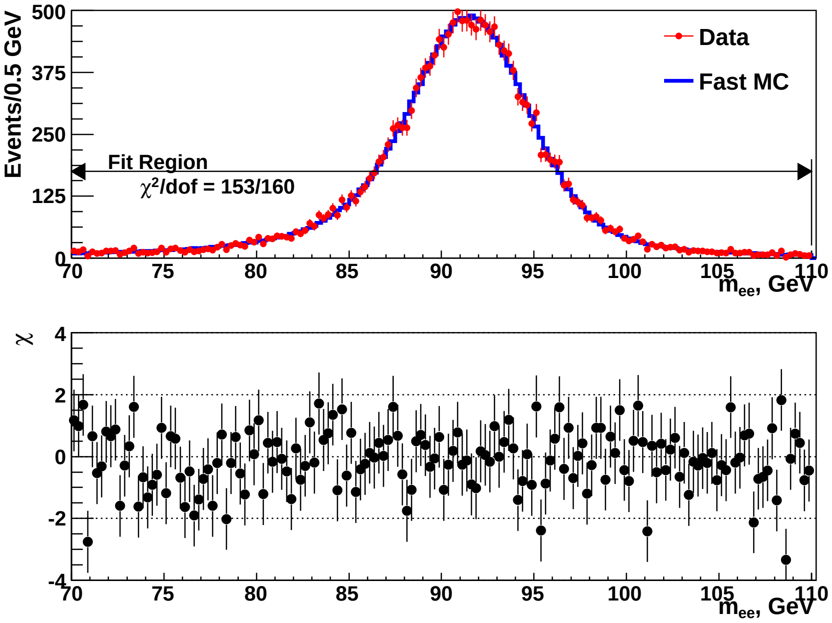

Figure 11.1: The Z mass distribution in data and from the fast simulation (top) and the χ values for each bin (bottom).

Figure 11.2, 11.3 and 11.4 show the distributions of m_T, $p_t(e)$, $\not{E}_T$ with the data and the fast simulation with the background for the best fit value. These figures also show the bin-by-bin χ values defined as the difference between the data and the fast simulation divided by the data uncertainty. The potential structure in the χ plot in figure 11.4 resides in a region of the distribution that does not carry much mass information.

The measured W mass from the data are shown in table 11.1. One might wonder why the statistical uncertainty by using the $\not{E}_T$ fit is smaller than that by using the $p_T(e)$ fit since we use the same fit range for both them. The reason is because the average recoil response is not close to 100%, but just about 60%. So the inferred $\not{E}_T$ magnitude is scaled down. Equivalently we squeeze more events into the same range for the $\not{E}_T$ distribution. This is confirmed by changing the recoil response to 100% in the fast simulation.

Figure 11.5, 11.6 and 11.7 show the variations of the fitted W mass values by changing the lower or higher limit of the fit range.

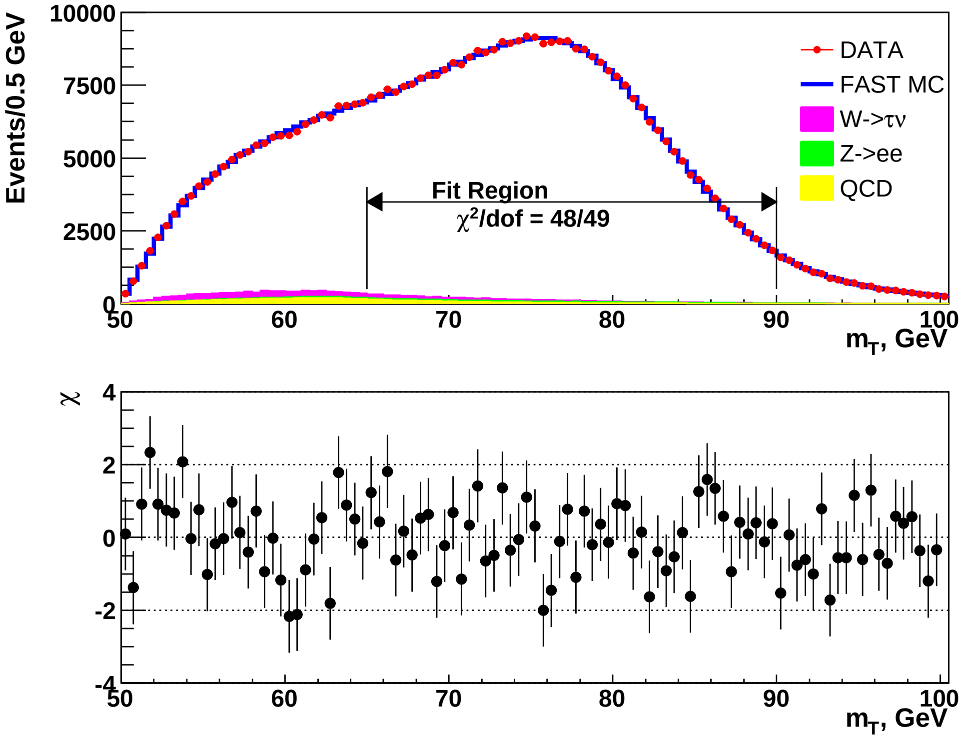

Figure 11.2: The m_T distribution for the data and fast simulation with backgrounds added.

Variable	Fit Range (GeV)	Result (GeV)	χ^2/dof
m_T	$65 < m_T < 90$	80.401 ± 0.023	48/49
$p_T(e)$	$32 < p_T(e) < 48$	80.400 ± 0.027	39/31
$\not{E}_T$	$32 < \not{E}_T < 48$	80.402 ± 0.023	32/31

Table 11.1: W mass results from the fits to the data. The uncertainty is only the statistical component. The χ^2/dof values are computed over the fit range.

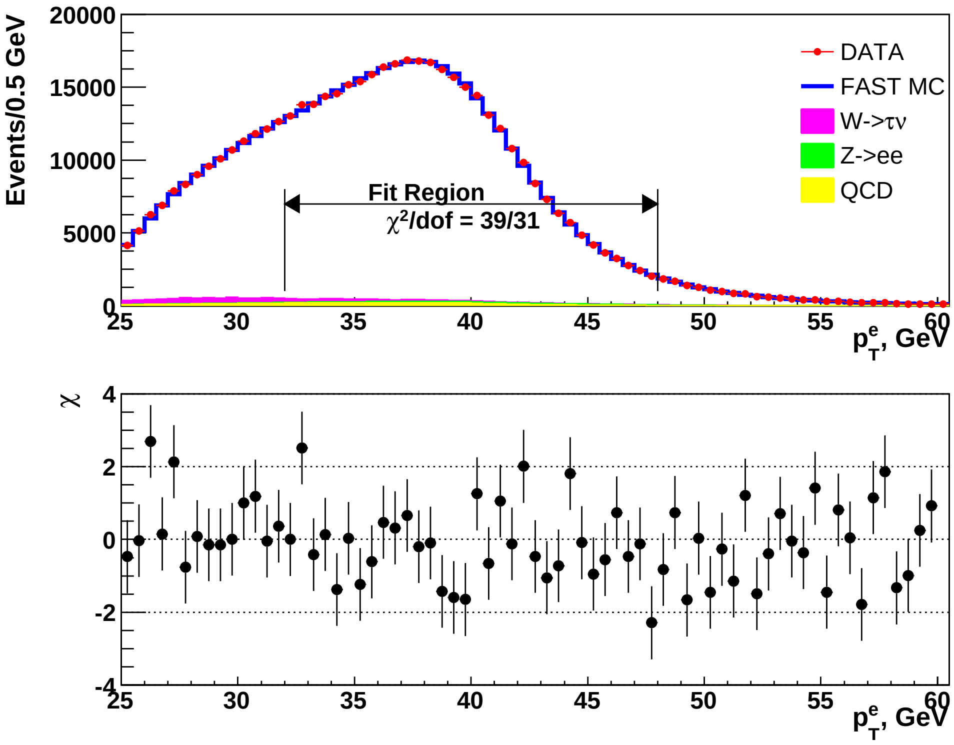

Figure 11.3: The $p_T(e)$ distribution for the data and fast simulation with backgrounds added.

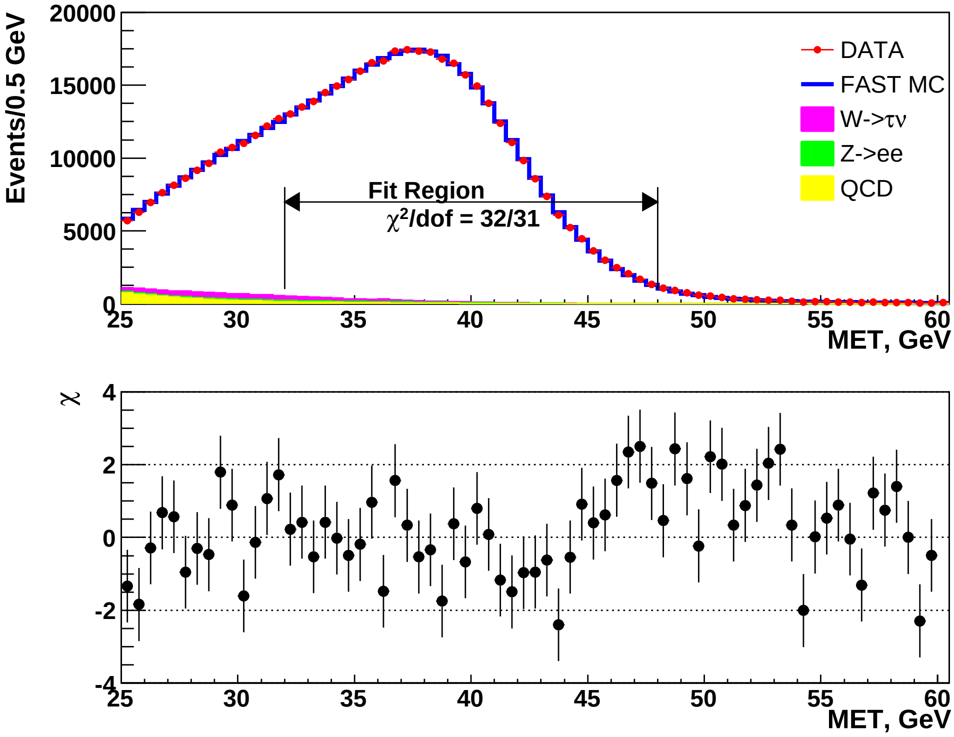

Figure 11.4: The $\not\!\!E_T$ distribution for the data and fast simulation with backgrounds added.

11.3 Combination of Results from Different Observables

To combine the results from the three observables(m_T, $p_T(e)$ and$\not\!\!E_T$), ensemble tests and standard uncertainty propagation methods are used to determine the correlation matrix[1] which is found to be

$$\rho = \begin{pmatrix} \rho_{m_T m_T} & \rho_{m_T p_T(e)} & \rho_{m_T \not E_T} \\ \rho_{m_T p_T(e)} & \rho_{p_T(e) p_T(e)} & \rho_{p_T(e) \not E_T} \\ \rho_{m_T \not E_T} & \rho_{p_T(e) \not E_T} & \rho_{\not E_T \not E_T} \end{pmatrix} = \begin{pmatrix} 1.0 & 0.83 & 0.82 \\ 0.83 & 1.0 & 0.68 \\ 0.82 & 0.68 & 1.0 \end{pmatrix}$$

,

where correlations between the three observables due to statistics, electron energy response, recoil model and the PDF systematics have been considered. All other sources of systematics (such as QED, backgrounds, efficiencies) have been considered as 100% correlated. The results from the three observables are combined [63] using this correlation matrix. The combined result is

$$m_W = 80.401 \pm 0.021 \text{ (stat)} \pm 0.038 \text{ (syst) GeV} = 80.401 \pm 0.043 \text{ GeV.}$$

11.4 Consistency Check

To check the stability of the W mass result, we performed a bunch of consistency checks. The basic idea is that we change some aspect of the analysis, especially the parameter on which we model the dependence, to check if we still can obtain consistent result.

A first set of consistency checks has already been presented in the previous section where we have shown the variation of the measured W mass due to the change of the fitting range. Here we present additional checks which are directly plugged in the middle of the analysis. As mentioned earlier in chapter 3, we are essentially measuring the the ratio of the W and Z mass. What really matters is the effect on the measured boson mass ratio by changing some aspect of this analysis. This means that, whenever we change something in the analysis for a consistency check, we should retune the EM energy scale to the Z. However, we did not do it this way. Instead, we studied the impact of a cut variation or a sample splitting simultaneously in both the data and fast MC to measure the W mass and Z mass separately. Then we check how the W/Z mass ratio changed.

---

[1] The correlation matrix is obtained from the error matrix by dividing each of its elements by the corresponding pair of parameter errors.

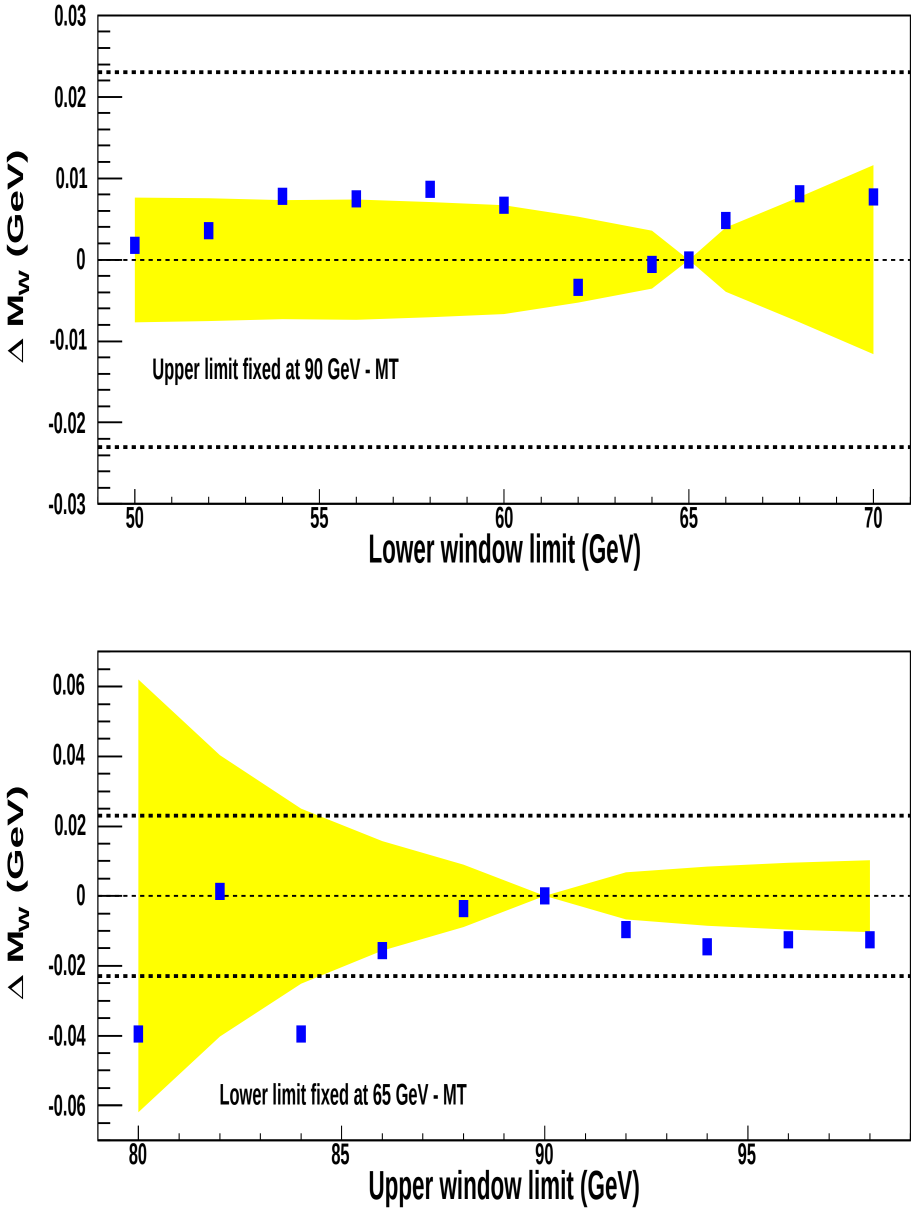

Figure 11.5: Sensitivity of the fitted mass values to the choice of fit interval for m_T distributions when upper edge is fixed (top) and lower edge is fixed (bottom). The yellow regions indicate the expected statistical variations from simulation pseudoexperiments. The dashed lines indicate the statistical uncertainty on the m_W fit using the default fit range.

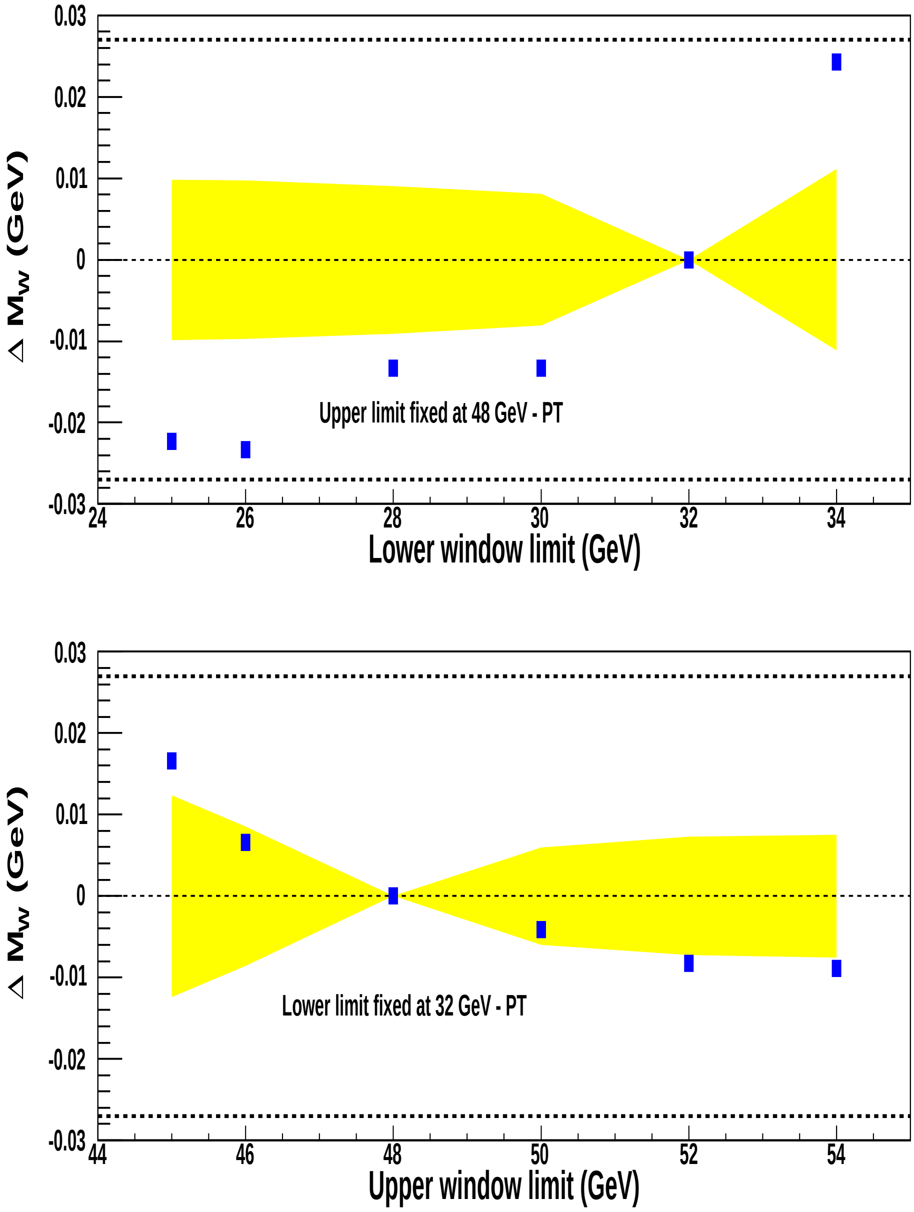

Figure 11.6: Sensitivity of the fitted mass values to the choice of fit interval for $p_T(e)$ distributions when upper edge is fixed (top) and lower edge is fixed (bottom). The yellow regions indicate the expected statistical variations from simulation pseudoexperiments. The dashed lines indicate the statistical uncertainty on the m_W fit using the default fit range.

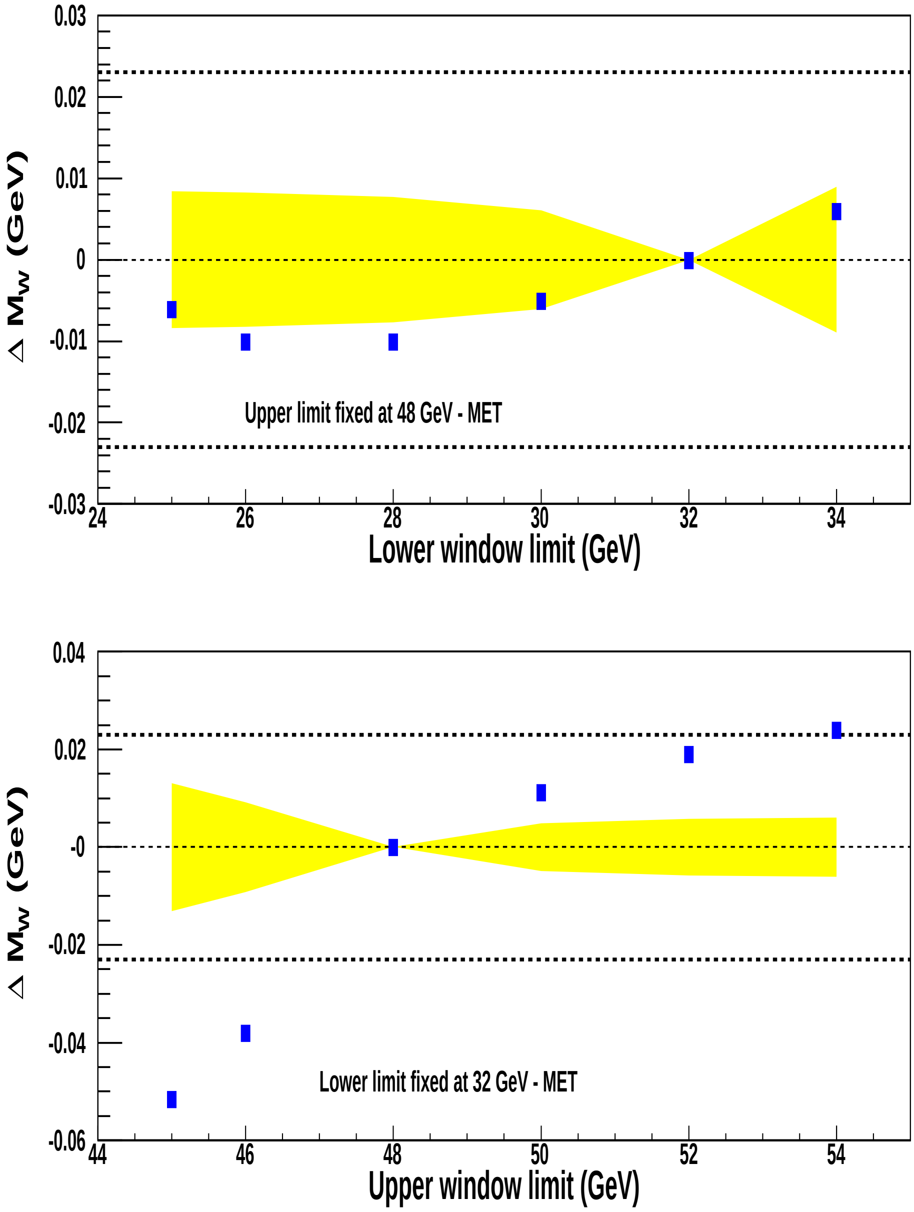

Figure 11.7: Sensitivity of the fitted mass values to the choice of fit interval for $\not\!\!E_T$ distributions when upper edge is fixed (top) and lower edge is fixed (bottom). The yellow regions indicate the expected statistical variations from simulation pseudoexperiments. The dashed lines indicate the statistical uncertainty on the m_W fit using the default fit range.

11.4.1 Instantaneous luminosity

We split the data sample into a "low lumi" subsample (per-tick[2] lumi $< 1 \cdot 10^{30}$ cm^{-2} s^{-1}) and a "high lumi" subsample (per-tick lumi $> 1 \cdot 10^{30}$ cm^{-2} s^{-1}). We chose to divide the sample in this way so that both subsamples have approximately the same size. The W mass and Z mass measurements for each subsample, as well as the resulting mass ratios are summarised in figure 11.8. The "relative change in mass ratio" shown in the right plot of figure 11.8 is defined as the ratio of measured W and Z mass (taking into account the statistical uncertainties on both masses) divided by the ratio of the nominal result for the W mass from the m_T observable (80.011 GeV) and the nominal result for the Z mass (91.185 GeV), not adding any uncertaities from the nominal values. As we can see, the "relative change in mass ratio" is consistent with one as expected.

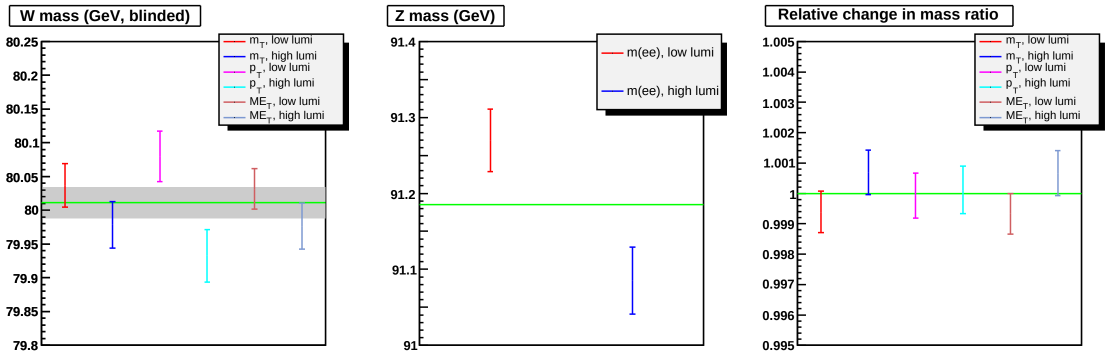

Figure 11.8: Left: W mass as measured from the m_T, $p_T(e)$ and $p_T(\nu)$ observables, separately for the "low lumi" and the "high lumi" subsamples. The green line and grey band indicate the nominal result from the m_T observable and its uncertainty. Middle: Z mass as measured from the di-electron invariant mass spectrum, separately for the two subsamples. The green line shows the nominal result from the fit to the full Z sample. Right: The resulting mass ratios, separately for the m_T, $p_T(e)$ and $\not\!\!E_T$ observables and for the two subsamples, normalised to the default mass ratio. The green line indicates unity.

---

[2] One tick is 132 ns.

11.4.2 Time

We can also split our data sample into an "early" subsample (before August 2004) and a "late" subsample (after August 2004). The measured W mass and Z mass measurements for each of of the two subsamples, as well as the measured mass ratios are summarized in figure 11.9. The measured "relative change in mass ratio" is consistent with one.

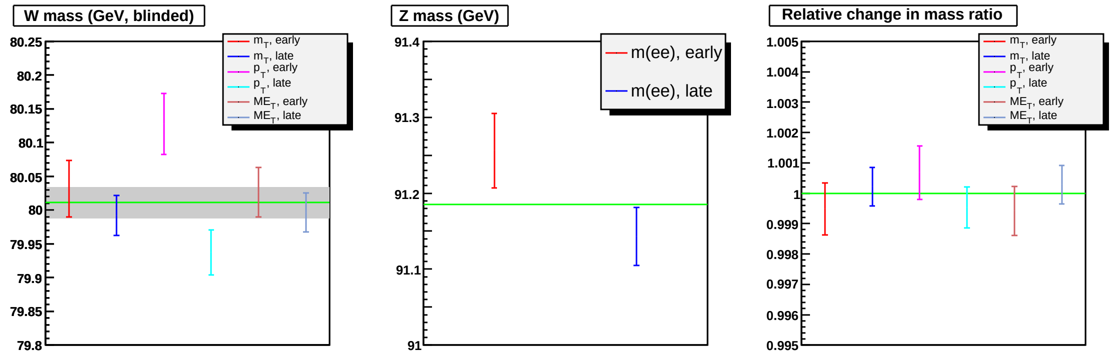

Figure 11.9: Left: W mass as measured from the m_T, $p_T(e)$ and $p_T(\nu)$ observables, separately for the "early" and the "late" subsamples. The green line and grey band indicate the nominal result from the m_T observable and its uncertainty. Middle: Z mass as measured from the di-electron invariant mass spectrum, separately for the two subsamples. The green line shows the nominal result from the fit to the full Z sample. Right: The resulting mass ratios, separately for the m_T, $p_T(e)$ and $\not{E}_T$ observables and for the two subsamples, normalised to the default mass ratio. The green line indicates unity.

11.4.3 Scalar E_{T}(SET)

We now split the data sample into an "low SET" subsample (SET $<$ 50 GeV) and a "high SET" subsample (SET $>$ 50 GeV). The measured W mass and Z mass for each subsample, as well as the resulting mass ratios are summarized in figure 11.10. Again, the "relative change in mass ratio" is consistent with unity.

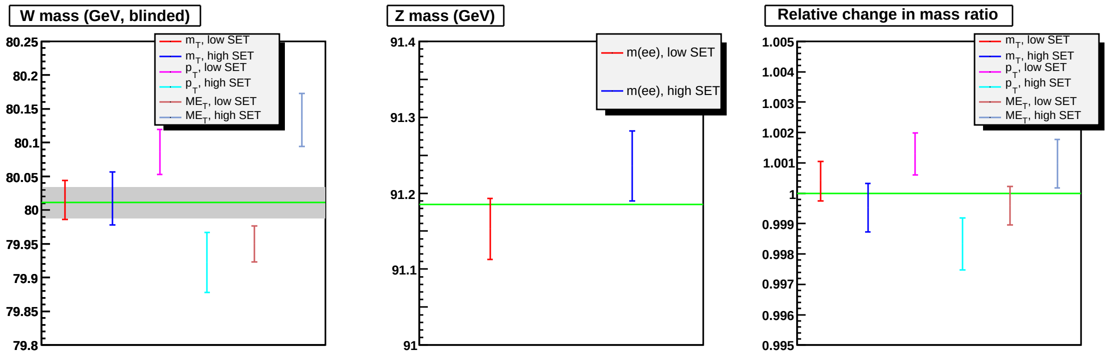

Figure 11.10: Left: W mass as measured from the m_T, $p_T(e)$ and $p_T(\nu)$ observables, separately for the “low SET” and the “high SET” subsamples. The green line and grey band indicate the nominal result from the m_T observable and its uncertainty. Middle: Z mass as measured from the di-electron invariant mass spectrum, separately for the two subsamples. The green line shows the nominal result from the fit to the full Z sample. Right: The resulting mass ratios, separately for the m_T, $p_T(e)$ and $\not{E}_T$ observables and for the two subsamples, normalised to the default mass ratio. The green line indicates unity.

11.4.4 Phi fiducial cut

We now vary the phi fiducial requirement. The default requirement, PhiMod [3]< 0.80, cuts away 10 % of the phase space at each edge of each CCEM module. We also study two tighter versions of the requirement, namely PhiMod< 0.75 and PhiMod< 0.70. The effects of these cut variations are summarized in figure 11.11. Again, the “relative change in mass ratio” is consistent with unity.

11.4.5 u_{T} cut

We now vary the u_{T} requirement. The default requirement is $u_{\mathrm{T}} < 15$ GeV. We now study one tighter version and one more loose version of this requirement, namely $u_{\mathrm{T}} < 10$ GeV and $u_{\mathrm{T}} < 20$ GeV. The effects of these cut variations are summarized in figure 11.12. Again, the “relative change in mass ratio” is consistent with unity.

---

[3] See section 6.1.

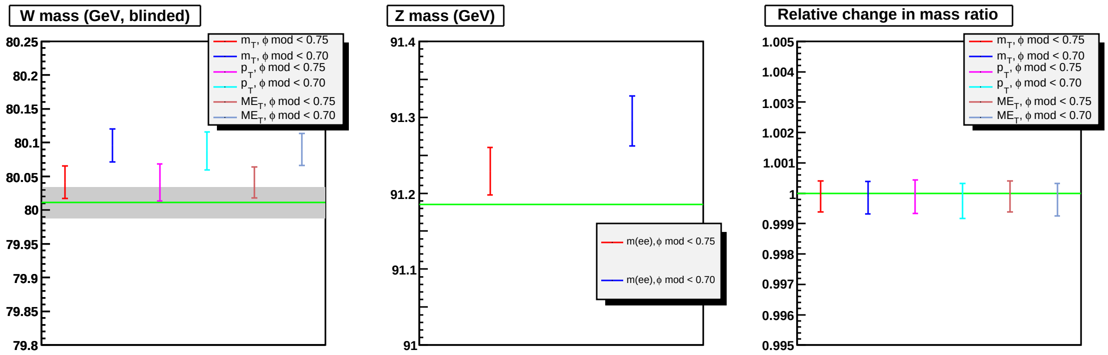

Figure 11.11: Left: W mass as measured from the m_T, $p_T(e)$ and $p_T(\nu)$ observables, separately for two variations of the phi fiducial cut. The green line and grey band indicate the nominal result from the m_T observable and its uncertainty. Middle: Z mass as measured from the di-electron invariant mass spectrum, separately for the two cut variations. The green line shows the nominal result from the fit to the default Z sample. Right: The resulting mass ratios, separately for the m_T, $p_T(e)$ and $\not{E}_T$ observables and for the two cut variations, normalized to the default mass ratio. The green line indicates unity.

11.4.6 $u_{||}$

We now split the W sample into a subsample of negative $u_{||}$ and a subsample of positive $u_{||}$. There is no direct equivalent of this splitting for the Z sample, because there are two electrons from each Z decay that are reconstructed in roughly opposite directions in the transverse plane. It does not matter for the purpose of our discussion since we expect the W mass to be stable on its own under this splitting, since we model the $u_{||}$ in the fast MC. The W mass as measured in the two subsamples is shown in figure 11.13 (first six data points). The results from each of the two subsets agree with each other: our measurement is stable.

The difference in central values for the m_T and $p_T(\nu)$ observables is somewhat larger than for the $p_T(e)$ observable. Upon closer inspection, one finds that this difference is related to the same events that cause the fluctuation in Fig. 11.4: the events in question “live” at $\not{E}_T \gtrsim 45$ GeV and $m_T \gtrsim 90$ GeV. The difference in central values from the m_T and $\not{E}_T$ observables vanishes almost completely when the fitting range is slightly reduced at the upper end (last four data points in figure 11.13).

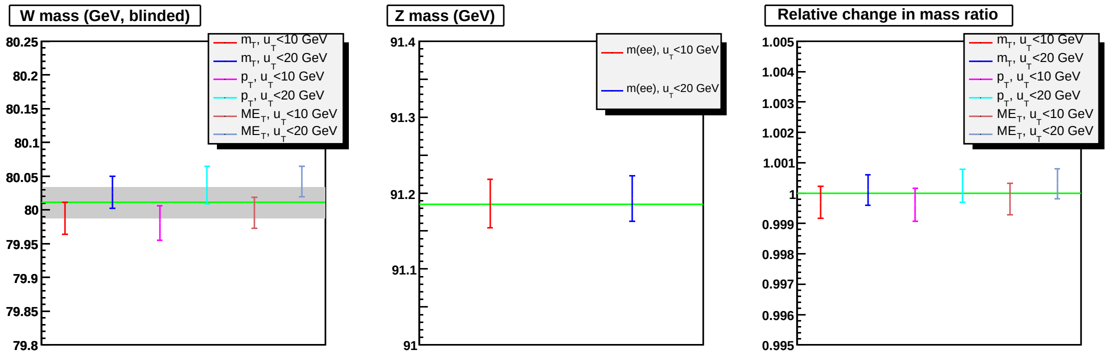

Figure 11.12: Left: W mass as measured from the m_T, $p_T(e)$ and $p_T(\nu)$ observables, separately for two variations of the u_{T} cut. The green line and grey band indicate the nominal result from the m_T observable and its uncertainty. Middle: Z mass as measured from the di-electron invariant mass spectrum, separately for the two cut variations. The green line shows the nominal result from the fit to the default Z sample. Right: The resulting mass ratios, separately for the m_T, $p_T(e)$ and $\not\!\!E_T$) observables and for the two cut variations, normalized to the default mass ratio. The green line indicates unity.

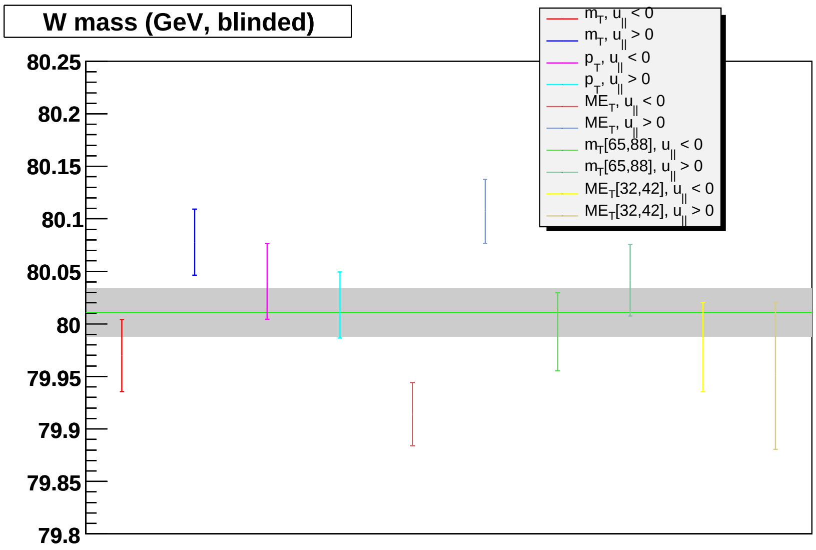

Figure 11.13: W mass as measured from the m_T, $p_T(e)$ and $\not{E}_T$ observables, separately for the subsamples of negative and positive $u_{||}$. For the m_T observable, in addition to the results obtained using the nominal fitting range ($65-90$ GeV), we also report results from the slightly more restricted fitting range $65-88$ GeV. Similarly, for the $p_T(\nu)$ observable additional results from the more restricted fitting range $32-42$ GeV are included.

Chapter 12

Conclusion and Outlook

12.1 Conclusion

The DØ group has analyzed 1 fb^{-1} Run II a data, which was collected from 2002 to 2006, to measure to W boson mass. We present a precision measurement of the mass of the W boson.

$$M_W(m_T) = 80.401 \pm 0.023(\text{stat}) \pm 0.037(\text{syst})\ \text{GeV} \tag{12.1}$$

$$M_W(p_T(e)) = 80.400 \pm 0.027(\text{stat}) \pm 0.040(\text{syst})\ \text{GeV} \tag{12.2}$$

$$M_W(\not{E}_T) = 80.402 \pm 0.023(\text{stat}) \pm 0.043(\text{syst})\ \text{GeV} \tag{12.3}$$

The combined result is

$$m_W = 80.401 \pm 0.021\ (\text{stat}) \pm 0.038\ (\text{syst})\ \text{GeV} = 80.401 \pm 0.043\ \text{GeV}.$$

These results are in very good agreement with each other.

In the event generation, a W width of 2099.6 MeV was used. It is different from the value 2093 MeV[64] that has been used for the Tevatron combination. The DØ W mass result is then corrected to[65]

$$m_W = 80.402 \pm 0.043\ \text{GeV}.$$

Figure 12.1 shows the results from experiments carried out by the Tevatron and LEP2. The DØ Run II result agrees well with these experiment and the world average. The DØ measurement is the most precise W boson measurement from one single experiment.

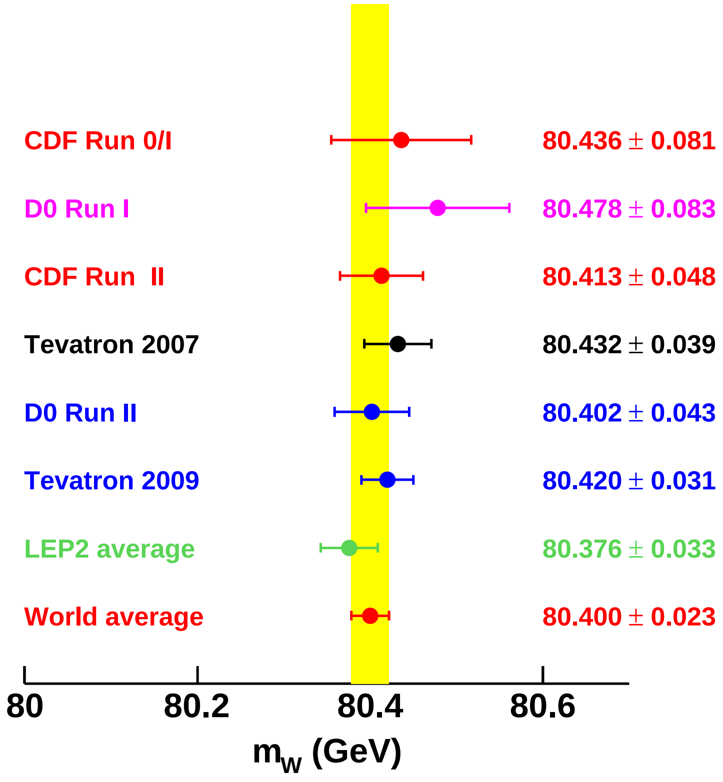

Figure 12.1: W mass measurements at Tevatron and LEP2.

12.2 Outlook

From the W mass uncertainty table in the previous chapter, we already mentioned the dominant experimental systematic is from the electron energy response, which is simply limited by the $Z \to ee$ statistics. Therefore, the easiest way to improve the DØ W mass experimental uncertainty is too increase the size of the data set. Currently the DØ W mass group has already started analyzing the 5 fb^{-1} Run II data. Assuming the same theoretical uncertainty, we will achieve a W mass uncertainty about 25 MeV. On the other hand, the PDF uncertainty is the dominant one in the theoretical part. With more data available, the PDF set can also be constrained more precisely. For example, the W charge asymmetry and jet production measurement will provide a powerful handle on constraining the PDF set.

With the 5 fb^{-1} DØ result and the 2.3 fb^{-1} CDF result, we would expect a W mass uncertainty of about 15 MeV for the Tevatron combination.

Bibliography

[1] S. Glashow, Nucl. Phys. **22**, 579 (1961); S. Weinberg, Phys. Rev. Lett. **19**, 1264 (1967); A. Salam, *Elementary Particle Theory: Relativistic Groups and Analyticity*, Nobel Symposium No. 8, edited by N. Svartholm (Almqvist and Wiksell, Stockholm, 1968), p. 367.

[2] D. Griffiths, Introduction to Elementary Particles, John Wiley & Sons Inc (1987).

[3] F. Halzen and A. Martin, Quarks and Leptons: An Introductory Course in Modern Particle Physics,Wiley, 1st edition (1984).

[4] J. Goldstone et al., Phys. Rev. 127: 965 C 970(1962).

[5] Y. Nambu and G. Jona-Lasinio, Phys. Rev. 122, 345-358 (1961).

[6] Y. Nambu and G. Jona-Lasinio,Phys. Rev.124, 246-254 (1961).

[7] M. Peskin and D. Schroeder, An Introduction to Quantum Field Theory,Westview Press (1995).

[8] L. Ryder, Quantum Field Theory, Cambridge University Press; 2 edition (1996).

[9] A. Sirlin, Phys. Rev. D 22, 971 (1980).

[10] B. Abbott et al. (DØ Collaboration), Phys. Rev. D **58**, 092003 (1998).

[11] A. Kotwal and J. Stark, Measurement of the W Boson Mass at the Tevatron, Annual Review of Nuclear and Particle Science, Nov. 2008.

[12] http://lepewwg.web.cern.ch/LEPEWWG/plots/winter2009/w09_plot_mt.pdf

[13] The LEP Electroweak Working Group:
http://lepewwg.web.cern.ch/LEPEWWG/plots/winter2009/

[14] ALEPH, CDF, DØ DELPHI, L3, OPAL, SLD Collaborations, DØ note 5802(2008).

[15] I. Adam, Measurement of the W Boson Mass with the DØ Detector using the Electron ET Spectrum, PhD Thesis, Columbia University, New York, New York(1997).

[16] T. Andeen, Ph.D. thesis, Northwestern Unversity, Measurement of the W Boson Mass with the DØ Run II Detector Using the Electron P_T Spectrum(2008).

[17] UA1 Collaboration, G. Arnison *et al.*, Phys. Lett. **122B**, 103 (1983);
UA2 Collaboration, M. Banner *et al.*, Phys. Lett. **122B**, 476 (1983);
UA1 Collaboration, G. Arnison *et al.*, Phys. Lett. **126B**, 398 (1983);
UA2 Collaboration, P. Bagnaia *et al.*, Phys. Lett. **129B**, 130 (1983).

[18] M. Syphers, Fermilab Accelerator Division, Accelerator Concepts, Version 3.0 (2002).

[19] Fermilab Accelerator Division Document Databases,
http://beamdocs.fnal.gov/DocDB//Static/Lists//FullList.html

[20] S. Abachi et al. (DØ Collaboration), The DØ Detector, Nucl. Instr. and Methods, A338, 185 (1994)

[21] DØ Upgrade Collaboration, "DØ Silicon Tracker Technical Design Report", http://www-d0.fnal.gov/trigger/stt/smt/smt_tdr.ps.

[22] D. Adams et al. (DØ Collaboration), The D0 Upgrade: Central Fiber Tracker, Technical Design Report, DØ note 4164(1999).

[23] M. Adams et al. (DØ Collaboration), Central Fiber Tracker Technical Design Report, DØ note 3014(1996).

[24] DØ Collaboration, The DØ Upgrade: Forward Preshower, Muon System and Level 2 Trigger, DØ note 2894(1996).

[25] B. Abbott et al. (DØ Collaboration), Measurement of the W boson mass, Phys. Rev. D **58**, 092003(1998).

[26] V. Abazov et. al, The Upgraded DØ Detector, Nucl. Instrum. Methods Phys. Res., A565, 463(2006).

[27] DØ Collaboration, Calorimeter Electronics Upgrade for Run 2, (1998).

[28] J. Zhu, Direct Measurement of the W Boson Decay Width in Proton-Antiproton Collisions at $\sqrt{s} = 1.96$ TeV, PhD Thesis, University of Maryland, College Park, Maryland (2004).

[29] Particle Data Group, Phys. Lett. B, Vol. 667(2008).

[30] F. James, Minuit: A system for Function Minimization and Analysis of Parameters Errors and Correlations, M. Roos Comput. Phys. Commun. 10, 343 (1975).

[31] DØ *W* mass group, Measurement of the *W* boson mass using Run IIa data, DØ note 5868, (2009).

[32] P. Petroff and J. Stark, Proposal to perform a blind measurement of the *W* mass in Run II, DØ note 5388(2007).

[33] T. Golling, Measurement of the $t\bar{t}$ Production Cross-Section at $\sqrt{s} = 1.96$ TeV in the Muon+Jets Final State using a Topological Method, DØ note 4667(2005).

[34] D. Adams, Finding Tracks, DØ note 2958(1996).

[35] H. Greenlee, The DØ Kalman Track Fit, DØ note 4303(2004).

[36] A. Schwartzman and M. Narain, Vertex Fitting by means of the Kalman Filter techinque , DØ note 3907(2001).

[37] G. Steinbruck, Measurement of the Angular Distribution of Electrons from *W* Boson Decay at DØ PhD Thesis, University of Oklahoma (1999).

[38] R. Wigmans, Calorimetry, Oxford University Press (2000).

[39] P. Nadolsky, Theory of W and Z boson production, ANL-HEP-CP-04-138, (2004).

[40] E. Mirkes, J. Ohnemus, W and Z polarization effects in hadronic collisions, Physical Review D, 50, 5692, (1994).

[41] C. Balazs and C.P. Yuan, Soft gluon effects on lepton pairs at hadron colliders, Phys. Rev. D 56, 5558 (1997).

[42] J. Collins, D. Soper and G. Sterman. Nucl. Phys. B250(1985) 199.

[43] F. Landry, R.Brock, P. Nadosky, C.P. Yuan, Fermilab Tevatron run-1 Z boson data and the Collins-Soper-Sterman resummation formalism, Phys. Rev. D **67**, 073016 (2003).

[44] H.L. Lai *et al.*, Phys. Rev. D **55**, 1280 (1997); J. Pumplin *et al.*, JHEP **0310**, 046 (2003).

[45] J. Guo, J. Zhu, J. Hobbs and R. Mccarthy, PDF Uncertainty for W mass Measurement, DØ note 5078(2006).

[46] T. Aaltonen et al. (CDF Collaboration), Phys. Rev. Lett. **99**, 151801 (2007); T. Aaltonen et al. (CDF Collaboration), Phys. Rev. D **77**, 112001 (2008).

[47] J. Osta, Combination of the Run IIa W boson mass measurements, DØ note 5913(2009).

[48] E. Barbiero and Z. Was, Comp. Phys. Commun. **79**, 291 (1994).

[49] J. Guo, J. Zhu, J. Hobbs and R. Mccarthy, Electroweak Uncertainty for the W Mass Measurement, DØ note 5666(2008).

[50] U. Baur, S. Keller and D. Wackeroth, Phys. Rev. D **59** 013002 (1999).

[51] U. Baur, S. Keller and D. Wackeroth, A Monte Carlo program for the calculation of electroweak radiative corrections to Z boson production at hadron colliders, Available at `http://ubhex.physics.buffalo.edu/~baur/zgrad2.tar.gz`

[52] J.Hays, J.Mitrevske,C.Schwanenberger,T.Toole, Single Electron Efficiencies in p17 Data and Monte-Carlo Using p18.05.00 d0correct, DØ note 5105(2006)

[53] Talk given by H. Schellman and D. Chapin, W/Z to electrons weekly meeting, March 23, 2004 (http://www-d0.hef.kun.nl//fullAgenda.php?ida=a0429&fid=61).

[54] Talk given by J. Stark, W mass meeting, May 23, 2007 (http://www-d0.hef.kun.nl//askArchive.php?base=agenda&categ=a07740&id=a07740s1t0/transparencies).

[55] Tim Andeen, Feng Guo, Jun Guo and Junjie Zhu, Effect of Recoil on Electron Identification Efficiency, DØ note 5686(2009).

[56] "Studies of energies below electron window for W mass measurement", F. Guo, J. Hobbs, R. Mccarthy, P. Petroff, M. Rijssenbeek, J. Stark, J.Zhu, DØ Note 5661(2008).

[57] Tim Andeen and Alex Melnitchouk, Measurement of Electron Energy Scale and Offset with $Z \rightarrow ee$ Full Monte Carlo and Data, DØ Note 5662(2009)

[58] C. Fabjan and F. Gianotti, Calorimetry for particla physics, Rev. Mod. Phys., Vol.75 (2003).

[59] A. Melnitchouk, M. Wetstein, Determination of the constant term of the electron resolution, DØ Note 5879(2009).

[60] T. Andeen, M. Cwiok, J. Guo, J. Hobbs, J. Osta, J. Stark, J. Zhu, Modeling the Hadronic Recoil for the W Mass Measurement in Run IIa (Method I), DØ Note 5668 (2008).

[61] Philip R. Bevington Data Reduction and Error Analysis for the Physical Sciences, Mc-Graw Hill Inc.

[62] J. Guo, J. Zhu, J. Hobbs and R. Mccarthy, Background for W Mass Measurement, DØ note 5665(2008).

[63] L. Lyons, D. Gibout, and P. Clifford, Nucl. Instrum. Methods in Phys. Res. A **270**, 110 (1988).

[64] The Tevatron Electroweak Working Group, Combination of CDF and DØ Results on W Boson Mass and Width, FERMILAB-TM-2415 1st August 2008

[65] DØ W mass group, Combination of CDF and DØ Results on the W Boson Mass, DØ note 5938(2009).